A Knudsen Cell for Controlled Deposition of L-Cysteine and L-Methionine on Au(111)

A Thesis Submitted to the
College of Graduate Studies and Research
in Partial Fulfillment of the Requirements
for the degree of Master of Science
in the Department of Physics & Engineering Physics
University of Saskatchewan
Saskatoon

By
Evan Alozie Dubiel

Permission to Use

In presenting this thesis in partial fulfilment of the requirements for a Postgraduate degree from the University of Saskatchewan, I agree that the Libraries of this University may make it freely available for inspection. I further agree that permission for copying of this thesis in any manner, in whole or in part, for scholarly purposes may be granted by the professor or professors who supervised my thesis work or, in their absence, by the Head of the Department or the Dean of the College in which my thesis work was done. It is understood that any copying or publication or use of this thesis or parts thereof for financial gain shall not be allowed without my written permission. It is also understood that due recognition shall be given to me and to the University of Saskatchewan in any scholarly use which may be made of any material in my thesis.

Requests for permission to copy or to make other use of material in this thesis in whole or part should be addressed to:

Head of the Department of Physics & Engineering Physics
Department of Physics & Engineering Physics
116 Science Place
University of Saskatchewan
Saskatoon, Saskatchewan
S7N 5E2
Canada

Abstract

This thesis details the development of expertise and tools required for the study of amino acids deposited on Au(111), with a primary focus on the design and testing of a Knudsen cell for controlled deposition of L-cysteine and L-methionine. An ultra-high vacuum preparation chamber designed by Dr. Katie Mitchell and built by Torrovap Industries Inc. was installed. This chamber is connected to the existing scanning tunneling microscopy chamber via a gate valve, and both chambers can operate independently. Various instruments such as a mass spectrometer, quartz crystal microbalance, ion source, and sample manipulator were installed on the preparation chamber. Scanning tunneling microscopy was performed on both homemade and commercial Au(111) thin films. High resolution images of "herringbone" reconstruction and individual atoms were obtained on the commercial thin films, and optimal tunneling conditions were determined. A Knudsen cell was designed to be mounted on the preparation chamber. The Knudsen cell operates over the temperature range $300 - 400\,\mathrm{K}$, with temperatures reproducible to $\pm 0.5\,\mathrm{K}$, and stable to $\pm 0.1\,\mathrm{K}$ over a five minute period. Reproducible deposition rates of less than $0.2\,\text{Å/s}$ were obtained for both L-cysteine and L-methionine. Electron impact mass spectrometry and heat of sublimation measurements were performed to characterize the effusion of L-cysteine and L-methionine from the Knudsen cell. The mass spectrometry results suggest that L-cysteine was decomposing at $403\,\mathrm{K}$ while L-methionine was stable during effusion. Heats of sublimation of $168.3 \pm 33.2\,\mathrm{kJ/mol}$ and $156.5 \pm 10.1\,\mathrm{kJ/mol}$ were obtained for L-cysteine and L-methionine respectively.

Acknowledgements

I would like to express my thanks and gratitude to all of those who made this work possible. I am grateful to the Nanoscale and Surface Physics Group at the University of Saskatchewan for the opportunity to study and the financial support provided. I would particularly like to thank my supervisor Dr. Katie Mitchell and Dr. Andrew Robinson for their guidance and mentorship. The contributions of colleagues Nathan Olfert, Trevor Coulman, JJ Theron, Mark Wurtz, Dale Heggie, and Mark Rempel warrant acknowledgement. Thanks goes out to Perry Balon, Blair Chomyshen, and Ted Toporowski of the Physics & Engineering Physics Machine Shop and Dave McColl of the Plasma Physics Laboratory for their assistance in the construction of the Knudsen cell and preparation chamber. Technical assistance from J.T. Steenkamp, Yao Yansun, Clay Cederstrand and George Lengel (RHK Technology Inc.) was greatly appreciated. I would also like to thank Dr. Stephen Urquhart, Dr. Matthew Paige, and Edwidge Otero from the Department of Chemistry for their advice and use of labratory equipment. Equal thanks to Dr. Chenzhong Li (Department of Biochemistry) and Jainzhong Fan (Department of Geological Sciences) for use of their laboratories. Last but certainly not least I would like to thank members of my supervisory committee (Dr. Michael Bradley, Dr. Kathryn McWilliams, and Dr. Alexander Moewes) and the entire Department of Physics & Engineering Physics at the University of Saskatchewan for all their wisdom provided over the years.

To my parents, A. Lloyd Dubiel & Audrey Robinson

Contents

List of Tables

List of Figures

List of Abbreviations

AC	Alternating Current
CI	Chemical Ionization
DC	Direct Current
DFT	Density Functional Theory
DNA	Deoxyribonucleic Acid
EI	Electron Impact
FCC	Face-Centered Cubic
HCP	Hexagonal Closed Packed
K-cell	Knudsen Cell
LEED	Low Energy Electron Diffraction
ML	Monolayer
MSIU	Mass Spectrometer Interface Unit
m/z	Mass-to-Charge Ratio
NIST	National Institute of Standards and Technology
OFHC	Oxygen Free High Conductivity Copper
PEP	Department of Physics and Engineering Physics at the University of Saskatchewan
PID	Proportional Integral Derivative
QCM	Quartz Crystal Microbalance
RF	Radio Frequency
SIMS	Secondary Ion Mass Spectrometry
STM	Scanning Tunneling Microscopy
UHV	Ultra-High Vacuum
UHV STM	Ultra-High Vacuum Scanning Tunneling Microscopy

Chapter 1

Introduction

The field of biological surface science is an area of increasing interest [1]. One particular area of interest is the surface immobilization of biomolecules which is important for the development of biosensors [2] [3]. Particularly, targeting biomolecules onto electrodes modified with self-assembled monolayers has received considerable attention for biosensor fabrication [4].

A biosensor is considered to be any sensor that responds selectively and reversibly to the concentration or activity of a chemical species (biomolecule) in a biological environment [5]. Virtually all biological processes involve a type of biological molecule known as a protein [6]. Proteins in living organisms do such things as produce energy, fight disease, propagate nerve impulses, and act as receptors to bind specific foreign material in the body [7]. Proteins are linked to many diseases such as Cystic Fibrosis, Duchenne muscular dystrophy, Huntington's, Parkinson's, and Alzheimer's [8]. It is no wonder that the detection of proteins is a valuable tool in biology and medicine. The detection of a protein or lack there of, inherent in a particular disease can be used as a tool in diagnosis and in monitoring the effectiveness of treatment. Furthermore, a protein sensitive biosensor could be incorporated into an automated drug delivery system, for example to provide controlled release of insulin (a protein produced in the pancreas) in diabetes patients [1] [7].

A diagram of a biosensor is shown in Figure 1.1. The receptive/organic adlayer is usually a receptor protein that senses changes in its environment (i.e. interaction with a biomolecule). The receptor must be selective and interact with the biomolecule of interest and only that biomolecule. Upon interaction, most often a change in shape or charge distribution is induced in the receptor. That change is detected

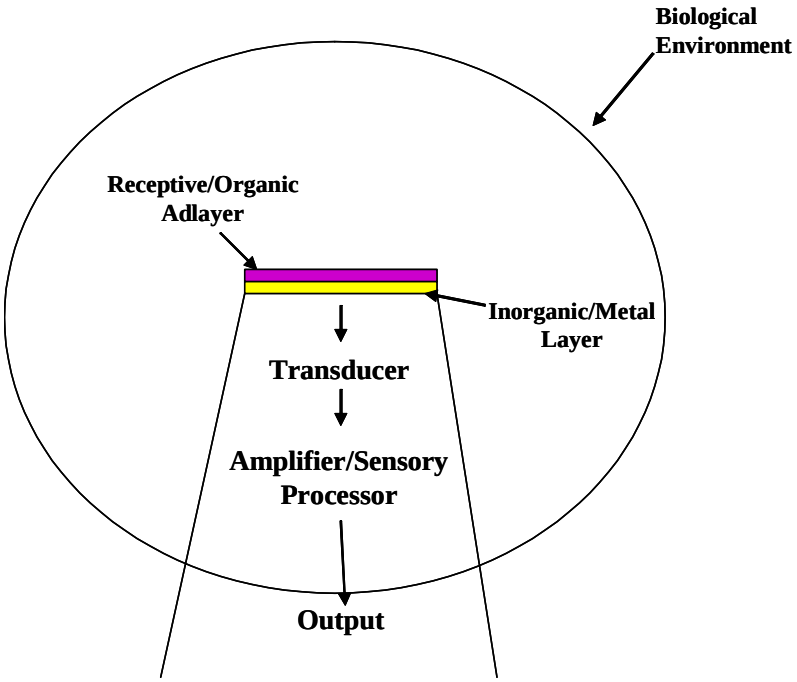

Figure 1.1: Diagram of typical biosensor. Biomolecules come into contact with the organic/metal interface. They are then immobilized and detected. After detection the biomolecules are released back into the environment.

by the transducer and then converted into an electrical signal. The signal is then amplified and processed into a usable output [5] [7] [9] [10].

In order for biosensors to function, the receptor proteins must be anchored to the inorganic/metal layer in such a way that their structure (and thus function) is not affected and, at an appropriate density (not too crowded or too far apart) [3]. Self-assembled monolayers, which are created when molecules assemble themselves into complex and well-defined two dimensional structures through a balance of molecule-molecule and molecule-surface interactions, have received considerable attention as anchor layers for biosensors [11] [12] [13]. Amino acids (the building blocks of proteins) and peptides (chains of amino acids) are interesting candidates for the formation of self-assembled monolayers for biosensors, since they exhibit a range of different intermolecular interactions and also can link readily to proteins [14]. However, before functional overlayers and devices can be developed, the fundamental

interactions of amino acids with an organic/metal surface must be understood.

Biosensors function in an aqueous environment, which will have a significant effect on surface structure and interactions. However, the aqueous environment is quite complex, and many questions concerning the fundamental interaction of amino acids with an inorganic/metal surface can best be addressed in ultra-high vacuum (UHV) studies [15] [16] [17].

While there are many interesting amino acid/surface systems to study, L-cysteine and L-methionine on Au(111) were chosen for this work for several reasons. A Au(111) surface is a good prototype substrate for a biosensor. This is because Au(111) has large (hundreds of nanometers) atomically flat terraces which allow, essentially, "defect free" formation of self-assembled monolayers [18]. Au(111) is also easy to prepare, is relatively inert, and binds molecules terminated with a thiol ($-SH$) group. L-cysteine is particularly interesting to study on Au(111) because it is terminated with a thiol group. It is also of pivotal importance in the structure of large biomolecules such as proteins and enzymes, and can often be found on their boundary [13]. L-methionine is the only other sulfur containing amino acid. It contains an $S-CH_3$ group that is less reactive than the thiol group of L-cysteine [6]. This makes it interesting to study in comparison to L-cysteine.

A wide variety of studies on the L-cysteine/Au(111) interface have been performed in the past, both on solution-deposited and vacuum-deposited samples, using techniques such as scanning tunneling microscopy, density functional theory, and x-ray photoelectron spectroscopy [13] [19] [20] [21] [22] [23] [24] [25]. Together these results indicate that there is likely a complex, coverage-dependent behavior of the electronic and structural properties of the L-cysteine/Au(111) interface that is not yet well understood. To the best of our knowledge, no studies of the L-methionine/Au(111) interface have been reported to date.

The goal of this thesis was to develop the expertise and tools needed to perform scanning tunneling microscopy (STM) experiments on Au(111) and to deposit low coverages of L-cysteine and L-methionine on Au(111). This involved the installation of a UHV preparation chamber, the preparation of Au(111) thin film samples and

their imaging with STM in UHV, and the design, construction and testing of a Knudsen cell (K-cell) for evaporation of L-cysteine and L-methionine.

The main body of the thesis begins in Chapter 2 with a brief review of the background theory related to this project. Chapter 3 describes the experimental setup, including the installation of the preparation chamber. The results of Au(111) thin film preparation and STM imaging are presented in Chapter 4. A description of the K-cell design can be found in Chapter 5. Results relating to the sublimation of L-cysteine and L-methionine from the K-cell are presented in Chapter 6. Chapter 7 presents conclusions and suggestions for future work.

Chapter 2

Theory

This chapter starts with an overview of background theory related to amino acids and proteins, followed by a discussion of metal surfaces, including the reconstruction of Au(111) and the concept of adsorption. Scanning tunneling microscopy (STM) was used to study Au(111), so a brief discussion of the theory is introduced. Also included is a discussion on Knudsen cell (K-cell) effusion. Background theory related to the quartz crystal microbalance (used to measure deposition rates) and to heat of sublimation measurements (performed using the K-cell) close the chapter.

2.1 Biological Molecules

Many biological processes involve proteins [6]. For example, the protein myoglobin transports oxygen in muscle. Proteins are made up of a repertoire of 20 amino acids. The amino acids that constitute the protein and their order determine its structure. Here the general properties of amino acids including structure and chirality are introduced, and specific properties of L-cysteine and L-methionine are included. Bonding of amino acids and the four levels of protein structure are discussed in the end.

2.1.1 Amino Acids

All amino acids are made up of four groups: an amino group (NH_2), a carboxyl group (COOH), a hydrogen atom (H), and a side chain (distinctive R group). The four groups are bonded to a central carbon (C) atom. Cysteine has the side chain CH_2SH [26]. The SH portion of the side chain is called a thiol group. The molecular

arrangement of cysteine is shown in Figure 2.1. Amino acids can exist in a neutral or zwitterionic (polar) state. In the zwitterionic form the amino group has a positive charge (NH_3^+) and the carboxyl group has a negative charge (COO^-) as shown in Figure 2.1. Methionine has a side chain-$(CH_2)_2SCH_3$. The molecular arrangement of methionine is shown in Figure 2.2. Many molecules involved in processes necessary

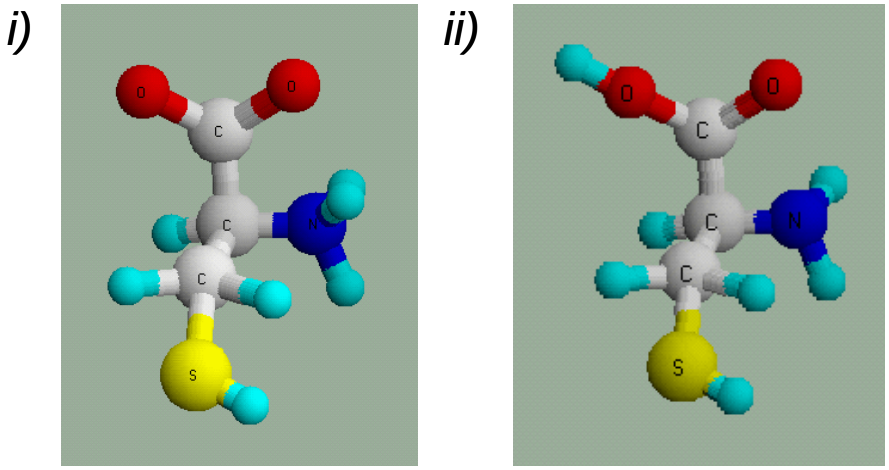

Figure 2.1: Molecular structure of cysteine. i) Molecular arrangement of neutral L-cysteine (note: aqua spheres represent hydrogen atoms). ii) Molecular arrangement of L-cysteine in the zwitterionic form.

for life have a property called chirality (from the Greek word for "hand"). A molecule is chiral if it lacks a plane of symmetry (see Figure 2.3). When the molecule has a plane of symmetry, it is said to be achiral (see Figure 2.3). All chiral molecules exist in two forms. These two forms, conventionally labeled L (levorotatory) - and D (dextrorotatory) - isomers, are non-superimposable mirror images of each other (exactly like our left and right hands) [27]. Examples of the L-isomer and D-isomer forms of an amino acid are shown in Figure 2.4 . Only L-isomers are constituents of proteins [28]. It is thus advantageous to study L-cysteine and L-methionine because they are involved in biological processes.

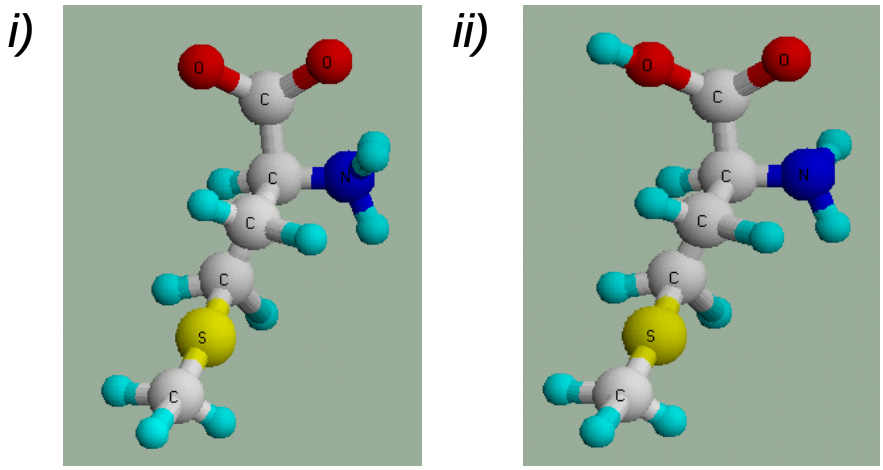

Figure 2.2: Molecular structure of methionine. i) Molecular arrangement of neutral L-methionine (note: aqua spheres represent hydrogen atoms). ii) Molecular arrangement of L-methionine in the zwitterionic form.

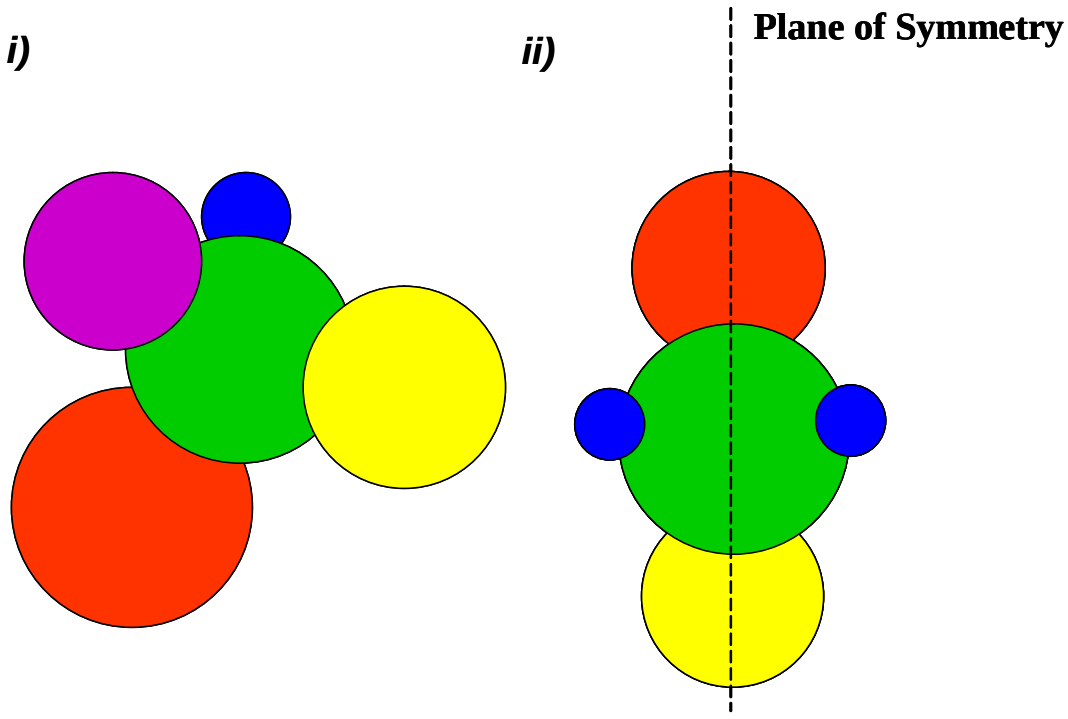

Figure 2.3: Molecular chirality. i) Chiral molecule (no plane of symmetry present). ii) Achiral molecule (plane of symmetry present).

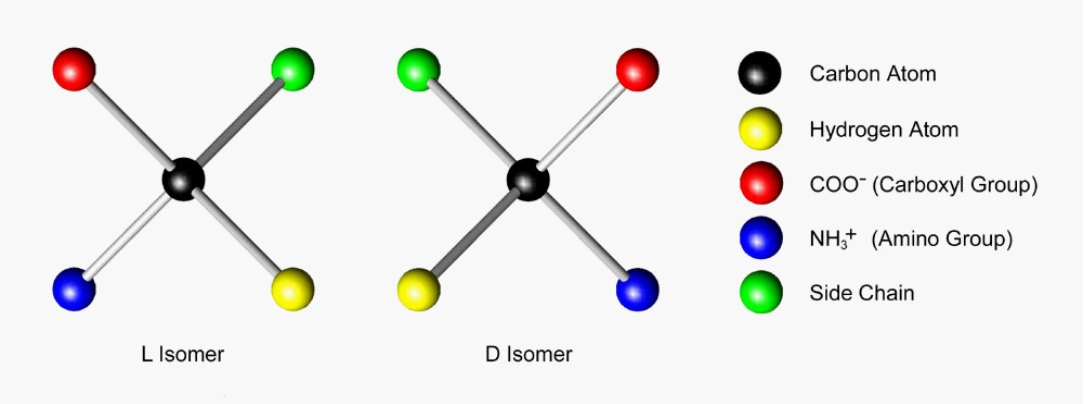

Figure 2.4: The two amino acid molecules are the same except for the fact that their spatial arrangement is different. The two molecules are mirror images of one another. Because there is no way one can rotate one molecule to make it have the same spatial arrangement as the other, the molecules are said to be isomers [6].

2.1.2 Protein Structure

Two amino acids can be bound together with the amino group of one amino acid joined to the carboxyl group of another. This is known as a peptide bond. Many amino acids attached together by peptide bonds are referred to as polypeptide chains. The sulfur (S) atom contained in L-cysteine can result in links between two polypeptide chains or cross-links within a single chain. This is known as disulfide bonding and is shown in Figure 2.5. Amino acids can also be linked via hydrogen bonding. A hydrogen bond consists of two molecules sharing a single hydrogen atom. Hydrogen bonds exist between polar molecules that contain hydrogen, such as water (H_2O). The portions of a polar molecule that have a negative polarity are attracted to the hydrogen (positive polarity) of another molecule [6].

The three-dimensional structure of a protein is dependent on the amino acid sequence. A protein consists of single or multiple polypeptide chains linked together via disulfide bonding, arranged in a three-dimensional structure. A large number of van der Waals interactions (discussed in Section 2.2.3) and hydrogen bonds between various components of the protein help to keep the structure stable [6].

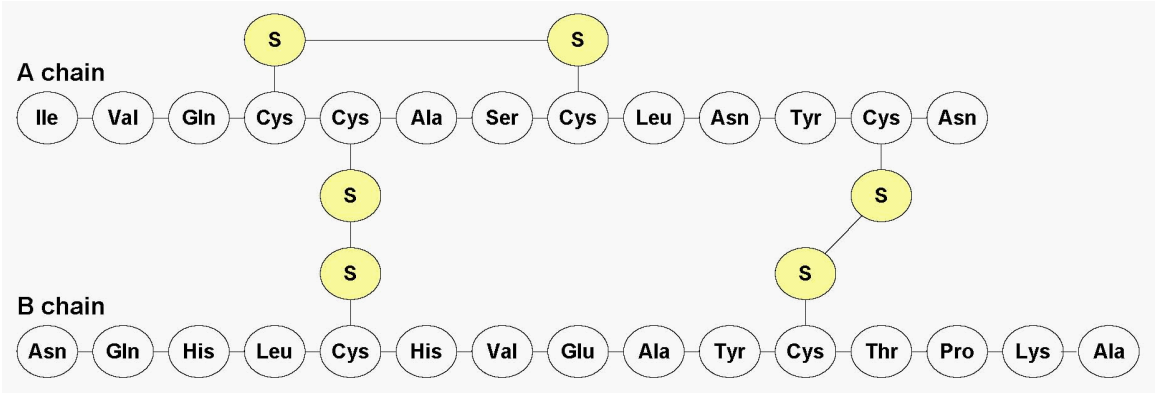

Figure 2.5: Disulfide bonding cross-linking the A chain and linking the A and B chains. S represents the sulfur atom present in cysteine (Cys). The other three-letter abbreviations represent other amino acids constituting the polypeptide chains [6].

Protein structure is divided into four levels. The first level, the primary structure, is the amino acid sequence. Secondary structure refers to the spatial distribution of amino acids near one another in a linear sequence. The tertiary structure is the arrangement of amino acids far apart in the sequence and the pattern of disulfide bonds. Only proteins made up of multiple polypeptide chains have the fourth structural level known as the quaternary structure. The quaternary structure regards the spatial arrangement of the polypeptide chains and the nature of their contacts [6].

Amino acids are interesting for surface adsorption studies both because of their biological relevance and because their ability to form inter-molecular hydrogen bonds may lead to a variety of self-organized two-dimensional structures on surfaces. Studying L-cysteine adsorption on a surface is particularly interesting because it is often found on the boundary of large proteins. Because L-cysteine is often on the boundary of large proteins and there is a strong affinity between S and metal surfaces, L-cysteine can provide a link for suspending a protein on an inorganic surface [29]. L-methionine is interesting to compare to L-cysteine because it also contains S, but in a less reactive side chain [6].

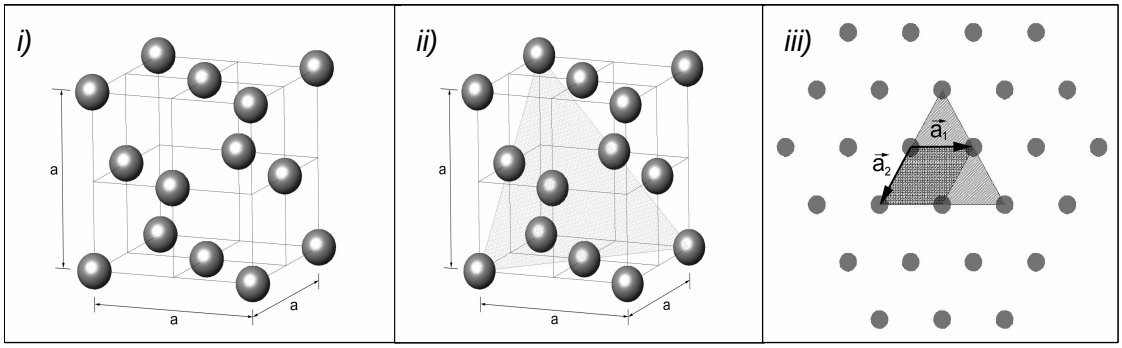

Figure 2.6: FCC structure. i) Face-centered cubic (FCC) conventional unit cell. Note that a = 4.08 Å for Au. ii) FCC conventional unit cell showing the (111) miller index plane. iii) Surface resulting from ideal termination of FCC (111) plane. The unit cell (two-dimensional hexagonal Bravais lattice) of the surface is also shown.

2.2 Metal Surfaces

Surface physics is the study of the first few layers (two or three) of outermost atoms at the termination site of a bulk material (in this case a metal). The surface geometry of a metal substrate is dependent upon the bulk properties of the material. This section introduces the concept of surface reconstruction. Because this project involves a Au(111) surface, Au(111) "herringbone" reconstruction is discussed in detail followed by a brief introduction to adsorption.

2.2.1 Surface Reconstruction

Noble metals Au, Cu, and Ag all have the face-centered cubic (FCC) crystal structure shown in Figure 2.6. The Au(111) surface results from ideal termination of bulk Au along the Miller index (111) plane (see Figure 2.6).

Atoms at the termination site lose some of their nearest neighbours. As a result of the nearest neighbour loss, the surface may undergo physical changes to minimize energy. The process of relaxation occurs when the interatomic spacing of the top

layers changes while maintaining the ideal atomic arrangement of the topmost surface. Surface reconstruction occurs when bonds are formed between atoms on the surface via the unused electrons as a result of the surface creation. Reconstruction is distinguished from relaxation because in reconstruction the atomic arrangement changes as a result of the surface's energy minimization [30].

A common notation used to label a surface reconstruction is known as Wood's notation. For this project Wood's notation can be summarized as follows:

$$\left(\frac{|\overrightarrow{a_0}|}{|\overrightarrow{a_s}|} \times \frac{\left|\overrightarrow{b_0}\right|}{\left|\overrightarrow{b_s}\right|} \right) \tag{2.1}$$

where $|\overrightarrow{a_0}|$ and $\left|\overrightarrow{b_0}\right|$ are magnitudes of the vectors describing the unit cell of the reconstructed surface and $|\overrightarrow{a_s}|$ and $\left|\overrightarrow{b_s}\right|$ are the magnitudes of the unit cell vectors of the ideal surface. Using this notation, a surface which is not reconstructed would be labeled (1 x 1), a surface with a reconstruction leading to surface unit cell vectors twice as long as those in the ideal surface would be labeled (2 x 2), and so on. A more general discussion of Wood's notation can be found in Attard *et. al.* [31].

2.2.2 Reconstruction of Au(111)

When a bulk Au crystal is cut along the (111) plane, a (22 x $\sqrt{3}$) "herringbone" reconstruction occurs. A feature of Au(111) reconstruction is the tendency of the top atoms to contract into a higher area density than that of the ideal surface [32]. The observation of 23 Au atoms on 22 bulk lattice sites gives an average contraction of 4.55% [33]. The ideal and reconstructed surfaces are shown in Figure 2.7. The atomic spacing on an ideally terminated Au(111) surface is 2.88 Å [34]. The (22 x $\sqrt{3}$) ideally terminated unit cell (dotted red line in Figure 2.7(i)) has a length of 63.4 Å in the $\left[1\bar{1}0\right]$ direction (22 spaces times 2.88 Å per space). The ideal termination surface also has the atoms arranged in a hexagonal pattern (represented by the purple dotted line). The reconstructed surface consists of regions with FCC and hexagonal close packed (HCP) stacking along with gradual transition regions

(Figure 2.7(ii)). For an atom in the top layer, theoretical studies indicate the FCC site as being the most energetically favourable, followed by the HCP, bridge, and top site respectively. The location and relative energy of each site is shown in Figure 2.8. This energetic ordering of the sites results in contraction along the $[1\bar{1}0]$ direction as being the most favourable. Contraction does not occur along the $[11\bar{2}]$ direction because that would force the atoms to occupy the top sites that have a very high energy [32]. The HCP regions are slightly smaller in size in comparison to that of the FCC because of HCP having a slightly higher energy [33]. A consequence of the contraction is a non-homogeneous surface [35]. Interatomic spacing varies in the $[1\bar{1}0]$ direction [33]. The transition regions tend to have a smaller nearest neighbour distance (2.68 Å) while that in the FCC region is typically larger (2.86 Å) [35]. This indicates that as a result of the reconstruction, the average interatomic spacing is smaller than that of an ideally terminated bulk Au crystal.

Although Au(111) is a complex surface, it is relatively easy to prepare and is chemically inert. Au(111) also binds thiol terminated molecules. Because of that, Au(111) has been used extensively as a substrate for creating prototype biosensors and other devices, and is thus an important surface to study [21].

2.2.3 Adsorption

Adsorption is defined as the process by which atoms and molecules interact with and become attached to a substrate. There are two types of adsorption: chemisorption and physisorption. Chemisorption is direct bonding characterized by an exchange of electrons between the adsorbate and substrate. The typical bonding strength of chemisorption is on the order of 1eV/atom. Physisorption is an indirect form of adsorption in which interactions between the adsorbate and substrate are weak and long range [31]. Unlike chemisorption, physisorption involves no exchange of charge between the surface atoms and the adatom [36]. The induced dipole moments in the surface and adsorbate atoms cause an attractive interaction known as the van der Waals force [30]. Bonding strength in physisorption is typically 0.01eV.

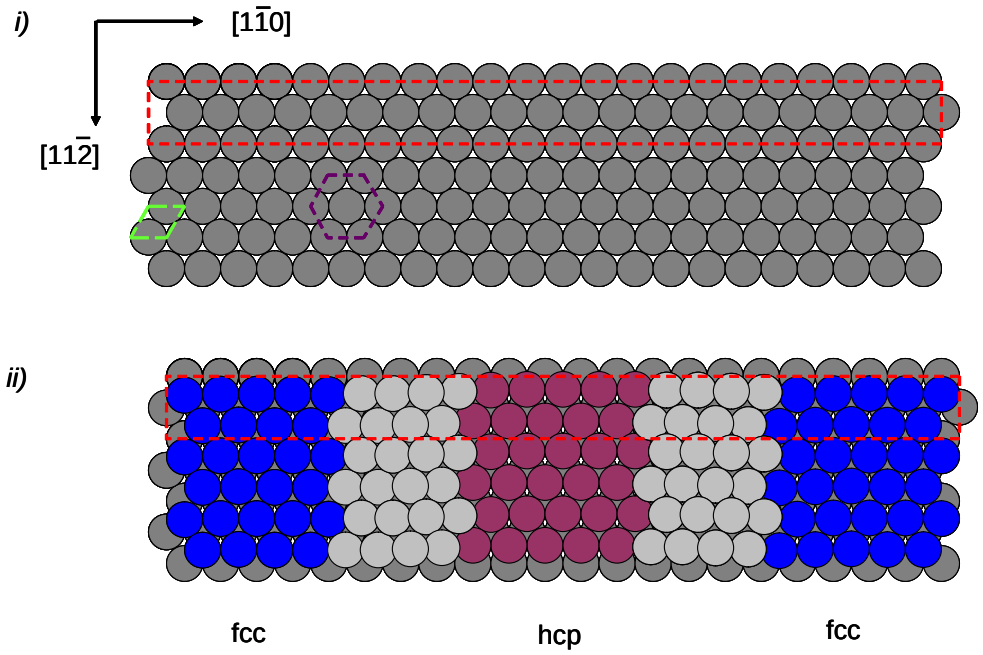

Figure 2.7: Au(111) reconstruction. i) Ideal termination of Au(111). The dotted red lines represent the superimposed unit cell of the (22 x $\sqrt{3}$) reconstructed surface. The dotted green lines represent the superimposed unit cell of the (1 x 1) reconstructed surface. ii) Au(111) reconstructed surface. The unit cell now contains 23 Au atoms in the $[1\bar{1}0]$ direction (see Figure 2.8). Note that the "lighter" atoms (transition region) are higher, so the surface is "rumpled". This figure was provided by Dr. Katie Mitchell.

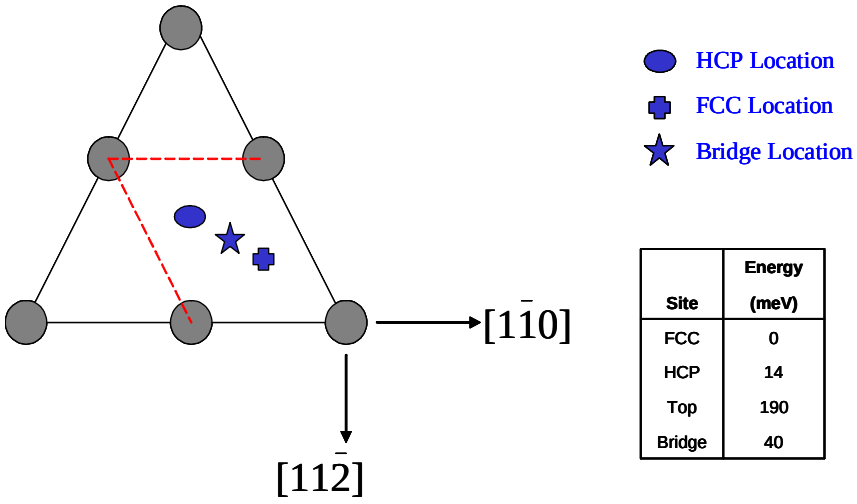

Site	Energy (meV)
FCC	0
HCP	14
Top	190
Bridge	40

Figure 2.8: Site locations and lattice directions for Au(111) ideal termination. Center of lattice point (grey circle) is defined as the top site. The table shows the relative energy of an atom located at each site [32].

For a small flux of incoming molecules from a thermal evaporation source, we will initially have a surface with isolated adsorbed molecules. As more molecules are adsorbed on a surface, the optimal adsorption site may change as molecule-molecule interactions become important in addition to molecule-substrate interactions [13] [24]. The balance of molecule-molecule and molecule substrate interactions may lead to a 2-D self-assembled structure. Note that the bonding sites and 2-D structure of an adsorbed layer do not necessarily reflect the equilibrium structure, but can be strongly influenced by factors such as substrate temperature during deposition, deposition rate, annealing, presence of defects, and so on. [11].

2.3 Scanning Tunneling Microscopy

Since its invention in 1981 by G. Binnig and H. Rohrer, the scanning tunneling microscope (STM) has been a powerful tool in the structural determination of surfaces and interfaces at the nanometer and sub-nanometer scale. The STM allows direct real-space determination of surface structure [37].

The STM operates based on the theory of quantum mechanical tunneling. This section will outline an elementary (time-independent) quantum mechanical tunneling model followed by a more sophisticated (time-dependent) model, and a brief discussion of lateral resolution. A quick description of the physical operation and basic feedback mechanism used in STM is presented in the end.

2.3.1 A One-Dimensional Time Independent Model of Scanning Tunneling Microscopy

In STM, electrons quantum mechanically tunnel through a vacuum gap from a sharp metal tip to a sample or vice versa. The tunneling direction is dependent on the polarity of the bias voltage between tip and sample. Consider the one-dimensional tunneling barrier in Figure 2.9 . The wavefunction in the classically forbidden region is given by

$$\Psi \propto e^{-\kappa z} \tag{2.2}$$

where κ is the decay constant and is given by the following expression

$$\kappa = \frac{\sqrt{2m(U-E)}}{\hbar} \tag{2.3}$$

where m is the electron mass, E is the energy of the electron, U is the potential barrier height, and $\hbar$ is the reduced Planck's constant. The term $U - E$ can be approximated by averaging the work functions (ϕ_μ and ϕ_ν) of the tip and sample [34]. Thus

$$U - E = \frac{\phi_\mu + \phi_\nu}{2} = \phi \tag{2.4}$$

The tunneling current (i.e. tunneling probability), I is given by

$$I \propto e^{-2\kappa z} \tag{2.5}$$

where

$$\kappa = \frac{\sqrt{2m\phi}}{\hbar} \tag{2.6}$$

Assume we scan the Au(111) surface with a tungsten tip. The work functions for Au and tungsten are 5.4 eV and 4.8 eV respectively [38]. Using the values for the

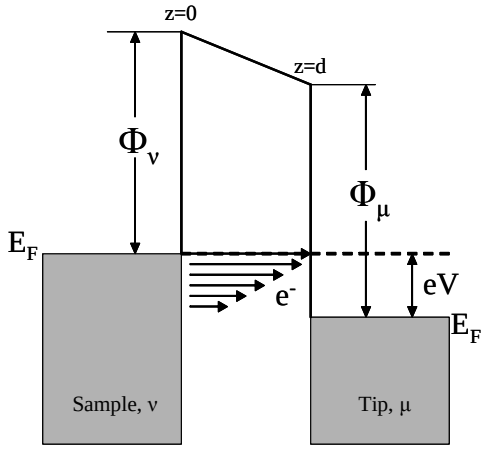

Figure 2.9: Potential barrier between sample and tip. Note that in this figure the bias voltage has a polarity that will allow electrons of sufficient energy to tunnel from the sample to the tip. Φ_υ and Φ_μ are the work functions of the sample and tip respectively, e is the elementary charge of an electron, V is the bias voltage, z is the tip position, and E_F is the Fermi level. It should be noted that most of the tunneling electrons e^- come from near the Fermi level, since this has the highest density of states.

work functions and applying the numerical values $\hbar = 6.582$ x 10^{-16} eV. s and $m = 0.511 \frac{\text{MeV}}{c^2}$ to equation 2.6, the resulting decay constant is

$$\kappa = 1.16\,\text{Å}^{-1} \tag{2.7}$$

The tunneling current has an extremely sensitive dependence on tip-sample distance z. For example, with the result of equation 2.7 applied to equation 2.5, a change of tip-sample distance as small as 1 Å changes the tunneling current by an order of magnitude. A change in tip-sample distance on the order of an atomic step (2-5 Å) can change the tunneling current I by as much as three orders of magnitude [39].

The one-dimensional model outlined above quantitatively highlights the sensitivity of tunneling current I to tip-sample distance z. This is one reason for the remarkable capabilities of STM such as atomic resolution [40]. However, in reality STM is three-dimensional. Thus to truly model STM we must extend our studies to three dimensions and consider time-dependence.

2.3.2 A Three-Dimensional Time Dependent Model of Scanning Tunneling Microscopy

A better explanation of the phenomena inherent in STM requires us to consider time dependence, as well as the geometric properties of the tip and sample. Because the bias voltage V is quite small (tens of mV to a few V), time-dependent perturbation theory can be used to study STM, and this theory was first performed by John Bardeen [41].

From time-dependent perturbation theory, one can determine the probability ω of an electron tunneling between a given tip and sample state using Fermi's Golden Rule [42] [43]:

$$\omega = \frac{2\pi}{\hbar} |M_{\mu\nu}|^2 \, \delta(E_\nu - E_\mu) \tag{2.8}$$

where $M_{\mu\nu}$ is the tunneling matrix, E_ν is the energy of the electron in the sample, and E_μ is the energy of the electron in the tip. The tunneling matrix $M_{\mu\nu}$ is determined from the overlap of wave functions of the tip and the sample at a separation distance z [41]. Bardeen showed the tunneling matrix $M_{\mu\nu}$ to be

$$M_{\mu\nu} = -\frac{\hbar^2}{2m} \int \partial \overrightarrow{S} . \left(\psi_\mu^* \nabla \psi_\nu - \psi_\nu \nabla \psi_\mu^* \right) \tag{2.9}$$

where the integral is evaluated over any surface lying entirely within the barrier region between the tip and sample [44]. Summing over all relevant states yields a tunneling current

$$I = \frac{4\pi e}{\hbar} \int f(E_F - eV + \varepsilon) f(E_F + \varepsilon) \rho_\mu (E_F - eV + \varepsilon) \rho_\nu (E_F + \varepsilon) \, |M_{\mu\nu}|^2 \, \partial\varepsilon \tag{2.10}$$

where V is the applied bias voltage, $f(E)$ is the Fermi distribution function, ρ_μ is the density of states of the tip, ρ_ν is the density of states of the sample, E_F is the Fermi energy, and ε is an incremental energy. The Fermi distribution function is defined as

$$f(E) = \frac{1}{1 + e^{\left(\frac{E - E_F}{k_B T}\right)}}. \tag{2.11}$$

Because we operate at room temperature, $k_B T = 0.026\,\text{eV}$, and the Fermi distribution function can be approximated as a step function. In this case the tunneling

current becomes

$$I \propto \int \rho_\nu(E_F - eV + \varepsilon)\rho_\mu(E_F + \varepsilon)\partial\varepsilon \tag{2.12}$$

which shows the tunneling current as being a convolution of the tip and sample density of states [45].

2.3.3 Lateral Resolution

The lateral resolution of STM is complex and depends on factors that may change during the course of an experiment, such as tip shape and electronic structure. It is difficult to define a general STM resolution function, however several models have been developed to describe STM resolution under different conditions.

J. Tersoff and D.R Hamann used Bardeen's formalism, also taking into account the geometric properties of the tip [46]. Using the assumption that only spherical-wave tip states contribute to tunneling [47], they were able to show that for a metal surface with a fundamental periodicity a the corrugation amplitude Δz can be estimated to be

$$\Delta z \approx \frac{2}{\kappa} \exp\left[-2\left(\sqrt{\kappa^2 + \frac{\pi^2}{a^2}} - \kappa\right) z\right] \tag{2.13}$$

where κ is the decay constant, a is the periodicity of the surface, and z is the distance from the surface to the center of curvature of the tip. If the corrugation amplitude Δz is larger than the z-resolution of the STM (0.05 Å for our STM), then the lateral structure can be resolved by the STM. For large superstructure surfaces such as (22 x $\sqrt{3}$) Au(111), Tersoff & Hamann's theory provides reasonable explanation of STM observations. However, it fails to explain atomic resolution obtained in such experiments [45].

A. Baratoff proposed that atomic resolution is likely due to a single highly localized state protruding from the apex of the tip [48]. Such a state was confirmed experimentally to exist in tungsten [49] [50]. First principle calculations showed that for tungsten clusters there exists a dz-like state, which predominantly contributes to the tunneling current and may lead to atomic resolution images [51].

2.3.4 Scanning Tunneling Microscope Feedback Mechanism

The physical operation of an STM is relatively simple. A metal tip is brought very close (a few Å) to the surface of interest. The tip is then scanned across the surface with a small bias voltage applied between the tip and the surface. The tip-surface height is adjusted to maintain a constant tunneling current, using a feedback mechanism. The trace of the tip generally results in a representation of the surface topography that is a map of constant surface charge contours [45] [52].

Control of the distance between the tip and sample is achieved through the tunneling current. The STM mode used in this project is the constant current mode. An elementary feedback loop for constant current mode is shown in Figure 2.10. A set point current acts as a reference. The tunneling current is measured and compared to the set point current. Based on the difference between the set point and tunneling current, the tip position z is adjusted to minimize the difference between the two currents. The tip is moved across an area of the sample. The gap between the tip and surface adjusted to keep the tunneling current constant is recorded over the scanned area [53]. At large features (vertical height $\geq$ nm), this creates a topographical image of the surface convoluted with the tip shape.

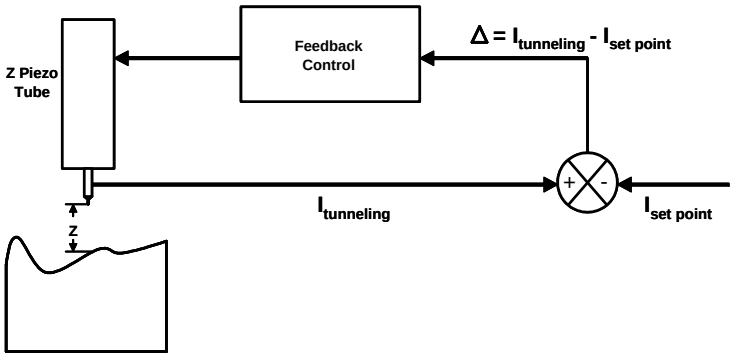

Figure 2.10: Feedback circuit for constant current mode. The feedback control box adjusts the voltage to the z piezo tube to minimize Δ.

2.4 Knudsen Cells and Quartz Crystal Microbalances

In this project a Knudsen cell (K-cell) was designed with the aim of performing controlled deposition of L-cysteine and L-methionine on Au(111). A quartz crystal microbalance (QCM) was used to calibrate the deposition rate of these amino acids. The K-cell and the QCM were also used to measure the heat of sublimation of L-cysteine and L-methionine. Here the theory behind these two devices is presented, followed by the background theory for the heat of sublimation experiment.

2.4.1 Physical Vapour Deposition from a Knudsen Cell

A K-cell consists of a nearly confined gas in a volume, created by loading the cell with a small amount of material and then heating so that the material sublimes. The volume has a small hole from which a fraction of the molecules escape (see Figure 2.11).

A K-cell operates based on the theory of molecular effusion (demonstrated by Knudsen in 1909)[54]. Effusion is the process by which molecules making up a gas escape from confinement through a small hole. An example of this is when an inflated balloon shrinks after a period of time. The shrinkage is a result of the gas molecules escaping through the porous material balloons are made of. Effusion can be described quantitatively with the use of the Kinetic Theory of Gases [55]. Kinetic theory describes gases as consisting of a collection of molecules moving in random directions. The speed of each particle is not necessarily the same, but is assumed to follow the Maxwell distribution

$$P(v) = 4\pi \left(\frac{M}{2RT}\right)^{\frac{3}{2}} v^2 e^{-\frac{Mv^2}{2RT}} \tag{2.14}$$

where v is the molecular speed, M is the molar mass of the gas, R is the gas constant,

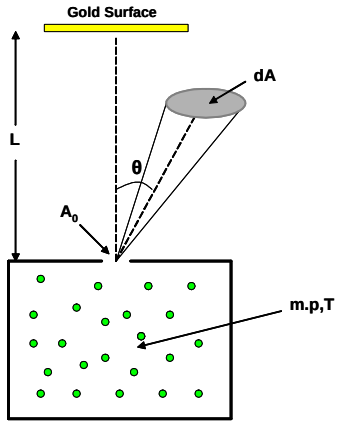

Figure 2.11: A fraction of gas molecules (L-cysteine or L-methionine) escape through the small opening and many that escape are adsorbed onto the Au(111) substrate. Here L is the distance from the effusion source to the substrate, A_0 is the area of the escape hole, m is the mass of a single gas molecule, p is the pressure of the gas, T is the temperature of the gas and, ϑ is the exit angle.

T is the temperature of the gas, and $P(v)$ is the probability of a molecule having speed v [56].

To quantitatively describe effusion, consider a box of volume V with a hole of area A_0 (see Figure 2.12). The volume fraction of molecules that can exit through an area ∂A_0 during a time ∂t at an exit angle θ is

$$\frac{v\partial t\partial A_0 \cos\theta}{V} \tag{2.15}$$

where v is the speed of the molecule and θ is the angle shown in Figure 2.12. Not every molecule in the volume $v\partial t\partial A_0 \cos\theta$ can escape due to the fact that the direction in which the molecules travel may not coincide with the area of the escape hole. Only the fraction of molecules $\frac{\partial\omega}{4\pi}$ in the solid angle $\partial\omega$ can escape.

Therefore, the number of molecules that can escape through an area ∂A_0 in a time ∂t into a solid angle $\partial\omega$ about an exit angle θ is

$$\partial^4 N_e = N\frac{v\partial t\partial A_0 \cos\theta}{V}\frac{\partial\omega}{4\pi}P(v)\partial v \tag{2.16}$$

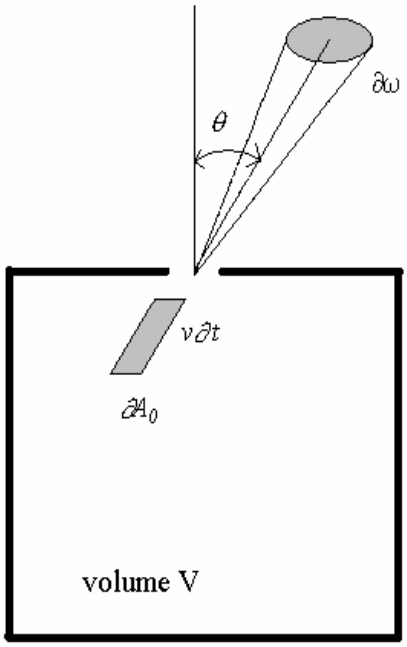

Figure 2.12: Geometry of Knudsen cell. Molecules are confined to a volume V and can effuse through an opening of total area A_0.

where N is the total number of molecules. Integrating over all speeds yields

$$-\infty \int^{\infty} vP(v)\partial v = \left(\frac{8k_BT}{\pi m}\right)^{\frac{1}{2}} \tag{2.17}$$

where $k_B = R/N_A$ and we make use of $M = mN_A$. Note that $N_A = 6.02\text{x}10^{23}$ (Avogadro's Number), $k_B = 1.38\text{x}10^{-23}\,\text{J/K}$ (Boltzmann's constant), and m is the mass of a single molecule. Equation 2.16 now has the form

$$\partial^3 N_e = \frac{N}{V}\left(\frac{8k_BT}{\pi m}\right)^{\frac{1}{2}} \cos\theta \frac{\partial\omega}{4\pi}\partial t \partial A_0. \tag{2.18}$$

Using the Ideal Gas Law,

$$pV = Nk_BT \tag{2.19}$$

where p is the pressure. Equation 2.18 can be rewritten as

$$\partial^3 N_e = p\,(2mk_BT)^{-\frac{1}{2}} \cos\theta \frac{\partial\omega}{\pi}\partial t \partial A_0 \tag{2.20}$$

$$\frac{\partial^3 N_e}{\partial A_0 \partial t \partial\omega} = (2\pi mk_BT)^{-\frac{1}{2}}\, p\frac{\cos\theta}{\pi} \tag{2.21}$$

which is defined as the number of molecules per unit area of the hole per unit time per unit solid angle. The portion

$$Z_w = \frac{p}{(2\pi m k_B T)^{\frac{1}{2}}} \tag{2.22}$$

is the number of collisions per unit time per unit area [57]. Integrating over the area of the escape hole A_0 results in

$$\frac{\partial^2 N_e}{\partial t \partial \omega} = Z_w A_0 \frac{\cos\theta}{\pi}. \tag{2.23}$$

The flux at an escape angle θ is given by

$$\frac{\partial^2 N_e}{\partial t \partial A} = \frac{\partial^2 N_e}{\partial t \partial \omega}.\frac{\partial \omega}{\partial A}. \tag{2.24}$$

Because

$$\frac{\partial \omega}{\partial A} = \frac{4\pi}{4\pi L^2} \tag{2.25}$$

where L is the distance from the effusion source to the substrate, the flux is finally written as

$$\frac{\partial^2 N_e}{\partial t \partial A} = \frac{Z_w A_0}{\pi L^2} \cos\theta \tag{2.26}$$

The flux, $\frac{\partial^2 N_e}{\partial t \partial A}$ of molecules from the small hole follows a distribution known as the Knudsen Cosine Law [58] [59] [60]. As the angle θ becomes larger, the "escape window" becomes effectively smaller; thus the flux decreases.

2.4.2 The Quartz Crystal Microbalance

In order to calibrate the deposition rates of L-cysteine and L-methionine on Au(111), a device capable of measuring very small changes in mass is required. For this task, a quartz crystal microbalance (QCM) was used. Gűnther Sauerbrey was the first to study the QCM quantitatively [61]. In a QCM, a quartz crystal vibrates at its resonant frequency. The resonant frequency of a body is dependent on its mass. Thus a small change in mass of the quartz crystal will cause a measurable shift in resonant frequency [62].

As shown in Figure 2.13, a quartz crystal plate oscillating in resonance in the thickness-shear mode must satisfy

$$t_q = \frac{\lambda_q}{2} \tag{2.27}$$

where t_q is the thickness of the quartz plate and λ_q is the wavelength of the elastic thickness shear mode wave. Multiplying both sides of equation 2.27 by the resonant frequency f_q and using the fact that

$$v_q = f_q \lambda_q \tag{2.28}$$

where v_q is the velocity of the elastic wave, yields

$$f_q = \frac{v_q}{2t_q} \tag{2.29}$$

Suppose that there is an infinitesimal change in thickness ∂t_f due to the addition of a thin film. The shift in resonant frequency ∂f_q is

$$\frac{\partial f_q}{f_q} = -\frac{\partial t_f}{t_q} \tag{2.30}$$

Here the "-" sign indicates a decrease in resonant frequency. For our application, it is more convenient to write equation 2.30 in mass per unit area (areal density) form rather than thickness form, thus

$$\frac{\partial f_q}{f_q} = -\frac{\partial m_f}{m_q} \tag{2.31}$$

where ∂m_f is the additional areal mass due to the film and m_q is the mass of the quartz plate. If one assumes that the mass of the thin film is arbitrarily small, then equation 2.31 can be written as

$$\frac{(f_c - f_q)}{f_q} = -\frac{m_f}{m_q} \tag{2.32}$$

where f_c is the resonant frequency of the quartz crystal with the deposited film. Using the fact that

$$m_q = t_q \rho_q \tag{2.33}$$

where ρ_q is the density of quartz, along with substitution of equation 2.33 into equation 2.32 results in

$$m_f = -m_q \frac{(f_c - f_q)}{f_q} \tag{2.34}$$

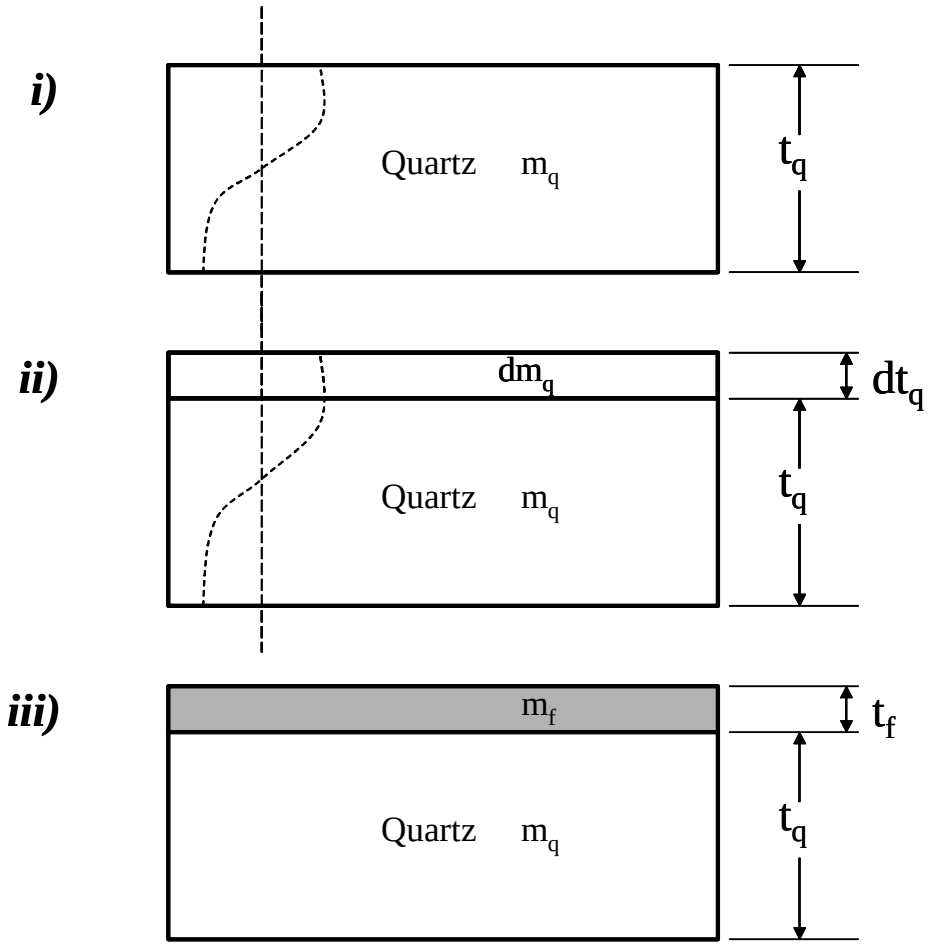

Figure 2.13: Oscillating quartz crystal plate. i) In resonance, the wavelength λ_q is one half the thickness t_q of the quartz plate. ii) A change in the quartz plate thickness of dt_q results in an increase in wavelength. iii) In this model the mass m_f of the deposited film is treated as the equivalent amount of quartz mass [63].

$$m_f = -t_q \rho_q \frac{(f_c - f_q)}{f_q} \tag{2.35}$$

$$m_f = -\frac{v_q}{2f_q} \rho_q \frac{(f_c - f_q)}{f_q} \tag{2.36}$$

If one uses the fact that the propagation velocity of a mechanical wave in the quartz is [64]

$$v_q = \sqrt{\frac{\sigma_q}{\rho_q}} \tag{2.37}$$

where σ_q is the Young's modulus of quartz, the shift in resonant frequency is

$$(f_c - f_q) = -\frac{2f_q^2}{\sqrt{\rho_q \sigma_q}} m_f \tag{2.38}$$

Finally using the definition of "areal density"

$$m_f = \frac{m}{A_{\text{exp}}} \tag{2.39}$$

where m is the total addition of mass and A_{exp} is the area of exposure, the shift in resonant frequency due to the addition of a small mass becomes

$$\Delta f = -\frac{2f_q^2}{A_{\text{exp}} \sqrt{\rho_q \sigma_q}} m \tag{2.40}$$

where $\Delta f = f_c - f_q$ is the shift in resonant frequency. This is the Sauerbrey equation. Another common form of the Sauerbrey equation is

$$\Delta f = -C_f m \tag{2.41}$$

where

$$C_f = \frac{2f_q^2}{A_{\text{exp}} \sqrt{\rho_q \sigma_q}} \tag{2.42}$$

is defined as the "mass sensitivity" [63] [65].

Since we know C_f for a given QCM, a measurement of Δf per unit time gives us added mass per unit time. To obtain the deposition rate (thickness per unit time), we divide by the volume density of the material being deposited.

2.4.3 Determination of Heat of Sublimation using a Knudsen Cell

Effusion from a K-cell can be used to determine the latent heat of sublimation of the material undergoing effusion [66]. This can be done by measuring deposition rate at various temperatures with a quartz crystal microbalance (QCM) [67].

Inside the K-cell, a solid is being converted into a gas. If the material is in thermal equilibrium, then it obeys the Clausius-Clapeyron equation

$$p = C_2 \exp\left(-\frac{H_\nu}{RT}\right) \tag{2.43}$$

where p is the pressure inside the K-cell, T is the temperature, R is the gas constant, H_ν is the heat of sublimation of the material under study, and C_2 is a proportionality constant [56].

The pressure p can be determined experimentally using the quartz crystal microbalance. The number of molecules deposited onto the surface is

$$N_e = \frac{\rho A \tau}{m} \tag{2.44}$$

where ρ is the density of the overlayer, τ is the overlayer thickness, A is the area of the substrate, and m is the mass of a single molecule composing the overlayer . An infinitesimal change in the number of molecules deposited is

$$\partial N_e = \frac{\rho A \partial \tau}{m} \tag{2.45}$$

Starting with the Knudsen Cosine Law

$$\frac{\partial^2 N_e}{\partial t \partial A} = \frac{Z_w A_0}{\pi L^2} \cos\theta \tag{2.46}$$

where

$$Z_w = \frac{p}{\sqrt{2\pi m k_B T}} \tag{2.47}$$

is the number of collisions per unit area per unit time (p is the pressure inside the K-cell and k_B is Boltzmann's constant), A_0 is the area of the escape hole, L is the

distance from the effusion source to the substrate, and θ is the escape angle, we solve for ∂N_e:

$$\int \partial^2 N_e = \frac{Z_w A_0}{\pi L^2} \cos\theta dt \int dA \tag{2.48}$$

$$\partial N_e = \frac{Z_w A_0}{\pi L^2} \cos\theta A \partial t. \tag{2.49}$$

The $\cos\theta$ term is set to one, assuming uniform growth across the QCM sensor, consistent with the Sauerbrey equation (see equation 2.40) [63]. We then substitute ∂N_e from equation 2.45 and solve for p:

$$\frac{\rho A \partial \tau}{m} = \frac{p}{\sqrt{2\pi m k_B T}} \frac{A_0}{\pi L^2} A \partial t \tag{2.50}$$

$$p = \frac{\pi L^2 \rho}{A_0} \left(\frac{2\pi k_B T}{m}\right)^{\frac{1}{2}} \frac{\partial \tau}{\partial t} \tag{2.51}$$

$$\delta p = \left(\sqrt{\left(\frac{1}{2}\frac{\delta T}{T}\right)^2 + \left(\frac{\delta\left(\frac{\partial \tau}{\partial t}\right)}{\frac{\partial \tau}{\partial t}}\right)^2} \right) p \tag{2.52}$$

This analysis follows the method of Hutchings *et. al.* [65]. Equation 2.52 is the uncertainty as a result of error propagation using partial derivatives added in quadrature [68]. Only uncertainties in T and $\frac{\partial \tau}{\partial t}$ are included since these are the only quantities that change during an experiment. The QCM will give a value of the rate of change of thickness $\frac{\partial \tau}{\partial t}$. We can thus calculate the partial pressure of the material inside the Knudsen oven using equation 2.51. Equation 2.43 can be rewritten in the form

$$\ln p = -\frac{H_\nu}{R}\left(\frac{1}{T}\right) + \ln C_2 \tag{2.53}$$

with

$$\delta(\ln p) = \frac{\delta p}{p} \tag{2.54}$$

$$\delta(\ln p) = \left(\sqrt{\left(\frac{1}{2}\frac{\delta T}{T}\right)^2 + \left(\frac{\delta\left(\frac{\partial \tau}{\partial t}\right)}{\frac{\partial \tau}{\partial t}}\right)^2} \right) \tag{2.55}$$

A plot of $\ln p \; vs. \frac{1}{T}$ should yield a straight line with a slope

$$slope = -\frac{H_\nu}{R} \tag{2.56}$$

Thus the heat of sublimation can readily be acquired using

$$H_\upsilon = -(slope)R \tag{2.57}$$

$$\delta(H_\nu) = \delta(slope)R. \tag{2.58}$$

Chapter 3

Experimental Setup

The experiments were performed in an ultra-high vacuum (UHV) system consisting of an RHK UHV 300 scanning tunneling microscope (STM) and a custom designed sample preparation/analysis chamber. The Au(111) experiments were performed in the STM chamber. The preparation/analysis chamber was then installed, and then used for all of the Knudsen cell experiments. The layout of the system is shown in Figure 3.1. The entire system is mounted on a steel frame supported by three air legs. The air legs isolate the system from external vibrations. In this chapter, the RHK UHV system and fast entry load-lock will be discussed first, followed by a description of the STM itself. Next, the preparation/analysis chamber and its installation will be described. A description of the mass spectrometer and quartz crystal microbalance (QCM) follows. The Knudsen cell will be discussed in Chapter 5.

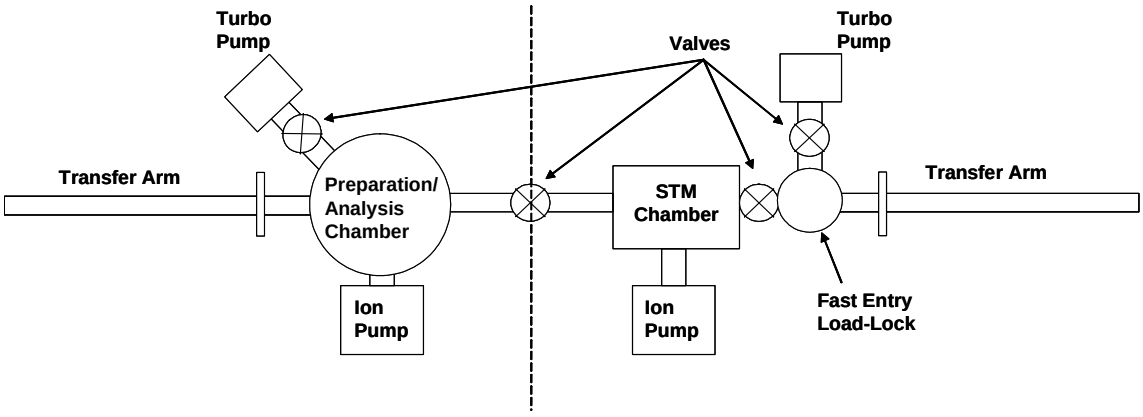

Figure 3.1: Layout of ultra-high vacuum system

3.1 Ultra-High Vacuum Scanning Tunneling Microscope

3.1.1 Ultra-High Vacuum System

The RHK UHV STM chamber is mounted on a steel frame supported by three air legs (see Figure 3.2). The air legs isolate the system from external vibrations. Isolation is required in order to prevent external vibrations from dominating the STM signal. The UHV chamber consists of a five-way 6" tube with the STM scan head manipulator mounted on the top port. The other four main ports connect to the ion pump, fast entry load-lock, sample heating/cooling system, and the preparation chamber (see Figures 3.2 and 3.6) [53] [69]. Additional ports house windows and a wobble stick for sample transfer.

The fast entry load-lock provides loading of samples/tips without breaking the vacuum of the main chamber. A fork on the end of a magnetic transfer arm within the load-lock holds the samples or tip transfer holders destined for UHV. When it is vented, the load lock is flooded with nitrogen gas to block water from adsorbing onto the walls of the load-lock. This decreases the subsequent pumpdown time. The load-lock is pumped down using a rotary and turbomolecular pump. When the load-lock reaches a pressure of approximately 10^{-8} torr, the gate valve can be opened and the samples/tips can be transferred into the main UHV chamber via the magnetic transfer arm. The wobble stick is used to move the samples/tips from the fork to either the sample stage or to a storage elevator. The sample stage is where STM analysis and tip changes occur. The storage elevator can be used to hold up to eight samples or tip transfer holders.

Achieving UHV requires a sophisticated pumping system. The pumping system for the RHK chamber consists of a rotary pump, turbomolecular pump, ion pump, and titanium sublimation pump. The rotary and turbomolecular pumps are used for the initial pumpdown of the UHV chamber. Without further treatment, the lowest achievable pressure is approximately 10^{-9} torr. UHV standards require a

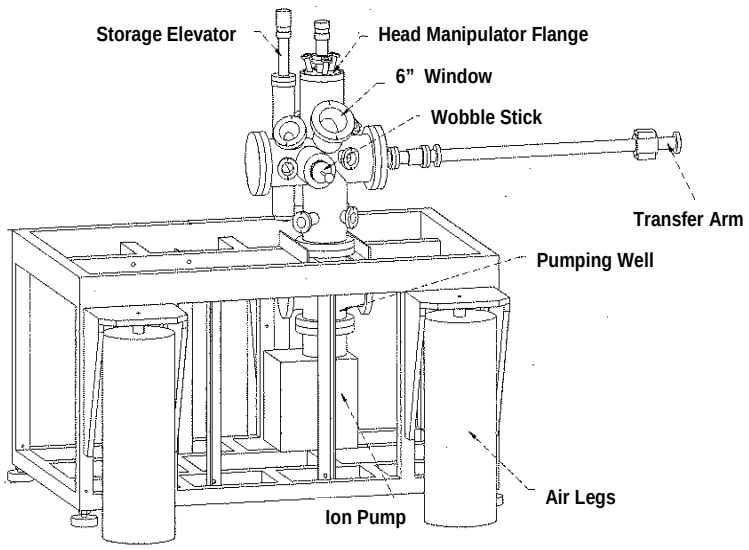

Figure 3.2: RHK UHV STM chamber. At the back is the sample heating and cooling system. Between the transfer arm and the main chamber is where the load lock is located (note that it is not shown in this figure). The unused port opposite to the transfer arm is where the preparation chamber is installed (not shown in figure). This figure was provided by RHK Technology Inc.

pressure of less than 10^{-9} torr (usually in the 10^{-10} torr range). Achieving a lower base pressure requires baking out the system to remove contaminants such as H_2O from the chamber walls [36]. Baking out the chamber consists of simultaneously heating the chamber to 140 °C and running the rotary and turbomolecular pumps for at least 12 hours. After bake out the pressure in the chamber is typically 5.0 x 10^{-10} torr. During STM operation the rotary and turbomolecular pumps have to be turned off due to the mechanical vibrations they generate. The ion pump runs silently and continuously to maintain UHV during STM operation. The titanium sublimation pump operates intermittently to assist the ion pump in maintaining UHV during STM operation [53].

3.1.2 Scanning Tunneling Microscope

There are two main parts of the STM: the scan head and sample holder, shown in Figures 3.3 and 3.4. The scan head is used to move the tip across the surface.

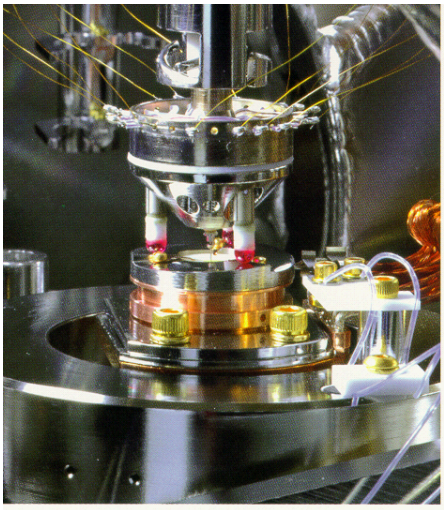

Figure 3.3: RHK UHV 300 STM. Here the scan head is approached to the sample holder. The piezo legs on the scan head are clearly visible. This figure was provided by RHK Technology Inc.

The scan head contains four piezoelectric tubes. Three of the piezoelectric tubes are mounted 120° apart with sapphire balls on the end forming the "legs" of the scan head. These legs sit on the sample holder. A fourth piezoelectric tube holds the tip in the center of the scan head. This design is of the "Walker" type, and uses the three outer piezoelectric tubes for the initial tip approach (coarse Z-positioning) and coarse X-Y positioning on the sample. The center piezoelectric tube is responsible for X, Y, and Z fine positioning and scanning.

The sample holder consists of a double grooved copper body and a helical top ramp. The two grooves are necessary for transferring the sample holder inside the UHV chamber. The wobble stick usually uses the top groove for movement of the sample holder. The bottom groove is then used to place the sample holder in the sample stage, storage elevator, or transfer arm. The helical ramp has three sections spaced 120° apart. Each ramp segment has a height of 0.75 mm. The three piezoelectric legs of the scan head each occupy one segment of the helical ramp. When a voltage is applied to the piezoelectric legs, translational motion of the legs along the ramps occurs (coarse X-Y-Z positioning). Samples for STM studies are mounted in the center of the sample holder between two sapphire washers. A thermocouple is also connected to the sample but not to the top ramp. The thermocouple connection

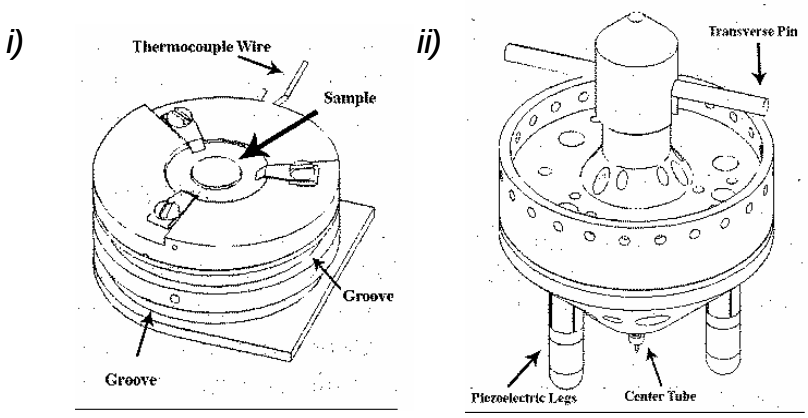

Figure 3.4: Sample holder and scan head. i) Sample holder. One groove is for the wobble stick while the other groove is used to hold the sample holder in the sample stage. The three sections of the helical ramp are also shown. The sample holder has a diameter of 25 mm and the exposed area of the sample is a disk of diameter 5 mm. ii) Scan head. There are three piezoelectric legs (one is not visible). Each leg occupies one section of the helical ramp on the sample holder. The transverse pin holds the scan head in the scan head manipulator. This figure was provided by RHK Technology Inc.

provides the sample bias voltage as well as measuring temperature.

The scan head manipulator holds the scan head and is mounted on the scan head manipulator flange (see Figure 3.2). All necessary mechanical and electrical feedthroughs are mounted on the top of the scan head manipulator. The mechanical feedthrough is used to lower the scan head onto the sample holder for scanning and to raise it for sample transfer. A series of thin wires are used to make all electrical connections to the scan head (see Figure 3.3). More detailed discussions on the laboratory components and procedures for performing STM studies can be found in the following literature [53] [69] [70] [71].

3.2 Ultra-High Vacuum Preparation Chamber

The purpose of the preparation chamber is to provide facilities for in-situ preparation and characterization of clean surfaces and ultra-thin films, which may be transferred

directly into the STM chamber under UHV conditions. During the course of this project, the preparation chamber was installed and then used for all the Knudsen cell experiments.

3.2.1 Ultra-High Vacuum System

The preparation chamber consists of a 12" diameter stainless steel sphere with 26 ports (see Figure 3.5), designed by Dr. Katie Mitchell and built by Torrovap Industries Inc. The preparation chamber is supported on the existing table frame and is connected to the RHK UHV system via a gate valve. The main components of the preparation chamber and its installation will be described below.

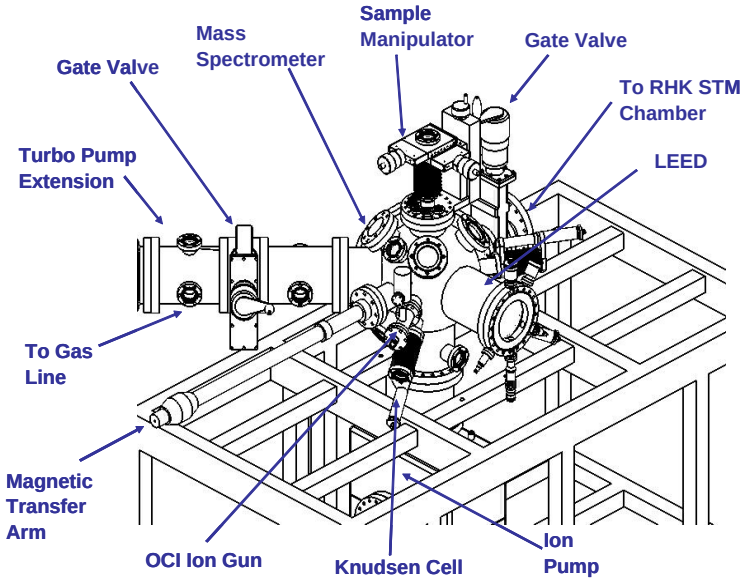

Figure 3.5: Preparation chamber mounted on the RHK frame. The STM chamber is not shown in this figure. It should be noted that the gate valve on the turbo pump extension is not actually tilted as shown in the figure. Due to external spatial contraints the Knudsen cell had to be mounted where the OCI ion gun is placed in the figure. Also not shown are the support brackets for the turbo pump extension and the RHK UHV STM chamber. This figure was drawn by Karl Molnar and provided by Torrovap Industries Inc.

A turbomolecular/backing pump combination (Varian 550l/s and Triscroll 300 Series) is used for initial pumpdown of the preparation chamber and/or gas handling

line, or for the evacuation of gases involved in sample preparation. To maintain UHV, a Gamma Vacuum 400 l/s ion pump integrated with a titanium sublimation pump is employed. This pumping system has the same capability as the system for the RHK chamber. However it is separate from the RHK pumping system, allowing both chambers to be independent of one another.

The heart of the chamber is the sample manipulator, used to position a sample for preparation and characterization, provide electrical and thermocouple connections to the sample, and to heat or cool the sample. The manipulator consists of support and feedthrough parts. Translational and rotational motion are provided by a Thermo VG Model HPT-WX 5 axis precision UHV manipulator (seen mounted on the top flange in Figures 3.5 and 3.6) The manipulator also has a docking stage for RHK sample holders. Heating, cooling and all electrical connections are provided by a custom designed manipulator head. The manipulator head was designed by fourth year engineering students under the supervision of Dr. Katie Mitchell at the University of Saskatchewan [72].

The transfer arm is mounted opposite to the RHK chamber (Figure 3.5). The fork on the end of the arm can be used to pick samples up from the manipulator and transfer them to the STM chamber. The transfer arm is a Thermo VG Model MLRM 4 magnetic linear and rotational motion drive with 24" of linear travel. There is a full 360 $^\circ$ rotation capability.

For characterization and analysis, the preparation chamber is equipped with facilities for low energy electron diffraction (LEED) and Auger electron spectroscopy (OCI Model BDL 800 LEED/Auger) and for mass spectrometry (Hiden Analytical Model HAL IV RIC PIC-RGA 301). The LEED/Auger will be used for characterization of surface and ultra-thin film structure and composition. The mass spectrometer will be used for temperature programmed desorption experiments to study molecular adsorption on surfaces. It can also be used to monitor residual gases in the chamber and as a tool for diagnosis of a leak or contaminant. In this project it was used to analyze the Knudsen cell effusion products. The mass spectrometer will be discussed in Section 3.2.2.

There are a variety of instruments for sample preparation. An ion gun (OCI Model IG70) is available for sample sputter cleaning. A gas line which can accommodate three gas bottles and can be pumped by the turbomolecular pump was designed by Dr. Andrew Robinson. It can be used to introduce gases (for example argon, nitrogen, and oxygen) to the chamber. The argon will be used for sputtering surfaces with the OCI ion gun. A quartz crystal microbalance (QCM) (discussed in Section 3.2.2) is used to measure deposition rates with the Knudsen cell, which was custom designed and installed on the side opposite to the QCM.

In the near future, a very low energy ion source will be installed on the preparation chamber. The ion source was designed by fourth year engineering students under the supervision of Dr. Andrew Robinson and Dr. Michael Bradley at the University of Saskatchewan. The goal of the ion source is to produce copper nitride self assembling nanostructures [73]. A four-pocket e-beam evaporator (Mantis Ltd. Model QUAD-EV-S) has been purchased and will also be added in the near future. It will be used for the deposition of ultra-thin metal overlayers.

During the course of this thesis project, a substantial amount of work was done installing and commissioning the preparation chamber. This work was supervised by Dr. Andrew Robinson, and assisted by Nathan Olfert, Mark Wurtz, and JJ Theron.

The ion pump and preparation chamber were mounted to the steel frame and aligned with the RHK chamber via mounting brackets (designed by myself and Nathan Olfert) built by the PEP Machine Shop. As shown in Figure 3.6, a gate valve isolates the two chambers. A stainless steel mesh (see Figure 3.7) was cut and placed at the ion pump port/preparation chamber interface. This is to prevent any sample holders dropped during transfer from falling into the ion pump. The extension pieces and gate valve for the turbo pump (see Figure 3.5) are quite heavy. Thus a support table (see Figure 3.8) for the turbo pump extension was designed by myself and Nathan Olfert and built by the PEP Machine Shop.

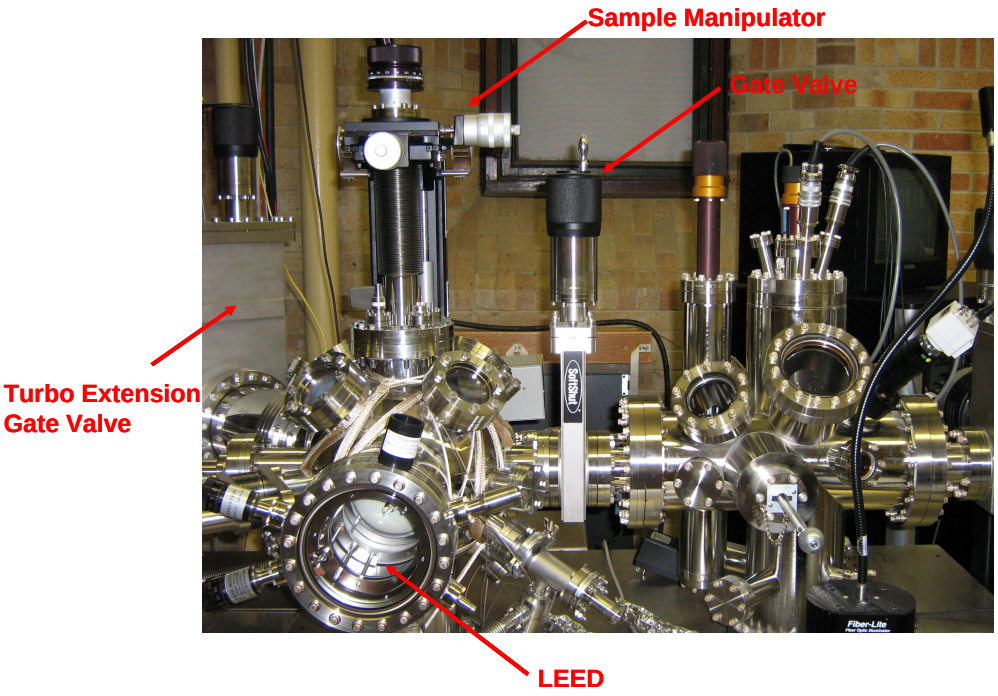

Figure 3.6: Preparation chamber (left) and RHK UHV STM chamber (right). The gate valve can be used to isolate the two chambers.

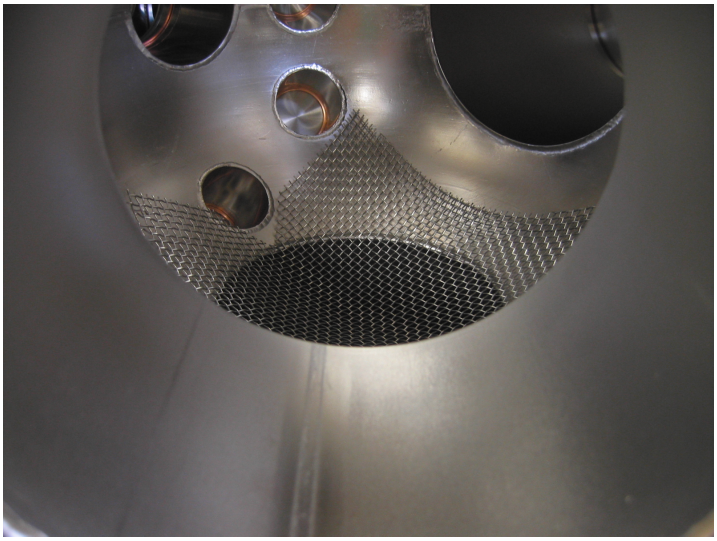

Figure 3.7: Stainless steel mesh isolating preparation chamber from ion pump

The turbo pump extension and gate valve, turbo pump, transfer arm, sample head manipulator, LEED, mass spectrometer, quartz crystal microbalance, OCI ion gun, and gas handling line were all installed on the preparation chamber. After the installation of every two or three components, the chamber was pumped down and leak tests were performed on newly sealed flanges. Leak testing consisted of squirting isopropyl alcohol on the flange of interest. If no pressure increase was present, the leak test was considered successful. After pumping down overnight, the pressure was typically 4.6 x 10^{-9} torr.

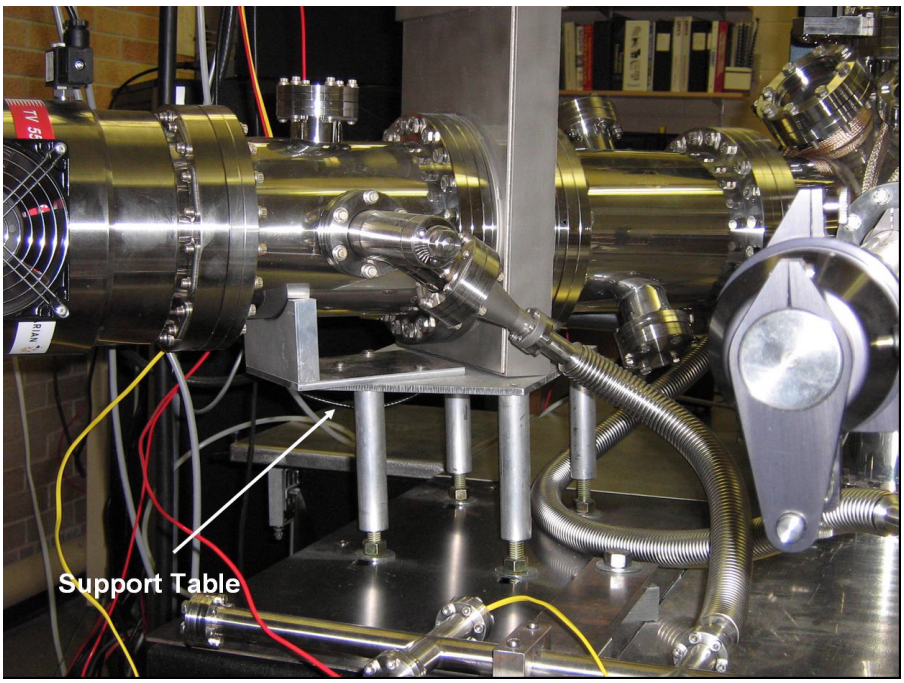

Figure 3.8: Support table for turbo pump extension on preparation chamber. An aluminum table rests on a sheet of steel (0.125" thick) bolted to the main frame.

As for the STM chamber, pumping the preparation chamber down to UHV requires bakeout. The addition of the preparation chamber to the steel frame required modification to the bakeout shield. Parts of the shield had to be cut and sewn to accommodate extensions that protrude beyond the steel frame. Parts that protruded were the turbo pump, mass spectrometer and transfer arm. JJ Theron assisted in the modification of the bakeout shield. After bakeout at 110 °C for 24 hours,

a pressure of 6.0 x 10^{-10} torr was obtained, meeting the design requirement for the UHV chamber.

3.2.2 Quartz Crystal Microbalance and Mass Spectrometer

Sublimation experiments were performed using the Knudsen cell (K-cell), quartz crystal microbalance (QCM), and mass spectrometer. The layout of the experiment is shown in Figure 3.9. These instruments are installed in the horizontal plane, with center lines meeting at the chamber center. The linear feedthroughs are used to position and retract each instrument. The QCM can be moved to the sample position (intersection of dotted red lines in Figure 3.9) for deposition calibration. When performing deposition experiments, both the QCM and K-cell feedthroughs were fully compressed. This resulted in a source-sample separation of $L = 15\,\text{mm}$. During mass spectrometer experiments, the K-cell was fully compressed while the mass spectrometer was compressed as far as possible without direct contact with the K-cell.

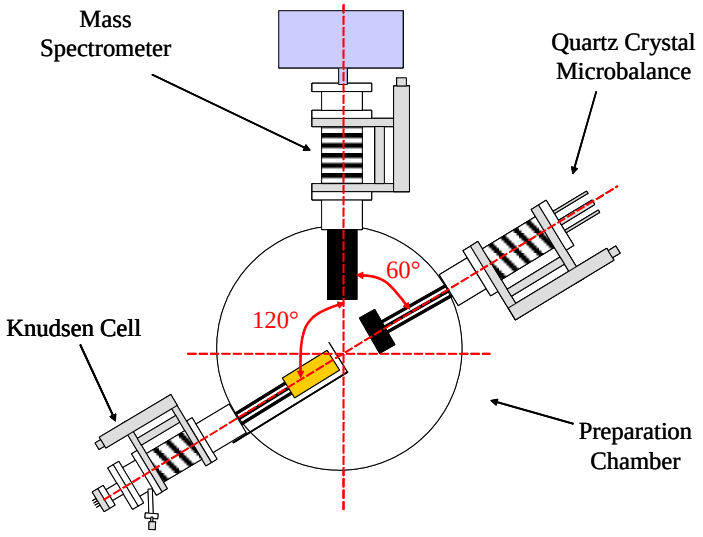

Figure 3.9: Experimental setup. Top view of preparation chamber showing the position of the K-cell, QCM and mass spectrometer. Linear positions of all components inside the preparation chamber are variable. Note that the preparation chamber is 12" in diameter. Both the K-cell and QCM ports have flange face to chamber center distances of 210 mm.

Deposition rate was measured using an SQM-150 QCM purchased from Sigma Instruments. When not in use, the QCM can be fully retracted. As discussed in Section 2.4.2, the QCM operates based on the change of resonant frequency of a vibrating quartz crystal due to added mass. A schematic of the QCM is shown in Figure 3.10. If the volume density of the material undergoing deposition is input to the control box, the deposition rate is displayed in Angstroms per second. The sensor is a 14 mm diameter gold coated quartz plate. When mounted in the QCM, the sensor has an exposed diameter of 8.5 mm. The sensor crystal must be changed when the crystal life on the control box displays a value of 70% or lower. The two outside connections are for liquid cooling of the sensor (not used in this experiment) while the inner connection is a coaxial electrical connection [74].

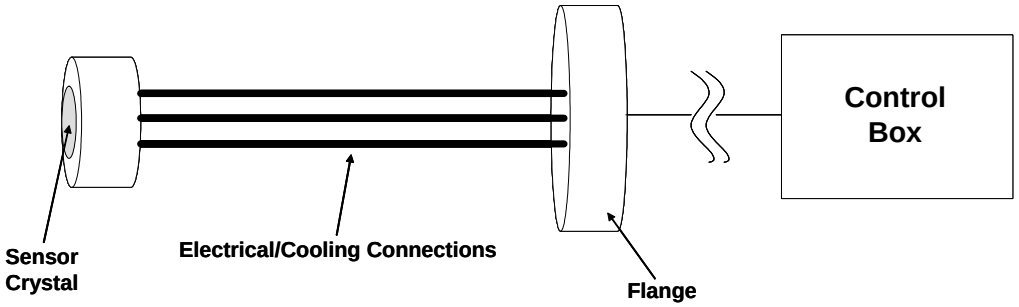

Figure 3.10: Schematic of Sigma Instruments quartz crystal microbalance. The distance from the flange to the end of the sensor is 263 mm.

In this project, mass spectra of L-cysteine and L-methionine were measured with the model HAL IV RIC PIC-RGA 301 Hiden Analytical electron impact (EI) quadrupole mass spectrometer (see Figures 3.11 and 3.12). A mass spectrometer works by measuring the mass-to-charge (m/z) ratio of ionized molecules. In an EI mass spectrometer, molecules are ionized via collisions with electrons from a heater filament. The electrons are accelerated to a specified kinetic energy (impact energy) into the molecules of interest. Mass-to-charge ratios that are not of interest are filtered out with a quadrupole filter. The principle of a quadrupole mass spectrometer is shown in Figure 3.13. Ions from the source pass through the quadrupole filter. Only ions of certain m/z ratios pass through the filter to the detector. The permitted m/z

ratio is governed by the AC and DC voltages. By changing the applied voltages, a range of desired m/z ratios can be scanned [75].

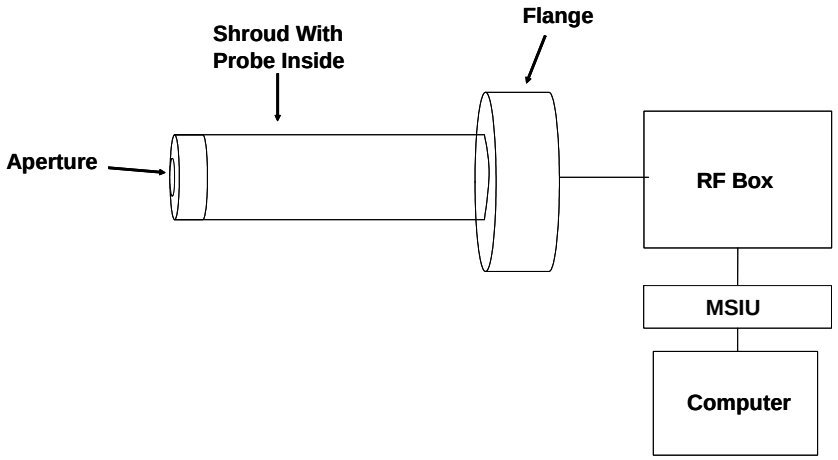

Figure 3.11: Schematic diagram of mass spectrometer setup. RF (radio frequency). MSIU (mass spectrometer interface unit). Distance from the flange to the end of the probe is 308 mm.

The Hiden Analytical mass spectrometer has a Residual Gas Analysis ionizer, a quadrupole mass filter, and an ion counting Secondary Electron Multiplier detector. A schematic of the mass spectrometer setup is shown in Figure 3.11. The radio frequency (RF) box contains signal conditioning electronics, the power supply for the quadrupole mass filter, and wiring to connect Mass Spectrometer Interface Unit (MSIU) signals to the probe. The MSIU contains a communications interface for linking the user to the system via a computer. The mass spectrometer has a scan range of up to 300 *amu*. Mass ranges and impact energies can be entered by the user with the computer in the MASoft program [76] [77].

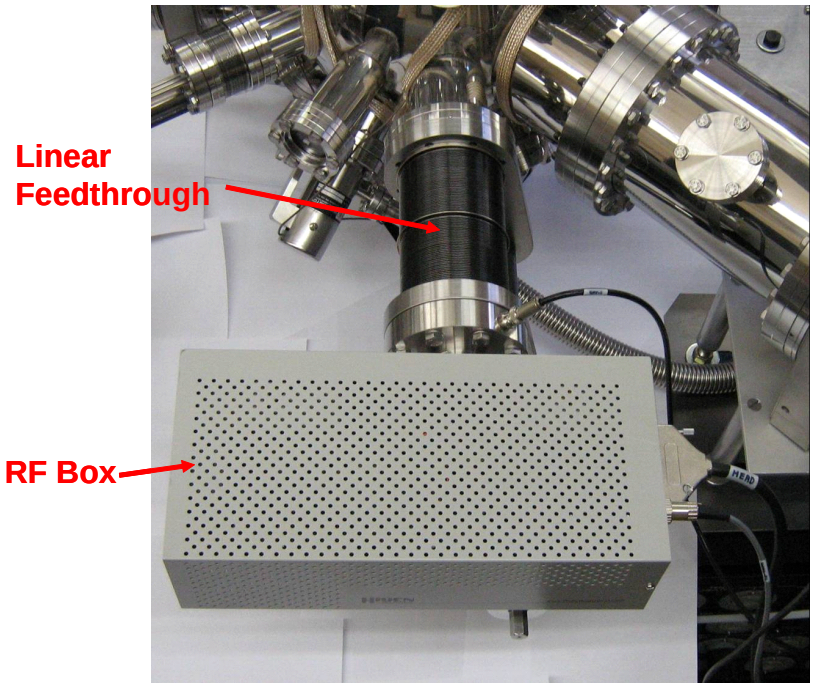

Figure 3.12: Hiden Analytical electron impact mass spectrometer mounted on the preparation chamber.

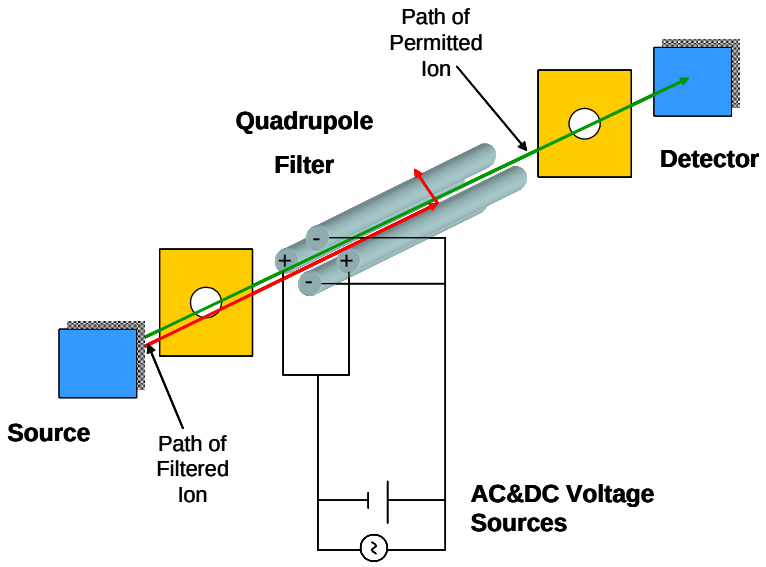

Figure 3.13: Electron impact quadropole mass spectrometer

Chapter 4

Scanning Tunneling Microscopy Study of Au(111)

A scanning tunneling microscopy (STM) study of clean Au(111) thin films was performed in order to evaluate their suitability for amino acid adsorption experiments and to acquire expertise in obtaining high resolution STM images of these surfaces. In this chapter, the preparation of the Au(111) thin films will be described, followed by a presentation of the STM results obtained, and a discussion of optimal imaging conditions.

4.1 Sample Preparation

A single crystal Au(111) surface is ideal for STM analysis since it can be cleaned in UHV, minimizing contamination [44]. However, preparation of the single crystal surface requires ion bombardment and annealing, and low energy electron diffraction for characterizing the clean surface. At the time the STM experiments were performed, these facilities were not yet available. A gold surface suitable for STM can also be produced by evaporating a thin film of gold onto a cleaved mica surface. Thin films can either be made in the lab or purchased from a commercial supplier. The feasibility of producing in-house thin films, as opposed to purchasing them commercially, was investigated.

4.1.1 Homemade Au(111) Samples

Mica substrates were acquired from Dr. Matthew Paige (Dept. of Chemistry). Before evaporation, the mica was cleaved with scotch tape. This helps produce a large (tens of microns), atomically flat substrate for Au(111) [78].

The samples were then taken to a high vacuum thermal evaporation chamber provided by Dr. Stephen Urquhart (Dept. of Chemistry). With the aid of Edwige Otero, a layer 95nm thick of 99.9985% pure gold (Alpha Aesar) was evaporated onto the cleaved mica substrates. The samples were then annealed in a hydrogen flame with the aid of Dr. Chenzhong Li (Dept. of Biochemistry). After the annealing procedure, the samples were quenched in ethanol and dried in a stream of nitrogen, then transferred into a sample holder and placed in the UHV STM chamber. This sample annealing procedure has been shown to produce contaminant free, highly-ordered Au(111) surfaces [79].

4.1.2 Commercial Au(111) Samples

Prepared Au(111) samples were purchased from Molecular Imaging Corporation. The samples consist of a mica surface (1.4 cm x 1.1 cm) with 1500 Å of gold covering an area of 1.0 cm x 1.1 cm. The samples are annealed in a hydrogen flame and packed in pure nitrogen before shipping. Before samples could be imaged using UHV STM, they had to be cut to appropriate size for mounting in the sample holder. The RHK sample holders have a 1.0 cm diameter space available for sample mounting (see Figure 3.4). The Au thin films were extremely fragile; simply using a utility knife or scissors resulted in the Au thin film peeling off the mica substrate, damaging the film and yielding an unreliable electrical connection for STM analysis.

The commercial samples were taken to the Dept. of Geological Science (Jainzhong Fan) for cutting with a laser. As shown in Figure 4.1, the Au suffered significant heat damage. The laser also had inadequate power to penetrate the mica substrate. Running the laser over the same area repeatedly would eventually penetrate the mica substrate. However, the heat damage made the Au(111) sample unsuitable for UHV

STM studies.

Finally, Nathan Olfert and I designed a "guillotine" style cutter as shown in Figure 4.2. This provided suitable cuts for mounting the commercial Au(111) samples.

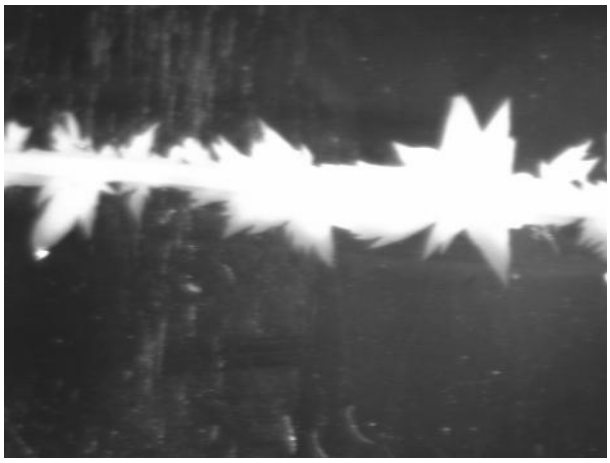

Figure 4.1: Cutting line of Au(111) with laser. The laser has a beam size of 100μm and a wavelength of 266nm. Image size is approximately 2.0 mm x 1.5 mm.

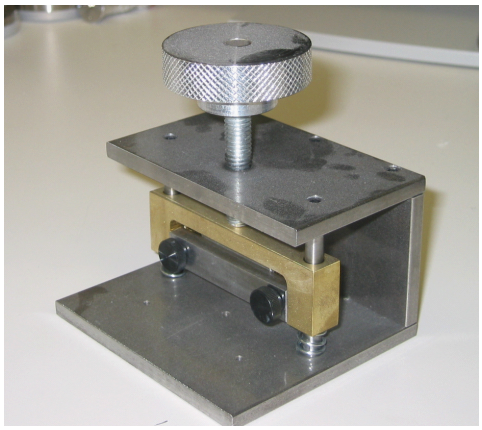

Figure 4.2: "Guillotine" cutter. A razor blade is clamped in between the steel support and brass guide (tightened with black knobs). The Au sample is placed on a piece of acrylic underneath the razor blade. The blade is brought down by turning the knob on top.

4.2 Results and Discussion

STM imaging was performed using a tungsten tip etched in $3M$ sodium hydroxide aqueous solution. After etching, the tip was rinsed in distilled water to remove sodium hydroxide crystals followed by isopropyl alcohol to remove water, and transferred into the STM chamber [80] [53]. After mounting, the samples were transferred into UHV and scanned without further preparation. Base pressure during scanning was in the low 10^{-9} torr to 10^{-10} torr range.

4.2.1 Homemade Au(111) Samples

A UHV STM image of the homemade Au(111) film is shown in Figure 4.3. We were unable to obtain well-resolved images of the surface, and no flat terraces, "herringbone" reconstruction or atomic resolution was seen. As shown in Figure 4.4, the surface is quite rough and lacks the large flat terraces necessary for meaningful adsorption studies. The poor surface quality is likely due to preparation conditions such as contamination of the evaporation chamber and the lack of heating of the mica substrate during evaporation, which was not available in the Dept. of Chemistry. It was thus concluded that the homemade Au(111)/mica substrates were not suitable for adsorption studies.

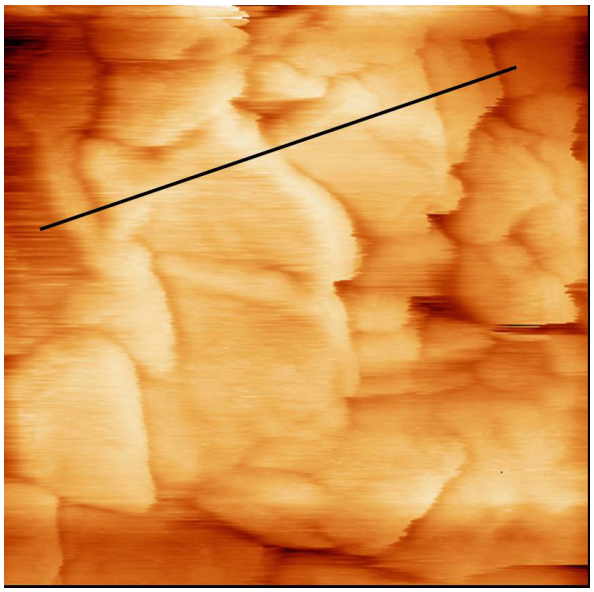

Figure 4.3: 5000 Å x 5000 Å UHV STM image of the homemade Au(111) surface at a tunneling current of 0.95 nA and a bias voltage of 0.55 V. The surface contains some triangular features as expected from the hexagonal symmetry of Au(111) [44], but the overall surface quality is poor.

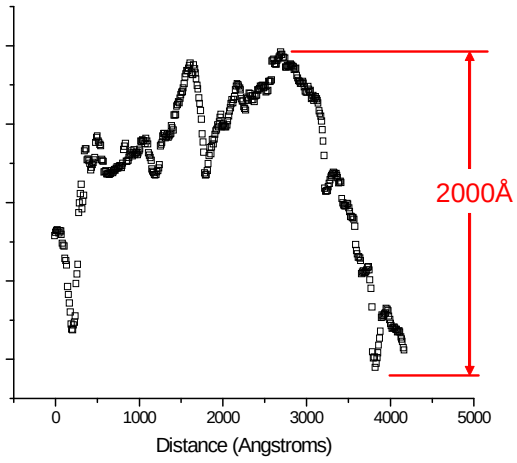

Figure 4.4: Cross section of STM image of homemade Au(111). The graph follows the black line in Figure 4.3 from left-to-right. Note that the surface corrugation is very large.

4.2.2 Commercial Au(111) Samples

High resolution images were acquired from Molecular Imaging Corporation's Au(111)/mica samples. Figure 4.5 shows large flat terraces and atomic steps. As shown in Figure 4.6, the atomic steps are approximately 2.5 Å high as expected [81]. Figure 4.5 also shows step edges oriented at 60° and 120° to each other, characteristic of a (111) oriented FCC crystal [82].

The Au(111) samples from Molecular Imaging Corporation produced high resolution images showing the expected "herringbone" reconstruction (Figure 4.7) [32] [35]. The corrugation lines of the "herringbone" reconstruction had paired separation distances of 63 ± 3 Å while the individual lines within a pair had separations of 43 ± 3 Å. These values are in agreement with the 64 Å for pair separation and 44 Å individual (within a pair) separation observed by Barth *et. al.* [33]. The pair separation is also in agreement with the 63.4 Å length of the (22 x $\sqrt{3}$) unit cell along $[1\bar{1}0]$ in Figure 2.7.

Figure 4.8 shows individual atoms on a Au(111) surface. The average spacing in between atoms is 2.66 ± 0.11 Å. This is smaller than the ideal unreconstructed 2.88 Å atomic spacing for Au(111) [34]. This can be expected as surface atoms on a Au(111) reconstructed surface are packed more densely than on an ideally terminated surface [32]. The atoms in Figure 4.8 also exhibit a distorted hexagonal arrangement. The distortion in the hexagonal pattern is partly due to drift in the piezo tubes on the STM and partly to the reconstruction of the surface.

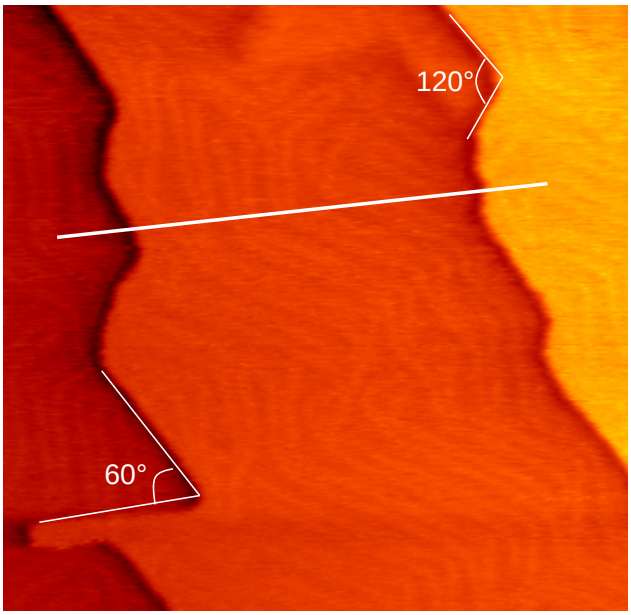

Figure 4.5: 1000 Å x 1000 Å STM image of Au(111) with a bias voltage of 0.025 V and a tunneling current of 1.15 nA. Several terraces are seen in this image and the "herringbone" reconstruction is faintly visible on the terraces. Step edges are seen to meet at characteristic angles of 60 ° and 120 °.

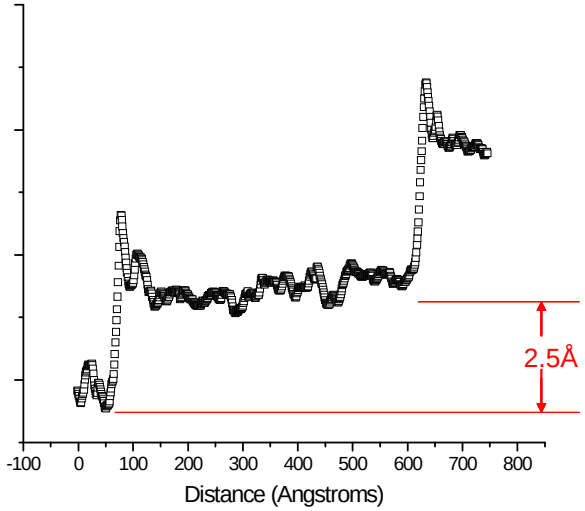

Figure 4.6: Cross section showing atomic steps on Au(111). The graph follows the white line in Figure 4.5 from left-to-right. The large peaks at the edge of each step arise from the response of the feedback loop as the tip passes over the step edge. The smaller oscillations in between are due to the "herringbone" reconstruction.

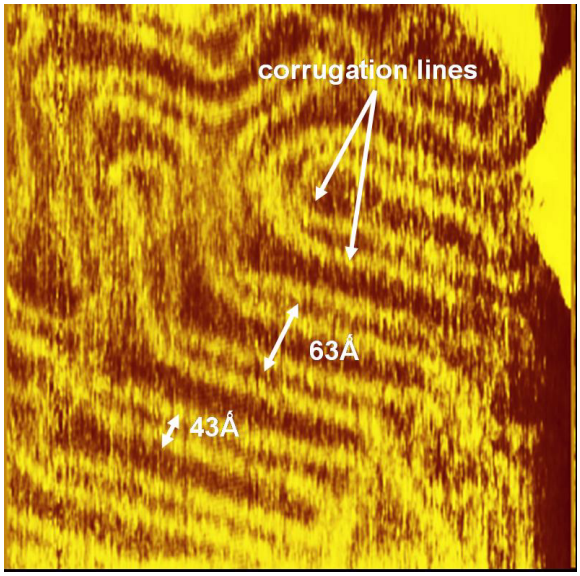

Figure 4.7: Enlarged section of Figure 4.5. Image size is 500 Å x 500 Å. Corrugation lines for "herringbone" reconstruction are clearly visible. The separation distances are in agreement with those observed by other research groups [33].

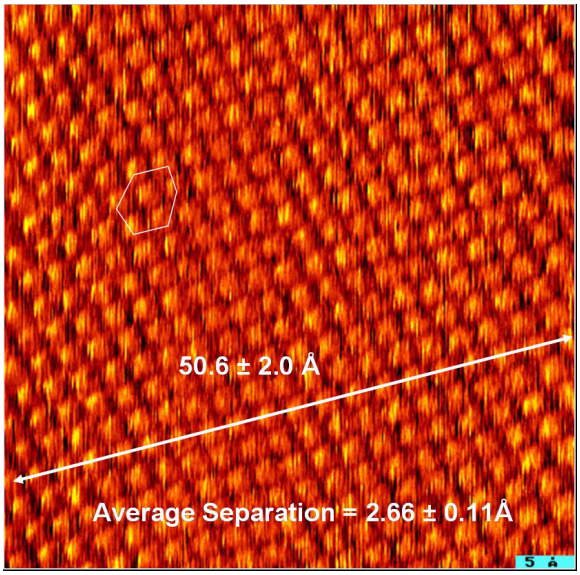

Figure 4.8: 50 Å x 50 Å image of individual atoms on a Au(111)/mica surface purchased from Molecular Imaging Corporation (bias voltage of 0.090 V and tunneling current of 1.09 nA). The average atomic separation along the line is 2.66 ± 0.11 Å.

4.2.3 Optimal Conditions for Imaging Au(111)

When imaging Au(111) there were some common factors that improved the chances of acquiring clear images. The conditions required for large survey images and for high resolution images will be discussed below. Note that the tunneling current was always set between 0.9 nA and 1.2 nA.

Imaging large flat terraces on Au(111) generally had a high success rate. The success of acquiring larger images of flat triangular terraces did not change when imaging in UHV (10^{-10} torr) or HV (10^{-8} torr). Higher bias voltages (≈ 0.5 V) had a tendency to produce images of larger surfaces with an equal success rate to that of lower bias voltages.

Acquiring high resolution images of individual atoms and "herringbone" reconstruction had a much lower success rate than that for the low resolution images. Certain conditions and parameters always had to be met to have any chance of success. While gold is relatively inert and does not necessarily require UHV conditions, high resolution imaging was only successful when performed in a baked chamber meeting UHV requirements. A low bias voltage (tens of mV) was necessary for producing high resolution images of "herringbone" reconstruction or individual atoms. This can be expected because a low bias voltage brings the tip close to the surface. From Tersoff and Hamann's theory (equation 2.13) for a metal like Au(111), the corrugation amplitude will increase with decreasing tip-sample separation, allowing the structure to be resolved. For successful high resolution imaging, a fast scan speed ($30 - 50$ ms/$line$) was always necessary, along with a maximum setting on the z position A/D gain.

Scanning tunneling microscopy is a delicate scientific practice. Imaging under the same conditions that produced successful images in the past will not necessarily produce images of the same degree of success in the present. However, the chances of successful Au(111) STM images can be increased by following the measures outlined above.

Chapter 5

Knudsen Cell

A Knudsen cell (K-cell) was custom designed for this project, to provide controlled deposition of L-cysteine and L-methionine on Au(111). In this chapter, the design requirements and final design are described, along with suggestions for future improvements.

5.1 Design Requirements

The purpose of the K-cell is to heat an amino acid powder to a reproducible, stable temperature, such that the amino acid sublimes and effuses from the oven according to the Knudsen Cosine Law. Amino acids, commercially available in powders, decompose thermally in the temperature range 448 K to 615 K, with L-cysteine at 448 K and L-methionine at 556 K (see Table D.1) [38] [83]. The K-cell must be optimized to provide controlled heating of amino acid powders below their decomposition temperatures, and in a temperature range where adequate sublimation can be achieved. Even for L-methionine, whose decomposition temperature is near the top end of the range, adequate sublimation can be obtained at approximately 400 K (see Chapter 6), so a temperature range of room temperature to 425 K is optimal.

In order to study coverage dependent behavior of amino acids on metal surfaces, such as Au(111), it is desirable to deposit known coverages from submonolayer (say 0.25 ML) up to a few monolayers. Here, a full monolayer is defined as one adsorbate atom per substrate atom. To provide reproducible low coverages such as these, one needs controlled low deposition rates less than approximately 0.2 Å/ s, as shown in Figure 5.1. The deposition rate is given by equations 2.26 and 2.22. These equations

show that the deposition rate depends strongly on temperature. Thus the K-cell must provide a reproducible and stable temperature ($\pm 0.5\,\mathrm{K}$).

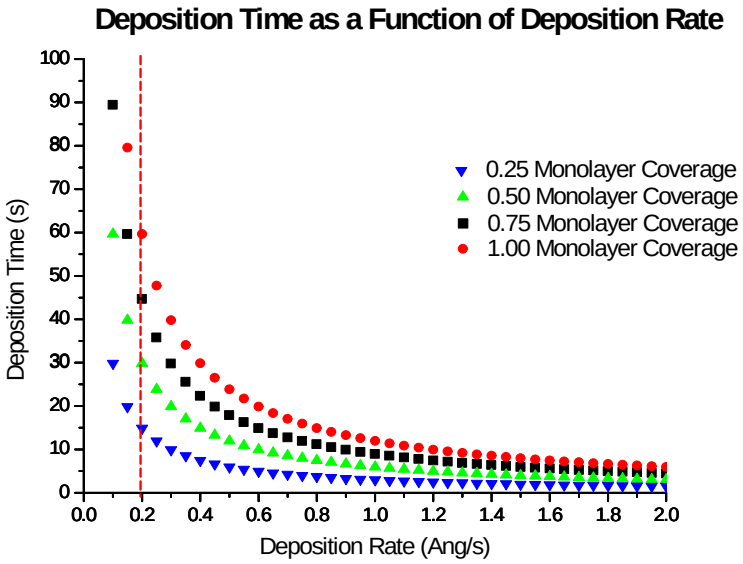

Figure 5.1: Graph of deposition time as a function of deposition rate for various monolayer coverages. At a deposition rate of $0.2\,\text{Å}/\,\mathrm{s}$, 0.25 ML is deposited in 15 s. The dashed line is drawn as a guide to the eye. Here, a full monolayer is defined as one adsorbate atom per substrate atom.

The sample in the RHK holder has an exposed diameter of 5 mm and will be located at the chamber center (see Figure 3.9). The QCM sensor has an effective diameter of 8.5 mm, and will also be located at the chamber center when in use. Table 5.1 shows the value of the exit angle θ subtended at the sample or sensor edge and of $\cos\theta$ for several source-sample distances L (see Figure 5.2). For $L > 15\,\mathrm{mm}$, $\cos\theta > 0.95$ for both the sample and QCM. From the Knudsen Cosine Law (equation 2.26) we see that the flux of molecules at the edge of the sample/QCM will differ by less than 5% compared to that at the center, leading to even coverage. A larger L gives more even coverage, but also more unwanted deposition on the surroundings. L should ideally be variable across the range $15 - 100\,\mathrm{mm}$ so that the source-sample distance can be optimized, the deposition rate varied (see equations 2.26 and 2.22),

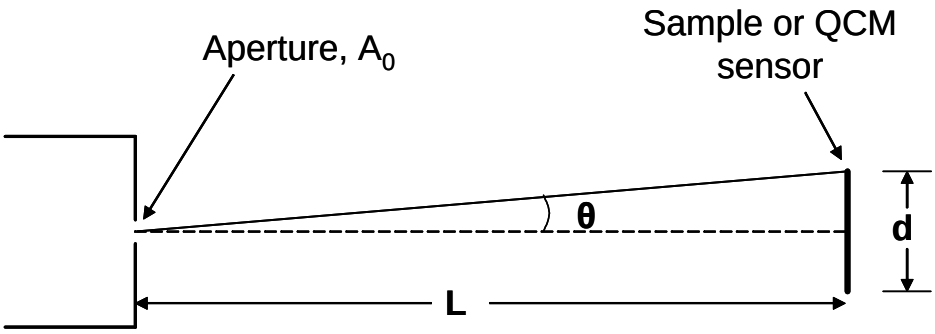

Figure 5.2: Deposition source and sample separation. Here L is the source-sample distance and d is the sample/QCM diameter. For the sample $d = 5\,\text{mm}$ and for the QCM $d = 8.5\,\text{mm}$.

and the K-cell retracted when not in use. It is also desirable to be able to vary A_0 since this provides independent variation of the deposition rate (see equation 2.26). The center line of the K-cell should be aligned with the center line of the sample/QCM, but a small (on the order of 1 mm) misalignment is not critical since $\cos\theta$ changes very slowly in the range $0 - 25\,^\circ$.

Table 5.1: Effects of source-sample distance on the $\cos\theta$ term in the Knudsen Cosine Law. θ_1 and θ_2 are the angles subtended at the edges of the sample and QCM sensor respectively (see Figure 5.2).

Distance L (mm)	**Sample** θ_1 (°)	**cos**θ_1	**QCM** θ_2 (°)	**cos**θ_2
5	26.6	0.90	40.4	0.77
10	14.0	0.97	23.0	0.92
15	9.5	0.99	16.8	0.96
20	7.1	0.99	12.0	0.98
25	5.7	1.00	9.6	0.99
30	4.8	1.00	8.1	0.99

A shutter is required on the K-cell to start and stop depositions, so they can last for a well defined time. The shutter will also reduce unwanted deposition on other parts of the chamber or equipment.

The K-cell must be mounted on a 2.75" flange, to be compatible with the appropriate port on the UHV preparation chamber. The K-cell must also be fully retractable when not in use, so as not to interfere with other equipment in the chamber.

For convenience, the K-cell must be easy to use. It must be easy to control during operation and easy to assemble and disassemble during maintenance. Maintenance includes refilling/changing the source material and cleaning of components. The K-cell must also be easy to modify if necessary. For these purposes, it is desirable for the K-cell components to be modular.

A critical factor in the design of the K-cell is that all components be ultra-high vacuum (UHV) compatible, since it will be installed in the UHV preparation chamber. This imposes severe limitations on the materials available for the K-cell design. Many common electrical and construction materials (even some metals) are not UHV compatible. Materials such as zinc, solder and plastic have high outgassing rates (high vapour pressure) and cannot be used in UHV. Appropriate materials include stainless steel, oxygen-free high conductivity (OFHC) copper, and ceramic to name a few. In addition to being UHV compatible, materials must also have low outgassing rates at the temperatures used during K-cell heating and bakeout (up to 425 K).

5.2 Final Design

The K-cell was originally based on the design of Hutchings *et al.* for a K-cell for evaporation of organic materials in the 450 K temperature range [65]. Modifications were made to this design to suit our experimental setup.

A schematic diagram of the final design is shown in Figure 5.3. The K-cell consists of the following components: Knudsen oven, electrical connections and

feedthrough, physical supports (support rods and collars, reducer flange), shutter assembly (shutter, spring, rotary feedthrough, cluster flange), and linear motion drive. Each of these components will be described in turn.

The Knudsen oven can be viewed in Figure 5.4. The Knudsen oven of consists of: oven body, aperture, heater wire and insulation, back and front caps, and connections for heater and thermocouple wire. The oven components were machined by the PEP machine shop out of oxygen free high conductivity (OFHC) copper. This material was chosen because of its high thermal conductivity and UHV compatibility [65]. Dimensions and drawings of each of the components of the oven can be found in Appendix A. The Knudsen oven has a brick shape body approximately 1.5" x 0.75" x 0.75" in size (see Figure 5.4(i)). This shape was chosen for its ability to provide electrical/physical isolation between the heater wire and the oven body. A cylindrical cavity of diameter 0.25" and depth 1.25" is machined into the oven body and can be loaded with amino acid powder.

The aperture is a circular disc 0.438" in diameter and 0.063" thick, with the aperture hole directly in the center. Three aperture discs were machined, with apertures of diameter 1 mm, 2 mm, and 3 mm. To secure the aperture in place, a circular slot was cut into the front of the Knudsen oven. The cap on the front of the oven body holds the aperture in the slot. The Knudsen oven assembly can be viewed in Figure 5.4(ii).

Heating is provided resistively via Ni40Cr60 wire (resistivity per unit length of 1.71 Ω/ m) with a 0.032" diameter (Mor Electric Heating Assoc., Inc.). The total resistance of the heating circuit is 1.6 Ω. Isolation of the heater wire is provided with ceramic tubes (1.5" long and 0.125" diameter) placed at each of the four long edges of the oven. The heater wire is wrapped tightly around the ceramic tubes. Protrusion of the ceramic tubes above the four corners prevents the heater wire from making physical/electrical contact with the oven body. The ceramic tubes are secured via the two oven caps (see Figure A.3) that are screwed onto the ends of the Knudsen oven (see Figure 5.4(ii)). The heater wire is also clamped at each end between two sheets of mica to the Knudsen oven with a copper plate (see Figure

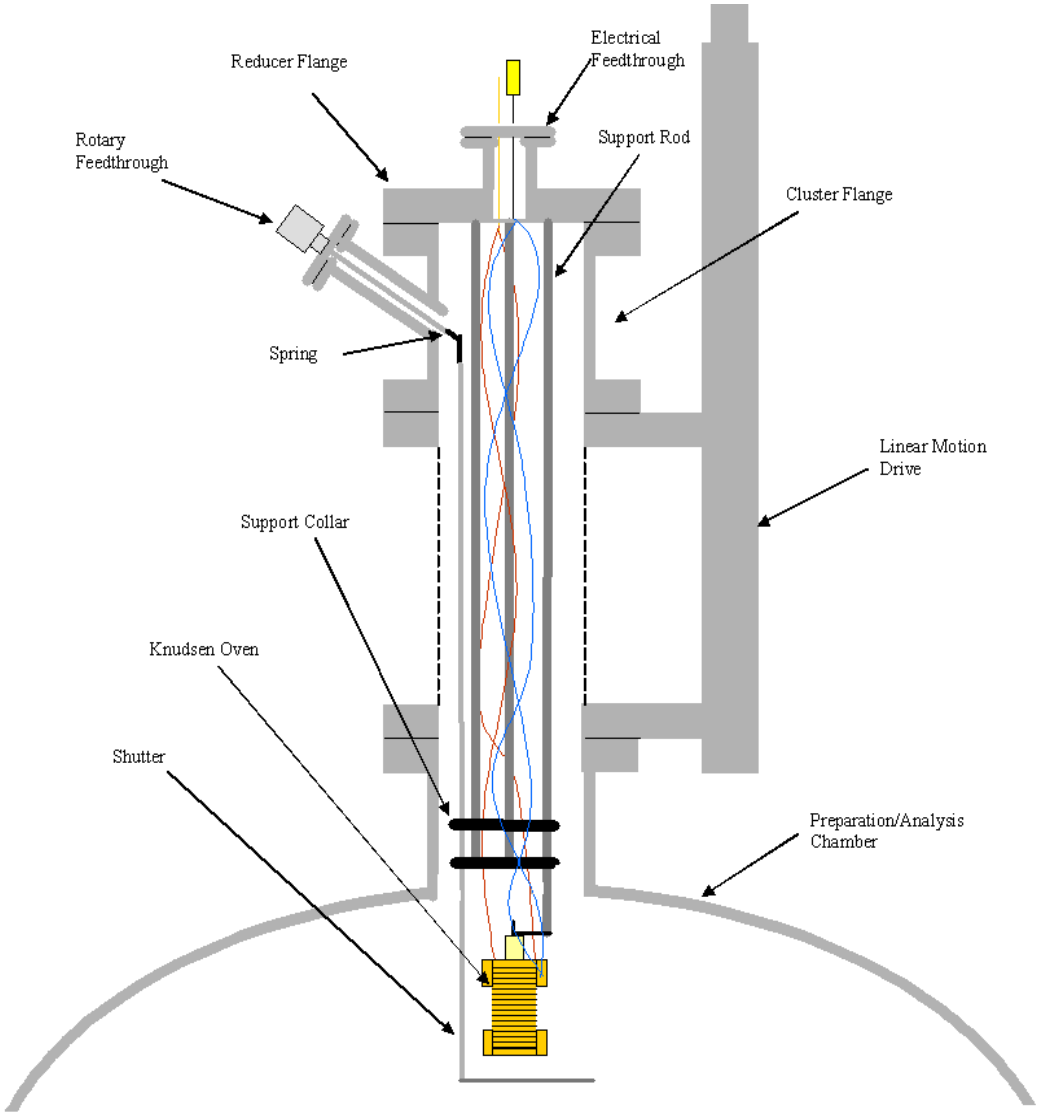

Figure 5.3: Cross section of K-cell mounted on the UHV chamber. The red and blue lines represent heater and thermocouple wires respectively. The length of the assembly from the face of the reducer flange to the far end of the Knudsen oven is 337 mm. The separation from the far end of the Knudsen oven to the shutter is 15 mm. All of the components are described in the text.

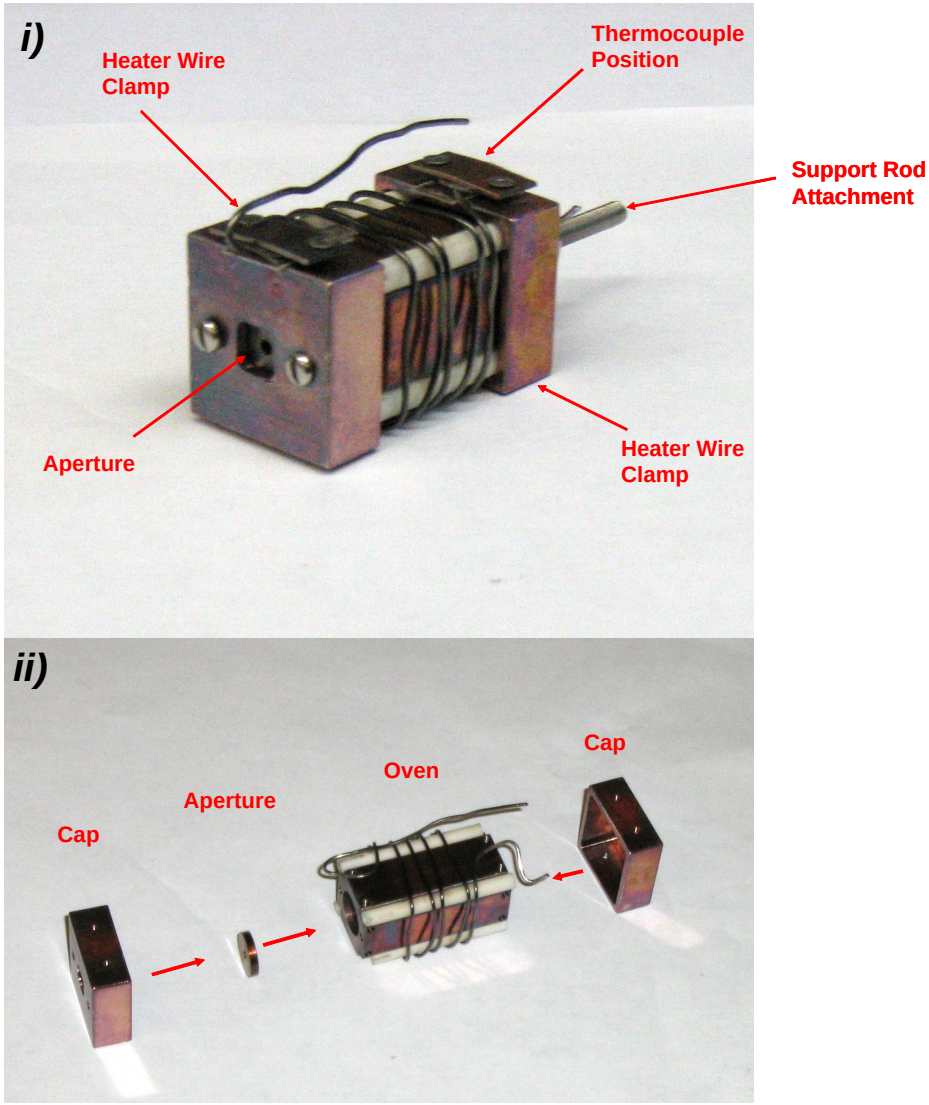

Figure 5.4: The Knudsen oven. *i)* Fully assembled. The oven body is 1.5" x 0.75" x 0.75" in size. *ii)* Assembly of Knudsen oven.

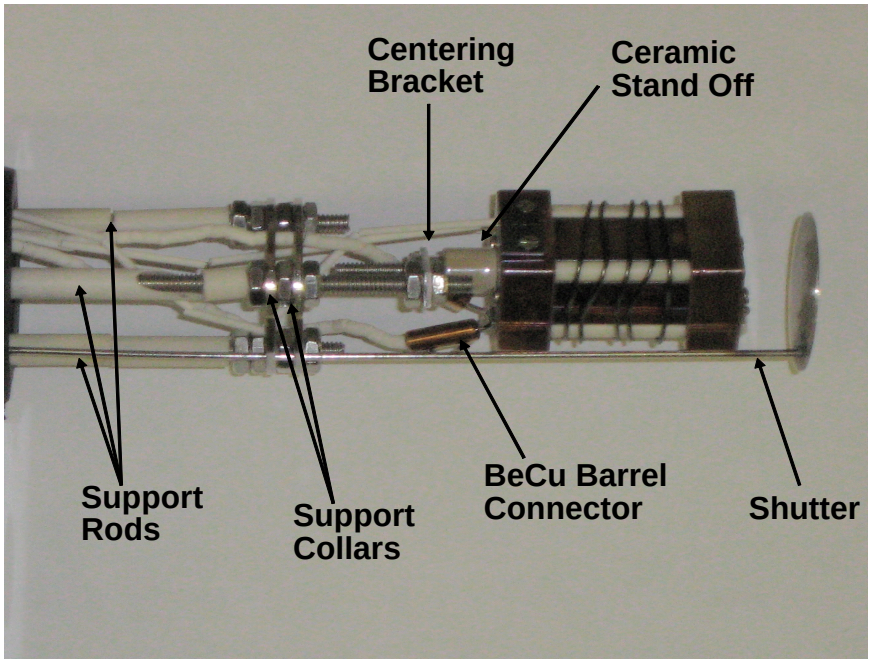

Figure 5.5: Knudsen cell completely assembled and mounted

A.5 for dimensions) as shown in Figure 5.4(i). The mica is required for electrical isolation. All screws used to secure components of the oven are made of stainless steel.

Beryllium copper (BeCu) barrel connectors are attached to the ends of the heater wire to connect the heater wire to the power lines (see Figures 5.4(i) and 5.5). The power lines consist of 0.032" copper wire insulated with ceramic beads.

The thermocouple wire is 0.01" diameter type K. Up to the junction, the wire is insulated with ceramic tubing. The junction is simply the two thermocouple wires twisted together, and it is secured to the back of the Knudsen oven with a copper plate (see Figure 5.4i). The power lines and thermocouple wires were connected to the electrical feedthrough with BeCu barrel connectors.

The electrical feedthrough (see Figures 5.3 and 5.7, Datacomp Electronics Model $T31K1231502$) has both power (rated for 15 A and 1000 V) and type K thermocouple inputs on a 1.33" flange. The power input was insulated with ceramic beads. It should be noted that ceramic is an ideal insulator in UHV because it has low

outgassing rates. All wire, connectors and ceramics were ordered from Kurt J. Lesker and Datacomp Electronics. Power for the K-cell is provided by a Lambda Model GEN30-25 power supply (current range $0-25\,\mathrm{A}$ and voltage range $0-30\,\mathrm{V}$).

A custom designed 2.75" - 1.33" reducer flange (see Figures 5.6 and 5.7) accommodates the electrical feedthrough and provides base support for the Knudsen oven. The reducer flange was built by Datacomp Electronics. One 12" and two 10.5" length threaded stainless steel rods (0.188" diameter) are screwed into the reducer flange to provide support for the oven. Their positions on the flange form the vertices of an equilateral triangle. The support rods are encased in ceramic tubing to prevent electrical contact with the power lines and to provide additional strength. Two circular stainless steel support collars (see Figure A.6) are mounted to all three rods to provide stiffness and as a guide for the wires and shutter (see Figure 5.5). The support collars are attached to each of the support rods with two nuts. All supports are designed to fit through the 1.5" bore of the 2.75" flange. The lengths of the support rods were chosen to allow positioning from out of the way to a source-sample distance $L = 15\,\mathrm{mm}$. The three rods and support collars are necessary to support this long length (see Appendix C). A stainless steel centering bracket is used to attach the Knudsen oven assembly to the 12" support rod. The centering bracket is clamped to the support rod with two nuts (see Figure 5.5). The Knudsen oven assembly is attached to the centering bracket with two nuts as well (see Figure 5.5). As shown in Figure 5.5, attached to the Knudsen oven assembly is a ceramic stand off. This stand off provides electrical isolation of the assembly from the rest of the chamber.

The shutter is a 1.33" diameter stainless steel disk (0.031" thick) welded to the end of a 10" long stainless steel rod (0.125" diameter). The rod passes through two holes in the support collars that hold it in place and guide its motion. Transfer of motion to this rod from a rotary feedthrough (MDC Vacuum Products Model $HTBRM-133$, see Figure 5.7) mounted on a custom designed cluster flange (see Figures 5.6 and 5.7) is provided by a stainless steel spring (PEP machine shop). Initially, a stainless steel universal joint provided manipulation. However the universal

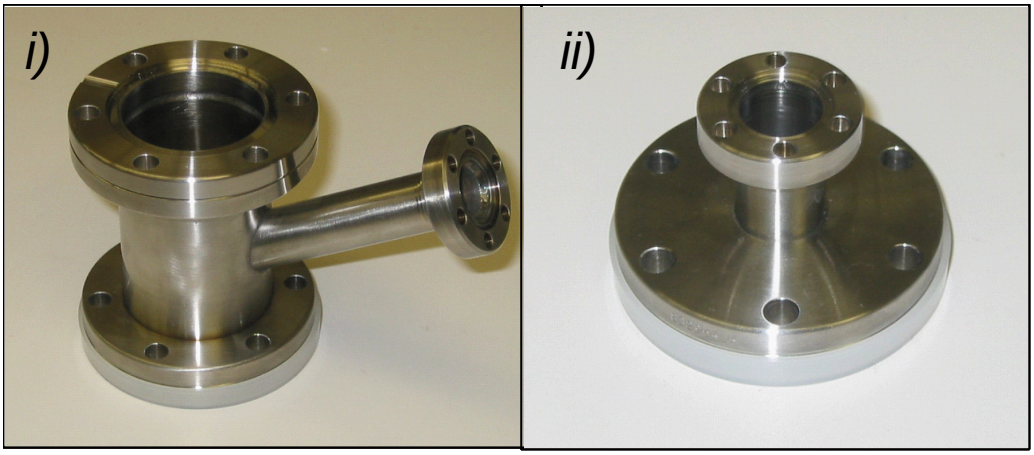

Figure 5.6: Custom flanges. i) Custom designed cluster flange. The additional port has a 1.33" flange (0.5" bore) for the rotary feedthrough and is mounted at an inclination of 30° with respect to the bottom flange. The main tubing has 2.75" flanges (1.5" bore). See Figure A.1 for blueprints. ii) Custom designed reducer flange which reduces a 2.75" flange to a 1.33" flange(0.5" bore). See Figure A.2 for blueprints.

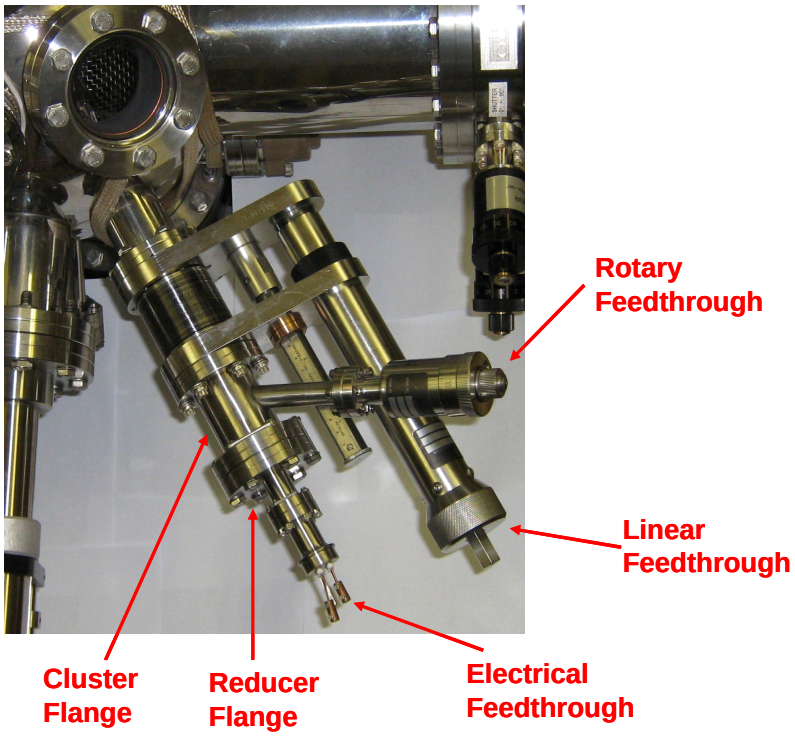

Figure 5.7: Knudsen cell mounted on preparation chamber.

joint did not provide a smooth enough transfer of motion. This caused the shutter assembly to become jammed during opening/closing. The spring provides a good transfer of motion. Opening and closing of the shutter assembly can be monitored through the windows of the preparation chamber.

Source to sample distance is adjusted using a bellows style single axis compact z stage linear feedthrough (model $LTM-154$) purchased from MDC Vacuum Products. The linear feedthrough has a 1.5" bore, 4" linear travel capability, and an operating temperature as high as 503 K. When fully retracted, the 4" linear travel prevents the K-cell from interfering with other equipment in the preparation chamber. The feedthrough is bolted onto the 2.75" flange on the preparation chamber as shown in Figure 5.7.

The K-cell meets all of its design requirements. Reproducible and stable temperatures were achieved in the range $384-410$ K, as will be shown in section 6.2. Lower or higher temperature in the range $300-425$ K may easily be achieved by an appropriate choice of heater currents. Deposition rates < 0.2 Å/ s were obtained for both L-cysteine and L-methionine, as will also be discussed in section 6.2. The aperture in the Knudsen oven can be changed allowing variation in aperture diameter A_0. The source-sample distance L is variable over the range $15-115$ mm, which covers the required $15-100$ mm range. The support rod/collars adequately hold the Knudsen oven in place (see Appendix C). The shutter provides a means of stopping a deposition as well as reducing contamination of surrounding equipment. Throughout experimentation, the K-cell was disassembled, cleaned, and then reassembled with very few problems. A bakeout (383 K for $24 hours$) was also performed with the K-cell installed in the chamber. After the bakeout a pressure of 6.0 x 10^{-10} torr was achieved. This means that the materials/components for the K-cell are all adequate for UHV.

5.3 Future Refinements

As will be shown in Chapter 6, the K-cell is fully functional for controlled deposition of an amino acid such as L-methionine, and meets the design requirements of Section 5.1. However there are several modifications and additions to the K-cell that could significantly improve performance and ease of use.

Heating/stabilization times for the K-cell were quite long. Initial temperature stabilization takes up to 300 min (see section 6.2). Subsequent stabilization takes in the neighbourhood of 100 min. A much shorter stabilization time is required in order for deposition and STM experiments to be performed on the sample during the course of the day. The long stabilization times also result in unwanted contamination of the chamber. These times for stabilization (especially the initial) would decrease if the heater wire was in direct contact with the Knudsen oven since conductive, as well as radiative, heating would occur. This was our initial design, and was tried with Cu70Ni30 ceramic coated wire that was donated by Detakta. However, the ceramic coating had a tendency to flake off the wire. This created a problematic path of conduction between the wire and Knudsen oven. Although we were not able to obtain any for this project, heater wire with a more robust insulating layer than that initially used would allow direct contact with the Knudsen oven. This would increase the rate of heat transfer and as a result speed up the heating process and decrease stabilization time.

As will be shown in section 6.4, contamination by outgassing from the K-cell is evident. Fewer contaminants would be able to reach the sample if a cylindrical tantalum shield with cover and aperture was placed around the Knudsen oven. This shield would also act as a radiation shield to improve temperature stability and decrease the stabilization time.

In order to further improve temperature stability, decrease stabilization time, and make it easier to select the desired temperature, a proportional integral derivative (PID) controller would be very helpful. PID controllers can be purchased commercially and the addition of PID control to the K-cell would be a relatively simple

modification.

A modification that would reduce the need for K-cell maintenance would be the elimination of the ceramic beads on the copper wire that connects the heater wire to the electrical feedthrough. Continuity tests before K-cell installation on the preparation chamber rarely fail. However when failure occurs, it is almost always due to the slipping of a ceramic bead leaving a small portion of copper wire exposed. No matter how densely the beads are placed on the copper wire, experience has shown that small portions of the copper wire are still exposed over time leaving a possible path of electrical conduction. A solution to this problem would be the use of fiberglass sleeving as insulation on the heater wires. Fiberglass sleeving could also be used to insulate the BeCu barrel connectors, which would further reduce the risk of unwanted short circuits.

Chapter 6

Sublimation of L-Cysteine and L-Methionine

A series of experiments were performed to evaluate the performance of the K-cell, and to characterize the effusion products during sublimation of L-cysteine and L-methionine. This chapter starts out with an outline of the experimental procedures. A discussion of the K-cell temperature as a function of time as well as temperature range, reproducibility and stability. Deposition rates were obtained for L-cysteine and L-methionine. The chapter ends with the results of the mass spectrometry and heat of sublimation measurements for L-cysteine and L-methionine.

6.1 Experimental Procedure

L-cysteine (99.6% purity) was purchased from MP Biomedicals Inc and L-methionine (99% purity) was purchased from Alpha Aesar. Prior to a series of experiments, the chamber was vented, and the K-cell removed and loaded with the amino acid of interest. When switching from one amino acid to another, the Knudsen oven was disassembled and cleaned. Cleaning involved submerging the components of the Knudsen oven in isopropyl alcohol and placing in an ultra-sonic bath. The main Knudsen oven chamber was placed in the ultrasonic bath for 45 min. The inside of the chamber was then scrubbed with a Kim wipe and placed in the ultra-sonic bath for another 30 min. Other components were placed in the ultra-sonic bath for 15 min. The Knudsen oven was then loaded with the new amino acid and assembled. All loading and assembly was done using gloves and clean tools. After assembly, the alignment of the Knudsen oven was checked (by eye) to make sure that the aperture was on the flange centerline. Prior to installation of the K-cell to the

preparation chamber, continuity tests were performed on the K-cell. A continuity test consisted of placing an electrical lead of a digital voltmeter on one of the power inputs of the electrical feedthrough. The other electrical lead was then attached to the Knudsen oven or the linear feedthrough. If the digital voltmeter read an open circuit, the continuity test was passed. After installation of the Knudsen cell on the preparation chamber, the continuity test with the linear feedthrough was always performed again.

The preparation chamber was then pumped down overnight. Pumpdown typically achieved a pressure of 5.0 x 10^{-9} torr. The K-cell had to be removed from the vacuum frequently during the experiments. Since a pressure in the 10^{-9} torr range was sufficient for these experiments, the chamber was not baked out. After the initial pumpdown, the K-cell was heated to 383 K for the purpose of degassing atmospheric contaminants such as H_2O. The K-cell was then allowed to cool back to room temperature. Experiments followed.

6.2 Knudsen Cell Temperature

In order to study temperature dependence, the K-cell was heated by setting the current to a fixed value and measuring temperature as a function of time until a stable temperature was reached. Figure 6.1 shows results for heater currents of 1.60 A and 2.00 A. Each of the data trends are fitted with an exponential of the form

$$T(t) = y_0 + A_0.e^{-\frac{t}{\tau}} \tag{6.1}$$

where $T(t)$ is the temperature of the K-cell, t is the time and y_0, A_0, and τ are adjustable parameters. The data was fitted using Origin Pro v7.5 [84] [85] [86] [87]. Table 6.1 shows the values of each fitting parameter for both fits. As can be seen in Figure 6.1, the stabilization times for the K-cell are quite long. This is likely due to the radiative heating (wire not touching oven) and relatively large mass of the oven.

Table 6.1: Temperature-time dependence fitting parameters

Parameter	**1.60** A	**2.00** A
y_0	387.3 ± 0.4	412.9 ± 0.3
A_0	-84.1 ± 0.5	-115.2 ± 0.4
τ	84.6 ± 1.5	74.7 ± 0.8

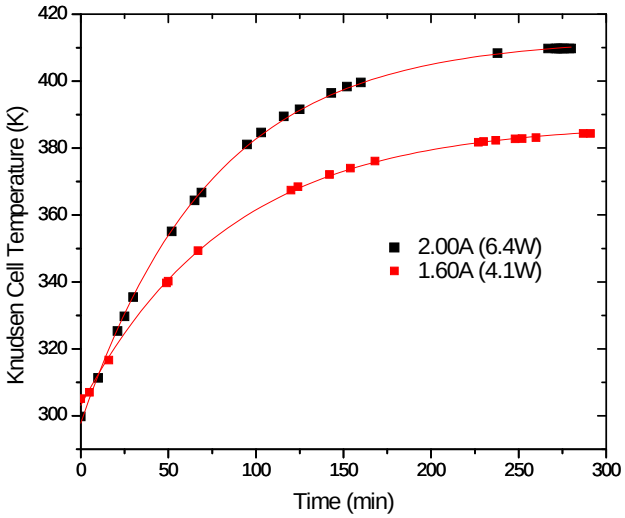

Figure 6.1: Knudsen cell temperature as a function of time for different heater currents.

Table 6.2 shows the stabilized Knudsen cell temperature for various heater currents. For the 2.00 A current, the temperature was allowed to stabilize for 275 − 300 min. Stabilized temperatures for lower currents were obtained by decreasing the current to the desired value, and letting the temperature stabilize for 100 min. Temperatures from 384 K − 410 K can be obtained using heater currents of 1.60 A − 2.00 A. The temperature can easily be controlled in this range or for lower or higher temperatures by choosing an appropriate heater current. The maximum heater current tried during these experiments was 4.50 A resulting in a K-cell temperature of 426 K after 55 min. Therefore by choosing an appropriate current less than 4.50 A, the K-cell temperature can be controlled over the required temperature range of 300 K − 425 K.

Table 6.2: Stabilization temperatures of Knudsen cell. The temperatures are averaged over six runs, and the uncertainties are calculated by subtracting the smallest value from the biggest and dividing by two. The resistance of the heating circuit is 1.6Ω

Heating Current (A)	**Heating Power** (W)	**Stabilized Temperature** (K)
2.00	6.4	410.2 ± 0.3
1.90	5.8	406.7 ± 0.4
1.80	5.2	401.2 ± 0.5
1.70	4.6	395.6 ± 0.2
1.60	4.1	384.3 ± 0.2

As shown in Table 6.2, the temperature for a given current is reproducible to within ±0.5 K as required. The temperatures reported in Table 6.2 were found to be stable within ±0.5 K over a measured period of $5 - 10$ min, also meeting design requirements.

6.3 Deposition Rate

Figure 6.2 displays the K-cell deposition rate as a function of temperature for L-cysteine and L-methionine. For data collection, the current was set, then the K-cell temperature and deposition rate was recorded at intervals of $1-3$ min during heating. It should be noted that the data in Figure 6.2 were taken while the temperature was increasing, so the system was not yet in equilibrium. As shown in Figure 6.2, there is a strong increase of deposition rate with temperature, as expected, since deposition rate depends on pressure which is proportional to $\exp\left(-\frac{H_\nu}{RT}\right)$ from equation 2.43. The onset temperature of sublimation is seen to be slightly higher for L-methionine than for L-cysteine.

Tables 6.3 and 6.4 show the deposition rates that were achieved for various heater currents for L-cysteine and L-methionine respectively, using a 1 mm diameter aperture and with $L = 15$ mm. For each of these experiments, the temperature was

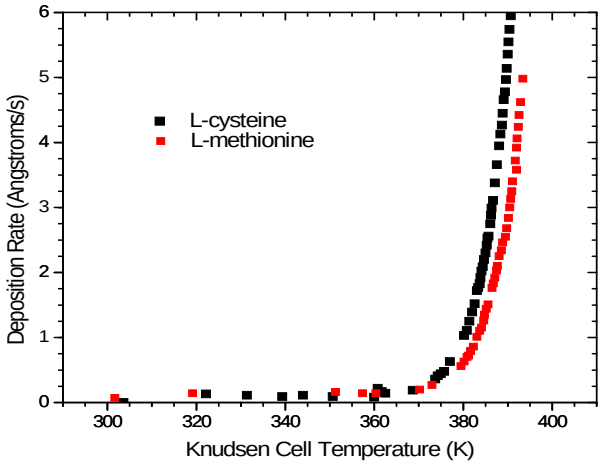

Figure 6.2: Knudsen cell deposition rate as a function of temperature. For both trends, the K-cell has a 2 mm aperture and a heating current of 2.60 A. L was set to 15 ± 2 mm.

allowed to stabilize before measurements were recorded (procedure and data collection as outlined in section 6.5). Removal of mica insulation from under the heater wires and reassembly between the L-cysteine and L-methionine experiments resulted in improved temperature stability, as is evident in Tables 6.3 and 6.4. For L-cysteine, the deposition rates are much higher than for L-methionine at similar temperatures. This can be expected given that L-methionine has a higher decomposition temperature (see Appendix D) and Figure 6.2 shows that the onset of sublimation is at a higher temperature for L-methionine.

The deposition rates of $\lesssim 0.2$ Å/ s specified in the design requirements (section 5.1) are easily achievable as can be seen from Tables 6.3 and 6.4. If even lower deposition rates are needed, they can be achieved by using either lower heater currents or by increasing the source-sample distance L. For example, according to equation 2.26 increasing L from 15 mm to 20 mm would cut the deposition rate in half.

Table 6.3: Deposition rates for L-cysteine for a 1mm diameter aperture and L=15mm. The deposition rates were averaged over five runs. The largest and smallest values were removed from each data set prior to averaging.

Current (A)	**Temperature** (K)	**Deposition Rate** (Å/s)
2.00	411.9 ± 2.3	2.52 ± 0.23
1.80	404.3 ± 1.0	1.05 ± 0.02
1.60	390.8 ± 1.0	0.23 ± 0.05
1.40	380.6 ± 1.4	0.08 ± 0.01

Table 6.4: Deposition rates for L-methionine for a 1mm diameter aperture and L=15mm. The deposition rates were averaged over seven runs. The largest and smallest values were removed from each data set prior to averaging.

Current (A)	**Temperature** (K)	**Deposition Rate** (Å/s)
2.00	410.2 ± 0.3	0.53 ± 0.08
1.90	406.7 ± 0.4	0.37 ± 0.07
1.80	401.2 ± 0.5	0.20 ± 0.04
1.70	395.6 ± 0.2	0.10 ± 0.01

6.4 Mass Spectrometry

Mass spectrometry was performed in order to determine whether or not there was any contamination and/or decomposition of the amino acids effusing from the K-cell. Mass spectrometry is a valuable tool in the identification and characterization of small quantities of amino acids [88]. Experiments were performed using a HAL 301 RIC PIC-RGA electron impact (EI) quadrupole mass spectrometer from Hiden Analytical Ltd. The acquired spectra were compared to previous EI mass spectrometry results, and to results from chemical ionization (CI) mass spectrometry and secondary ion mass spectrometry (SIMS).

Before the first experiment, the K-cell was cleaned, loaded, installed, pumped down, and degassed as described in section 6.1. The pressure in the chamber was 3.8 x 10^{-9} torr after degassing. During an experiment, the pressure would reach 1.7 x 10^{-8} torr at the most.

The filaments of the mass spectrometer were each degassed for 15 min before any data was acquired, in order to remove any contamination from previous runs. The impact energy was set to 70 eV. All EI mass spectrometry scans consisted of five iterations. The iterations were averaged to produce a single spectrum. A K-cell aperture 1 mm in diameter was used for both mass spectrometry studies.

6.4.1 L-Cysteine

A background spectrum was obtained just before heating the K-cell. The K-cell was then heated to 403 K by setting the current to 2.00 A and leaving it to heat for 200 min. Spectra were then obtained with the shutter closed, and 3 min after opening the shutter. These spectra are shown in Figure 6.3.

In an unbaked UHV chamber, the main residual gases present are H_2, H_2O, CO_2, and CO. N_2 and O_2 would be present if there was a leak in the UHV chamber. Figure 6.3(i) is a spectrum with the K-cell at room temperature. It is dominated by the gases expected in an unbaked UHV chamber. Peaks at $m/z = 16$ -17 indicate the presence of CH_4 and NH_3. There is also H_2S ($m/z = 32 - 34$) in the chamber.

In addition to these, decomposition products of L-cysteine, larger fragments, such as those at $m/z = 74$, 75, and 76 are also present.

When the K-cell was heated but the shutter remained closed , all peaks increased in intensity as shown in Figure 6.3(ii). Even though the closed shutter prevents line of sight effusion into the mass spectrometer, it does not seal the K-cell, and effusion products are still entering the chamber. The greatest relative increase in intensity upon heating the K-cell was in H_2S. This could be due to decomposition of L-cysteine when heated in the K-cell or to decomposition of L-cysteine adsorbed on the outside of the K-cell. The peak at $m/z = 17$ also increases relative to $m/z = 18$. This means NH_3 is increasing relative to H_2O.

When opening the shutter (see Figure 6.3(iii)), the most significant increases occur in H_2S ($m/z = 32$ to 34) and in L-cysteine fragments ($m/z = 59$ and $74-76$). The large H_2S peak and its further increase suggests that decomposition of L-cysteine is occurring in the K-cell. Further increases in the background peaks at $m/z \leq 50$ could be due to degassing from the front of the K-cell exposed by the open shutter, and to decomposition of L-cysteine, as well as to a small temperature increase between 6.3(ii) and (iii). An increase in peaks $m/z \geq 50$ is present after opening the shutter (note that not all are visible in Figure 6.3). This is evidence that effusion of L-cysteine is taking place.

Figure 6.4 shows the mass spectrum from Figure 6.3(iii) scaled for comparison with results compiled by the National Institute of Standards and Technology (NIST) [89]. The spectra were scaled so that the intensities of the peaks at $m/z = 76$ were the same. The NIST spectrum was obtained by EI mass spectrometry at 70 eV, and shows the relative intensities of fragments detected by the mass spectrometer after electron impact ionization of L-cysteine.

The spectra are in relatively good agreement for $m/z > 50$, although there are some differences in relative intensity. For $m/z < 50$, our spectrum is dominated by background gases such as H_2O, CO_2, and CO. The very large H_2S peak in our spectrum is an indication of L-cysteine decomposition.

The high intensity of background peaks and some differences in relative intensity

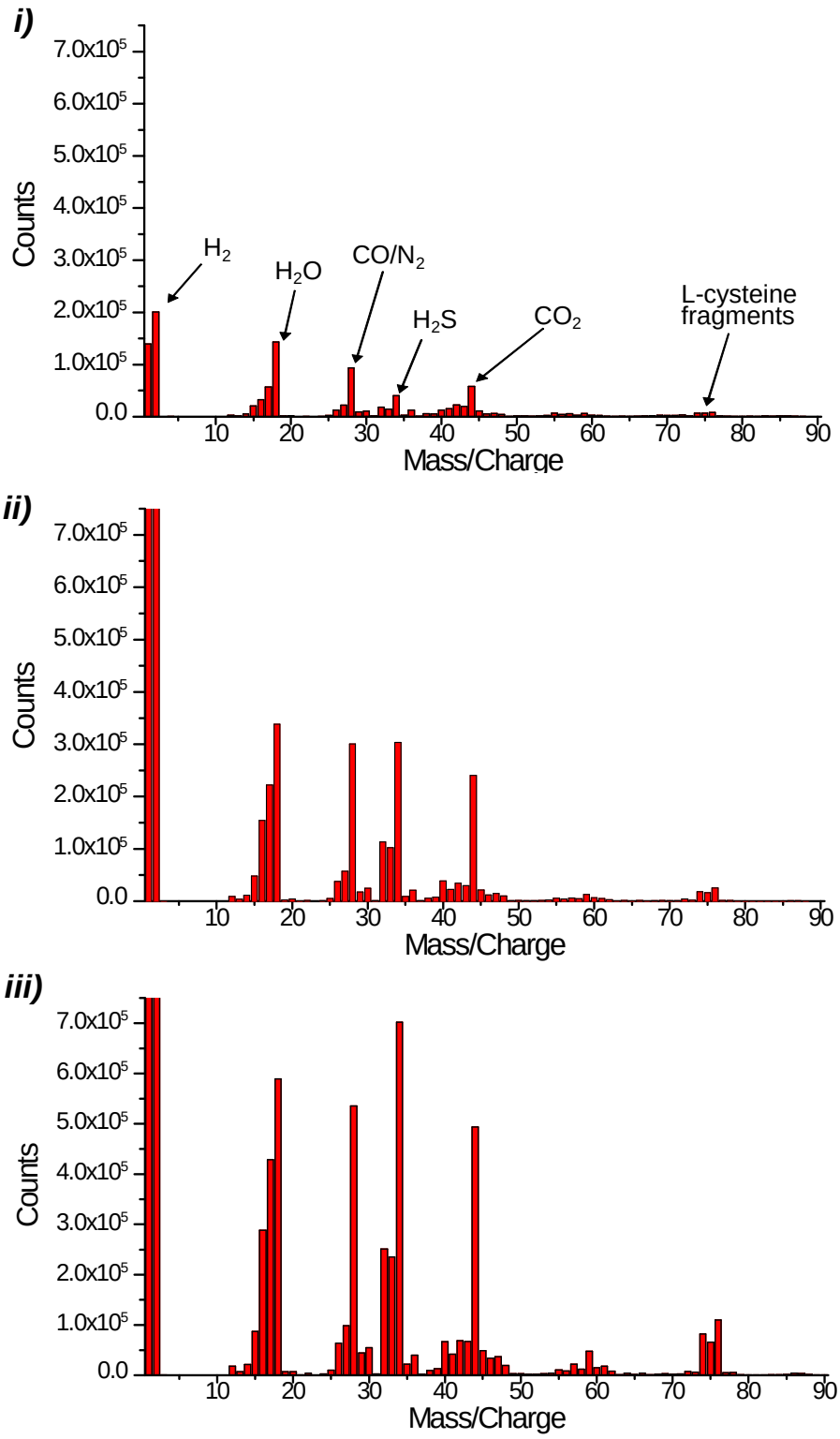

Figure 6.3: L-cysteine mass spectra. *i)* Unheated K-cell (background) *ii)* Heated K-cell with shutter closed *iii)* Heated K-cell with shutter opened. Heated to 403 K. The labels on selected peaks represent the parent molecules.

may be attributed to the unfavourable geometry of our experiment. The mass spectrometer was positioned on the UHV preparation chamber for other experiments, and unfortunately it is just catching the edge of effusion from the K-cell (see Figure 3.9). Effusion products are thus entering the mass spectrometer aperture at a shallow angle.

Although the reported decomposition temperature of L-cysteine (448 K) is almost 50 K greater than our experimental temperature [83], unexpected L-cysteine decomposition has been reported in past studies. Junk *et al.* were unable to acquire unique reproducible mass spectra of cystine (two L-cysteine molecules joined by a disulfide bond); they concluded that their observations were due to decomposition products [90]. Sabbah *et al.* were unable to obtain heat of sublimation measurements for L-cysteine, which was attributed to L-cysteine decomposition at < 448 K in vacuum. Prince *et al.* attempted K-cell effusion of L-cysteine for gas phase photoemission using both stainless steel and aluminum crucibles; they found that their mass spectrum was dominated by H_2S [91].

In order to identify the peaks in our mass spectra, our L-cysteine results were compared to previous electron impact mass spectrometry studies performed by Biemann *et al.* [92], and chemical ionization (CI) mass spectrometry performed by Milne *et al.* [93]. CI mass spectrometry does not use high energy electron bombardment to generate ions. Rather it involves the transfer of a proton, electron, or other charged species between reactants to generate ions. Milne *et al.* used methane as the reactant gas for their studies of amino acids. Because of the different ionization techniques, the relative intensities of fragments can be quite different in EI and CI mass spectrometry, but many of the same peaks are observed. Neither Biemann *et al.* nor Milne *et al.* reported decomposition, but Biemann *et al.* used more stable amino acid derivatives (ethyl esters) for their study, and Milne *et al*. claimed that the addition of a proton in their CI mass spectrometry stabilized the L-cysteine molecule.

A summary of the main peaks that we observed, along with the previous studies which found the same peaks is shown in Table 6.5. The molar mass of L-cysteine

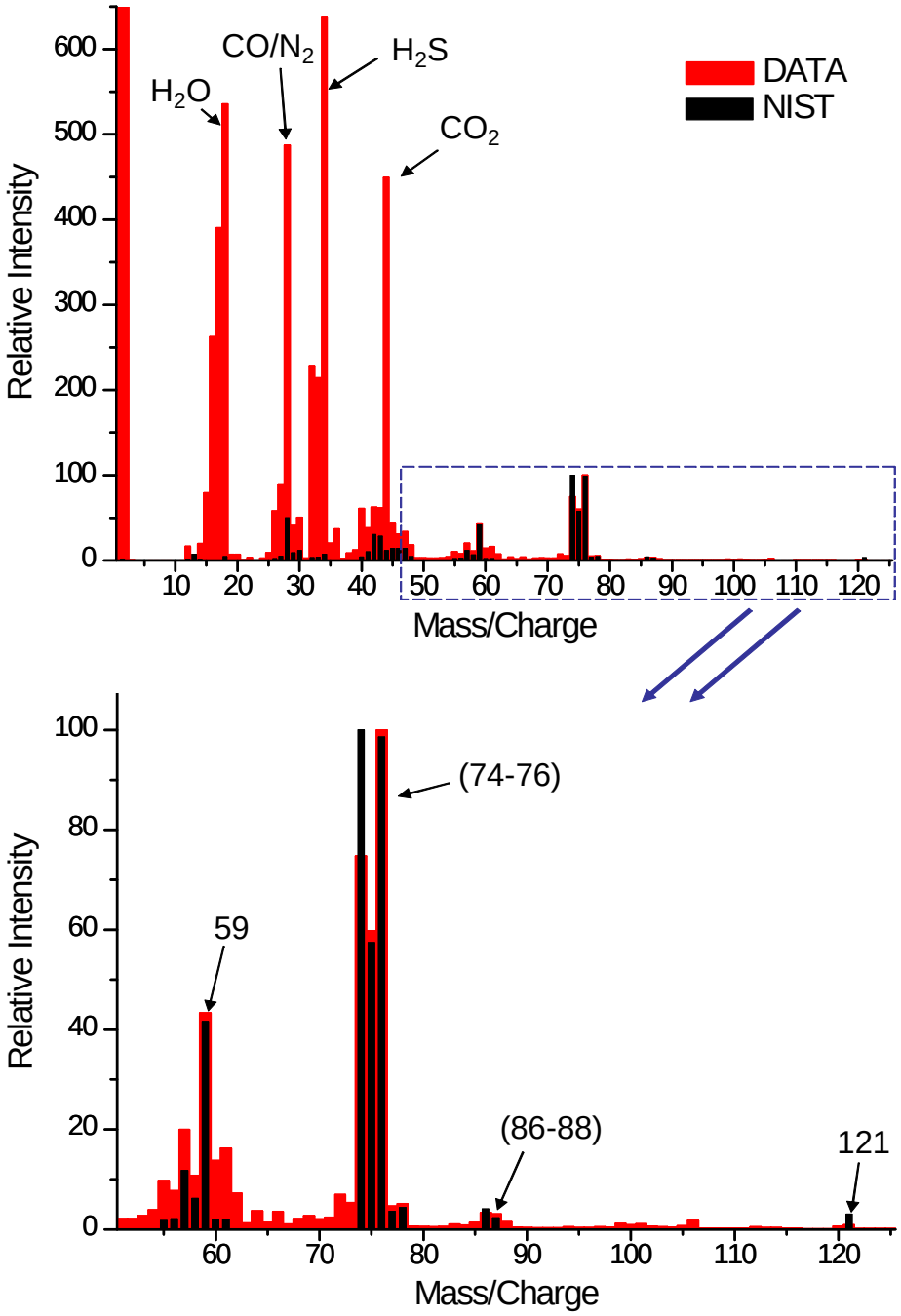

Figure 6.4: Comparison of measured L-cysteine mass spectrum with NIST spectrum. The blue rectangle indicates the area of the top spectrum that has been zoomed (displayed on the bottom). Both spectra used an impact energy of 70 eV. The labels on selected peaks represent the parent molecules.

Table 6.5: L-cysteine mass spectrometry peaks

m/z	**Peak/Fragmentation**	**Observer(s)**
121	Parent Ion P	EI [89], CI [93], SIMS [94],
88	$P - H_2S$	CI [93], SIMS [94]
87	$P - NH_3 - OH$	EI [89], SIMS [94]
86	$P - NH_3 - H_2O$	EI [89], SIMS [94]
76	$P - COOH$	EI [89], CI[93], SIMS [94]
75	$P - COOH_2$	EI [89], CI [93]
74	$P - CH_2S$	EI [89], CI[93], SIMS [94]
59	$(P - COOH) - NH_3$	EI [89], CI [93], SIMS [94]

is $121amu$. The parent ion P ($m/z = 121$) is visible. The expulsion of H_2S ($m/z = 34$) from the parent ion yields a peak at $m/z = 88$. This was not observed in the NIST data or by Biemann *et al.*, but it was seen by Milne *et al.* and Leggett *et al.* It is clear in this work. A loss of ammonia (NH_3) and OH results in a peak at $m/z = 87$ [89]. Losses of both NH_3 and H_2O yield a peak at $m/z = 86$ [89]. These peaks are seen in the NIST data. The $m/z = 76$ fragment corresponds to a loss of $COOH$. Further fragmentation (loss of NH_3) of this ion produces a peak at $m/z = 59$ [89]. Both peaks were observed by Biemann *et al.* [92]. A peak at $m/z = 74$ corresponds to a loss of CH_2S [89] [92]. The loss of $COOH_2$ results in the $m/z = 75$ peak [89] [93].

Leggett *et al.* performed SIMS mass spectrometry on L-cysteine [94]. In their SIMS experiment, crystalline L-cysteine was bombarded with Cs^+ or O_2^+ ions. L-cysteine molecules and fragments removed by this bombardment were then detected. With the exception of the $P - COOH_2$ ($m/z = 75$) peak, Leggett *et al.* observed all the peaks that are listed in Table 6.5.

6.4.2 L-Methionine

The same method for mass spectrometry data collection was used for L-methionine as for L-cysteine. Figure 6.5(i) shows a spectrum of the K-cell at room temperature before heating. As in Figure 6.3(i), the spectrum is dominated by background gases expected in an unbaked UHV chamber. Note that the y-axis scale is only half that of Figure 6.3(i) and the intensities of the H_2, H_2O, and CO_2 peaks are lower, indicating a cleaner UHV chamber for this experiment. There is also much less H_2S ($m/z = 32 - 34$). Only a very small number of L-methionine fragments are visible at $m/z > 50$.

Figure 6.5(ii) shows the spectrum obtained with the K-cell heated to 403 K and the shutter closed. The most significant increases are in the levels of H_2 and H_2O, likely due to the desorption of atmospheric contaminants from the Knudsen oven. There is no significant increase in $m/z \geq 50$ when heating the K-cell with the shutter closed, and only a very small increase in H_2S.

The spectrum with the shutter open shows an increase in L-methionine fragments at $m/z \geq 50$ (note that not all are visible in Figure 6.5(iii)). Unlike the L-cysteine spectra, there is only a very subtle increase in peaks at $m/z \leq 50$, such as H_2S. Together this implies that there is L-methionine effusing from the K-cell and that no significant decomposition is occurring in the heating process.

Figure 6.6 shows our mass spectrum of L-methionine scaled to that from the NIST database [89]. Like our mass spectrum, the NIST spectrum was obtained by EI mass spectrometry at an impact energy of 70 eV. The spectra were scaled so that the intensities of the peak at $m/z = 61$ were the same. The intensity of our L-methionine peaks is very low compared to the background gases, indicating that only a small amount of L-methionine is reaching the mass spectrometer. This is due to the unfavourable geometry and to the relatively low effusion rates of L-methionine at the temperatures used. For $m/z > 50$, the spectra agree relatively well, although the relative intensities of the different fragments (particularly at $m/z > 100$) are not the same. Our intensities for the high m/z fragments are lower than expected. We also

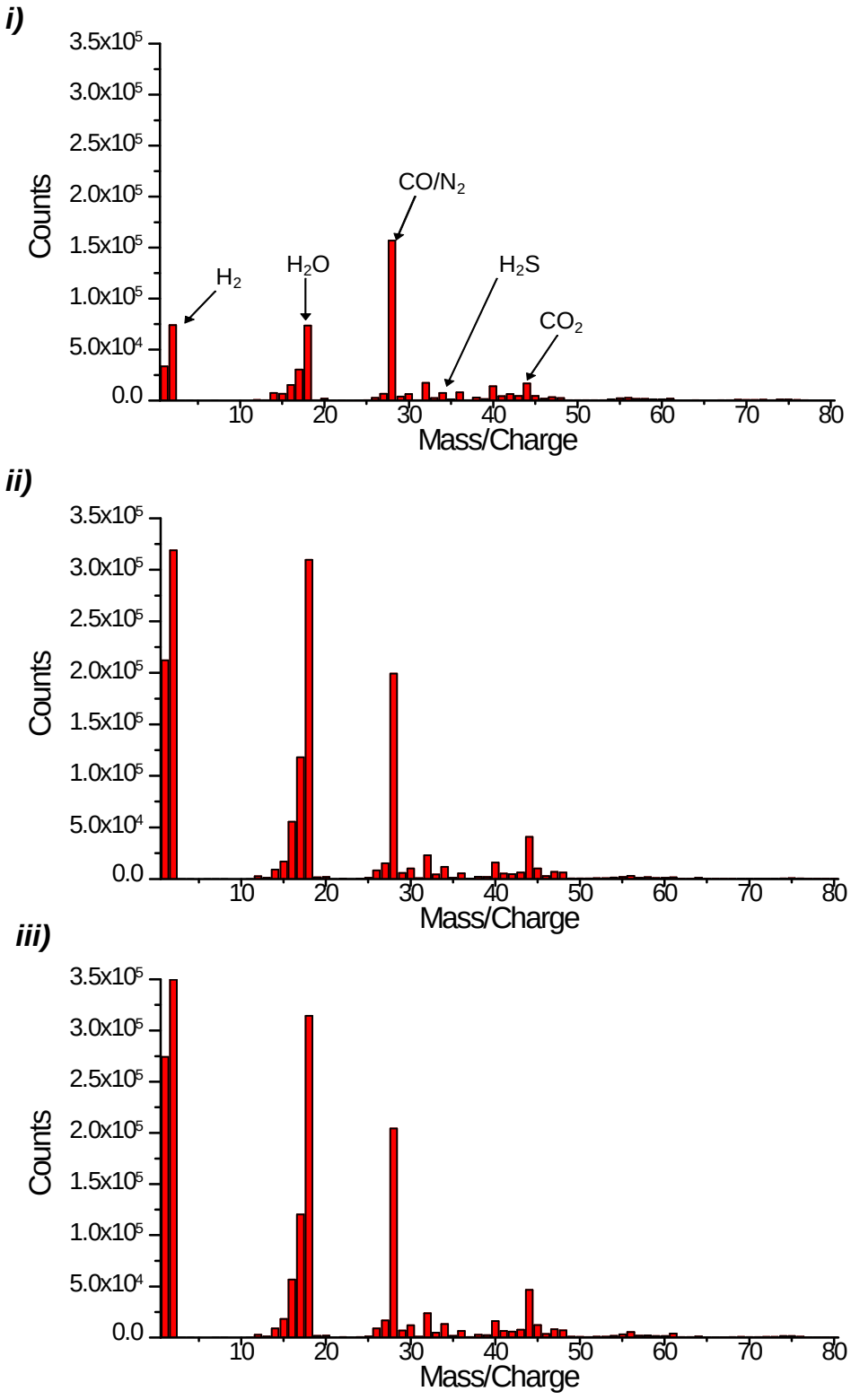

Figure 6.5: L-methionine mass spectra. *i)* Unheated K-cell *ii)* Heated K-cell with shutter closed *iii)* Heated K-cell with shutter opened. The K-cell was heated to 403 K. The labels on selected peaks represent the parent molecules.

see a high intensity at $m/z = 130$ and 148 rather than 131 and 149. These differences in intensity may be due to different conditions inside our mass spectrometer ionizing chamber (relative high pressure of background gases compared to the low pressure of L-methionine) compared to previous studies.

In order to identify the peaks in Figure 6.5, our results were compared to those from EI mass spectrometry studies performed by Junk *et al.* and Biemann *et al.,* and CI mass spectrometry studies performed by Milne *et al.* [92] [90] [93]. The molar mass of L-methionine is $149amu$. A peak at $m/z = 148$ is clearly visible. The difference in m/z from the molar mass of L- methionine would be due to a loss of hydrogen. A very faint peak at $m/z = 149$ is also present. A loss of H_2O from the parent ion P results in a peak at $m/z = 131$. It is worth mentioning that our work also has a visible peak at $m/z = 130$. This could be due to the loss of an additional hydrogen from the $P - H_2O$ ion. The $P - H_2O$ ion fragments to produce $C_4H_6NO_2$ at $m/z = 83$ and CH_3SH at $m/z = 48$ [90]. These peaks are not present in the NIST spectrum but were seen by Junk *et. al.* and are found in our data. The $m/z = 104$ peak is the result of a loss of the carboxyl ($COOH$) group from the parent ion [90]. The ion $P - COOH$ ion at $m/z = 104$ can lose CH_3SH which leaves an intense peak at $m/z = 56$ [92]. This same fragmentation pattern was also found in CI mass spectrometry studies performed by Milne *et al.* [93]. The observed peaks at $m/z = 74$ and $m/z = 75$ correspond to CH_3SCH_2CH and $CH_3SCH_2CH_2$ fragments respectively [89] [90] [92] . An intense peak at $m/z = 61$ represents CH_3SCH_2 [89] [90] [92]. A summary of the observed peaks is shown in Table 6.6. These results appear to be in good agreement with previous EI mass spectrometry results performed by Biemann *et al.* and Junk *et al.*

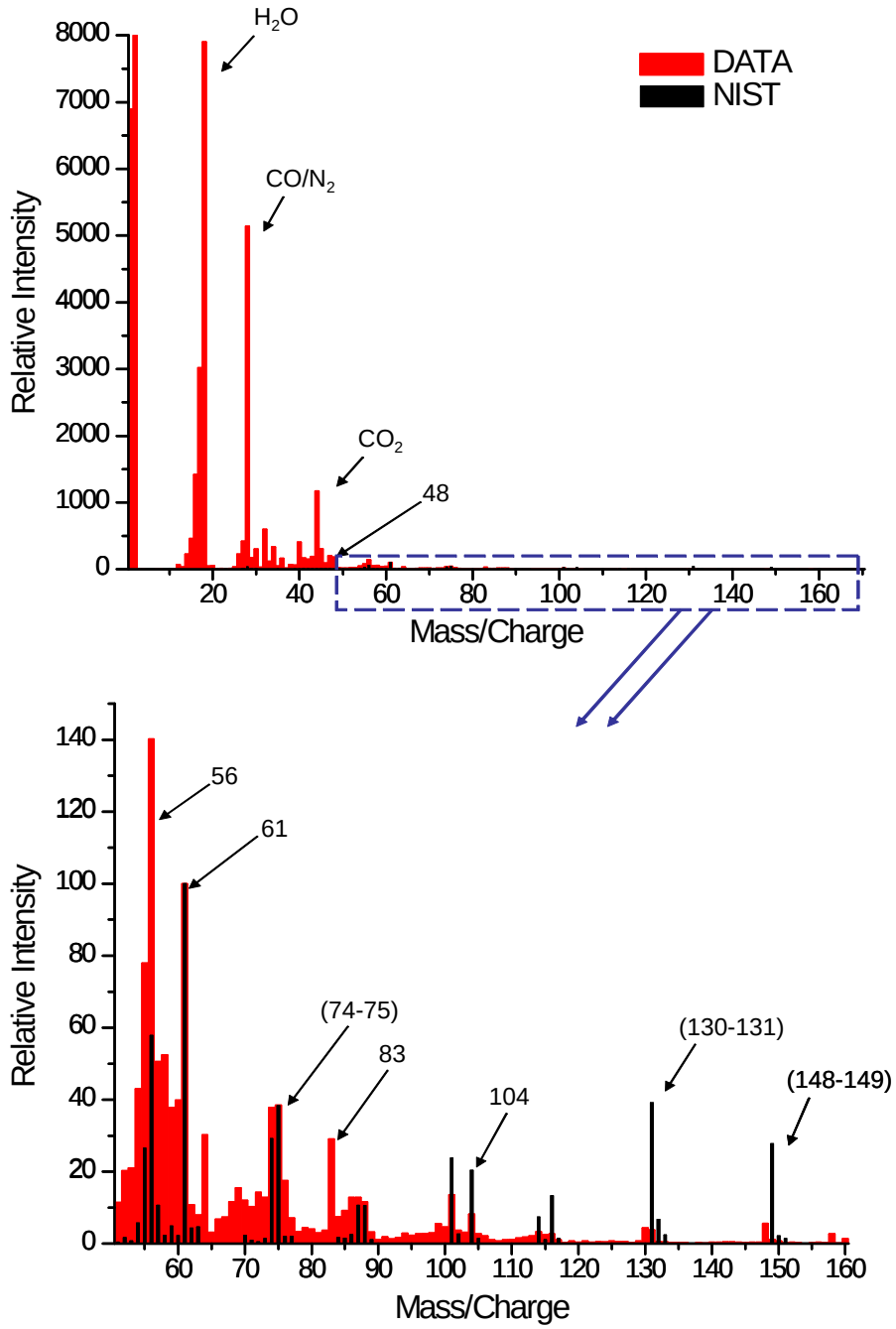

Figure 6.6: Comparison of measured L-methionine mass spectrum with NIST spectrum. The blue rectangle indicates the area of the top spectrum that has been zoomed (displayed on the bottom). Both spectra used an impact energy of 70 eV. The labels on selected peaks represent the parent molecules.

Table 6.6: L-Methionine mass spectrometry peaks

m/z	**Peak/Fragmentation**	**Observer(s)**
149	Parent Ion P	EI [89] [90]
148	$P - H$	EI [92]
131	$P - H_2O$	EI [89] [90]
104	$P - COOH$	EI [89] [90] [92], CI [93]
83	$P - CH_6NO_2$	EI [90]
75	$P - C_2H_4NO_2$	EI [89] [90]
74	$P - C_2H_5NO_2$	EI [89] [90] [92]
61	$P - C_3H_6NO_2$	EI [89] [90] [92]
56	$(P - COOH) - CH_3SH$	EI [89] [90] [92], CI [93]
48	CH_3SH	EI [90]

6.5 Heat of Sublimation

As discussed in section 2.4.3, effusion from a K-cell can be used together with a quartz crystal microbalance (QCM) to estimate the heat of sublimation of the material undergoing effusion. In this section, heat of sublimation measurements for L-cysteine and L-methionine will be described, and results compared to previous work.

Prior to experimentation, the K-cell was treated in the same manner (cleaned, loaded, pumped down, degassed) described in section 6.1. Chamber pressure was similar before (3.8 x 10^{-9} torr) and during (1.7 x 10^{-8} torr) experimentation as with mass spectrometry.

The experimental procedure was based on that of Hutchings *et al.* [65]. The K-cell was initially heated with a maximum current of 2.00 A. The temperature was allowed to stabilize. Upon stabilization, the temperature T and deposition rate $\frac{\partial \tau}{\partial t}$ were recorded for a period no less than 5 min. The heater current was then lowered 0.10 A or 0.20 A and the temperature allowed to stabilize. Recording

Table 6.7: Density and molecular mass for L-cysteine and L-methionine

Amino Acid	**Density** ($\mathrm{kg/m^3}$)	**Molecular Mass** (kg)
L-cysteine	1756 [95]	2.01 x 10^{-25}
L-methionine	1220 [96]	2.48 x 10^{-25}

of data proceeded. Initial stabilization time(s) took $300 - 600$ min. Subsequent stabilization time(s) took in the neighbourhood of 100 min. A single deposition experiment consisted of four (sometimes 3) data points [65]. Twelve deposition runs were performed for L-cysteine and seven for L-methionine. The minimum current used was 1.50 A. For all depositions, the K-cell had a 1 mm diameter aperture. The source-sample distance was set to $L = 15$ mm for all experiments except for three L-cysteine cysteine experiments at $L = 75$ mm and 85 mm.

The data analysis follows the theory described in Section 2.4.3. Specifically equations 2.51 and 2.52 were used to calculate the pressure p inside the K-cell, with $L = 15$ mm and

$$A_0 = \pi \left(\frac{d}{2}\right)^2 \tag{6.2}$$

where $d = 1$ mm. A plot of $ln(p)$ vs. $\frac{1}{T}$ was made for each deposition run, and yielded a straight line as expected. The error bars were calculated using equation 2.55, with $\delta T = 0.1$ K, and $\delta(\frac{\partial \tau}{\partial t}) = 0.02 - 0.04$ Å/ s (the uncertainties were based on the variations in T and $\frac{\partial \tau}{\partial t}$ over the period of data collection). The slope of the line was calculated using a least squares fit (Origin v7.5) [84] [85] [86] [87]. The heat of sublimation H_ν was calculated using equations 2.57 and 2.58.

A typical plot of $ln(p)$ vs. $\frac{1}{T}$ for L-cysteine is shown in Figure 6.7. The data points lie on a straight line, as expected from the exponential dependence of p on $\frac{1}{T}$ in the Clausius-Clapeyron equation. The results for the heat of sublimation of L-cysteine are shown in Figure 6.8. Each result was obtained from a separate experiment as described above. The heat of sublimation results for L-cysteine are scattered over the range 130.7 kJ/ mol − 197.0 kJ/ mol, with an average of 168.3 ± 33.2 kJ/ mol. Gaffney *et al.* measured the heat of sublimation of amino acids using rapid heating proton

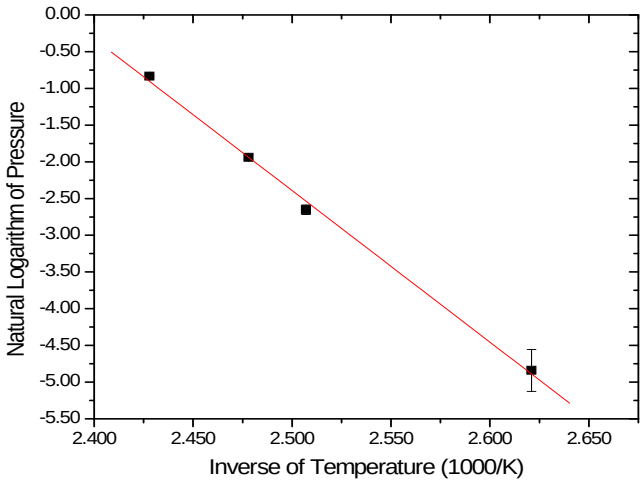

Figure 6.7: Natural logarithm of pressure as a function of inverse of temperature for L-cysteine

transfer mass spectrometry, and found a heat of sublimation of $96.2 \pm 4.2\,\mathrm{kJ/mol}$ for L-cysteine, significantly lower than our results [97]. Sabbah *et al.* were unable to determine a heat of sublimation for L-cysteine because of its low decomposition temperature (448 K) which they found decreased when L-cysteine was under vacuum [83]. Our results for L-cysteine are widely scattered, although there do appear to be groups of a few consistent results. The chamber was vented twice (see Figure 6.8) to fix thermocouple problems. There was no obvious effect on our results. In order to check the possibility that heating of the QCM by the K-cell was affecting the results, three experiments were performed with a greater L (see Figure 6.8); again no effect. Gaffney *et al.* notes that heats of sublimation depend on the environment of the molecule in the solid, and thus on sample purity and on the presence of competitive decomposition reactions [97]. Since our mass spectrometry results suggest that L-cysteine is decomposing, we cannot expect our heat of sublimation results to be reliable.

The same experimental method and data analysis were used for L-methionine deposition runs. Figure 6.9 shows a plot of $ln(p)$ vs. $\frac{1}{T}$ for L-methionine deposition,

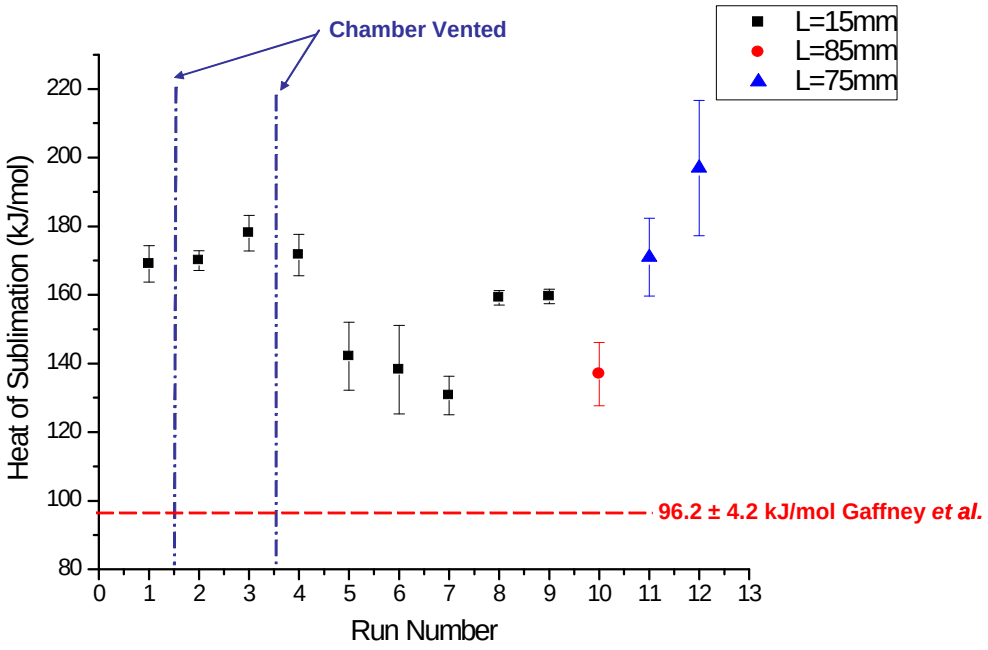

Figure 6.8: Heat of sublimation results for L-cysteine

which produces a linear graph as expected.

The heat of sublimation results for L-methionine are shown in Figure 6.10. They are scattered over the range $147.3\,\mathrm{kJ/mol} - 167.5\,\mathrm{kJ/mol}$ with an average of $156.5 \pm 10.1\,\mathrm{kJ/mol}$. These results have a much smaller scatter than those for L-cysteine. Our results for L-methionine are all higher than those reported by Gaffney *et al.* using rapid heating proton transfer mass spectrometry [97] and Svec *et al.* using effusion from an aluminum K-cell [98], but they are in agreement with those of Sabbah *et al.* who determined the heat of sublimation using an effusion cell and calorimeter [83]. The better quality results obtained for L-methionine compared to L-cysteine are consistent with the mass spectrometry results, which did not show any decomposition for L-methionine.

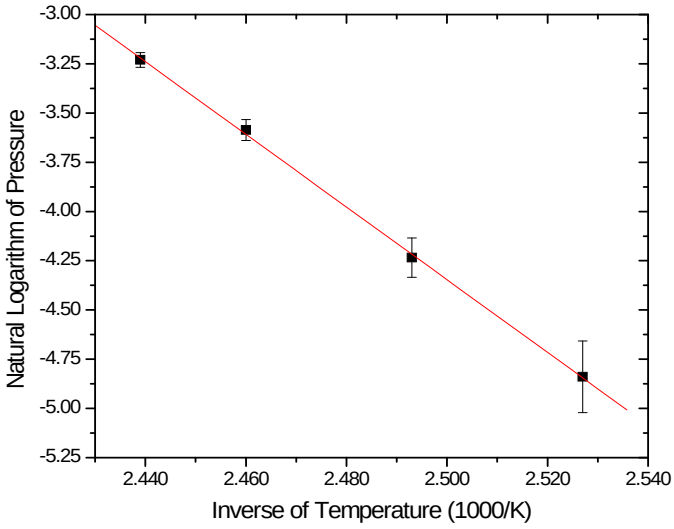

Figure 6.9: Natural logarithm of pressure as a function of inverse of temperature for L-methionine.

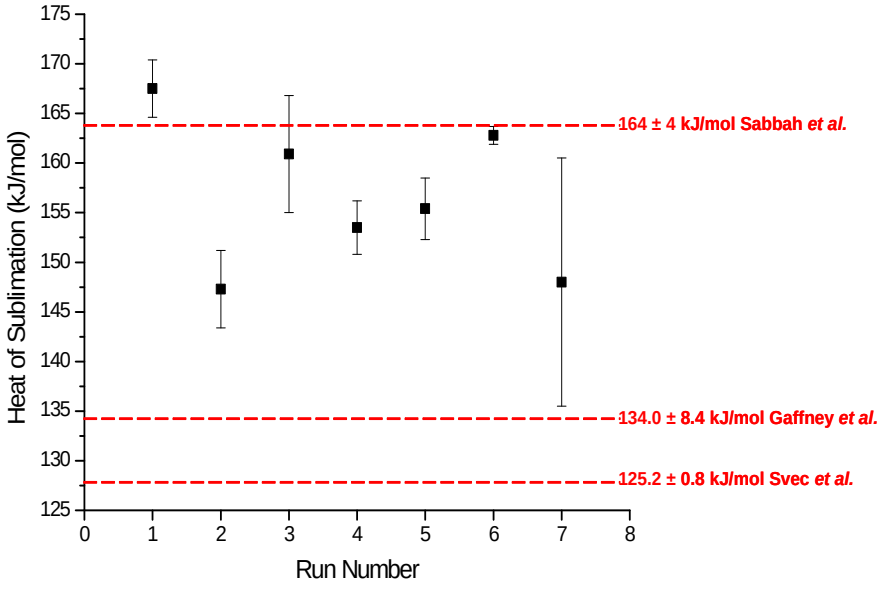

Figure 6.10: Heat of sublimation results for L-methionine

Chapter 7

Conclusion

The installation of a UHV preparation chamber, preparation and STM imaging of Au(111) substrates, and the design of a K-cell for the deposition of amino acids have been described in this thesis. The performance of the K-cell was characterized by performing mass spectrometry and heat of sublimation studies on L-cysteine and L-methionine. In this chapter, a summary of accomplishments, conclusions and suggestions for future work will be presented.

7.1 Installation of Ultra-High Vacuum Preparation Chamber

The installation and commissioning of a UHV preparation chamber designed by Dr. Katie Mitchell and built by Torrovap Industries Inc. was successful. The preparation chamber is connected to the RHK UHV STM chamber via a gate valve. The two chambers have separate pumping systems, allowing them to operate independently. The ion pump, turbo pump, transfer arm, sample head manipulator, LEED, K-cell, mass spectrometer, QCM, OCI ion gun, and gas handling line were all successfully installed on the preparation chamber. Components such as the four-way evaporator and very low energy ion source have yet to be installed. Bakeout at 383 K for 24 hours with all installed components yielded a pressure of 6.0 x 10^{-10} torr which is within UHV requirements. The preparation chamber was subsequently used for all experiments involving the K-cell, QCM, and mass spectrometer.

7.2 Preparation and Scanning Tunneling Microscopy Imaging of Au(111)

Preparation and STM imaging of Au(111) substrates were performed. The feasibility of producing our own substrates as opposed to purchasing commercial substrates was investigated. Tunneling conditions to maximize the success rate of acquiring high-resolution images were determined.

The images of the homemade Au(111) substrates (see Figure 4.3) did contain some of the triangular features typical of a Au(111) substrate. However, the surface quality was poor overall. We were unable to acquire high resolution images of "herringbone" reconstruction or individual atoms. A cross section of the surface (see Figure 4.4) shows that over a horizontal distance of approximately 4000 Å, there is a corrugation of 2000 Å. The surface lacks large the flat terraces which are required for it to be a suitable substrate for the deposition of amino acids. Thus commercial Au(111) substrates were purchased from Molecular Imaging Corp.

The STM imaging of commercial Au(111) substrates yielded images of large flat terraces as well as high resolution images of both "herringbone" reconstruction and individual atoms (see Figures 4.7 and 4.8 respectively). We found individual and paired line separations to be 43 ± 3 Å and 63 ± 3 Å respectively. This agrees with the 44 Å and 64 Å observed experimentally and with the calculated size of 63.4 Å for the (22 x $\sqrt{3}$) unit cell along [$1\bar{1}0$] [33]. We also were successful in acquiring images of individual atoms, as shown in Figure 4.8. The average spacing of the surface atoms was found to be 2.66 ± 0.11 Å. This separation is smaller than that of an ideally terminated surface, which is 2.88 Å. This can be expected due to the fact that an Au(111) surface undergoes contraction during the reconstruction process [35]. The expected hexagonal pattern of the surface atoms was slightly distorted. The distortion is partly due to drift in the piezoelectric tubes of the STM and partly a result of surface reconstruction. Due to the large flat terraces and high resolution images obtained, the commercial Au(111) substrates were deemed suitable for the

deposition of amino acids.

There were some common conditions found during scanning that increase the chance of success of acquiring high resolution Au(111) STM images. This includes always imaging in a baked chamber. The bias voltage should always be fairly low ($0.025\,\mathrm{V} - 0.050\,\mathrm{V}$) and the tunneling current in the range $0.9\,\mathrm{nA}\ -1.2\,\mathrm{nA}$. A fast scan speed of 30-50ms/line along with the maximum setting on the z position A/D gain should be used.

7.3 Design of Knudsen Cell

The primary goal of this project was the design of a K-cell for sublimation of amino acids. The K-cell met all of the design requirements outlined in section 5.1.

The K-cell produced stable and reproducible temperatures in the range from room temperature to 425 K as discussed in section 6.2. When the temperature was allowed to stabilize with a specific heater current, the temperature was always within $\pm 0.5\,\mathrm{K}$ of a previous stabilization using the same heater current (see Table 6.2). Over a period of at least 5 min, these temperatures were stable to $\pm 0.5\,\mathrm{K}$.

Reproducible deposition rates were obtained for both L-cysteine and L-methionine at $< 0.20\,\mathrm{\AA/s}$ as shown in Tables 6.3 and 6.4, and as required in order to obtain low coverage deposition. The shutter also allows the depositions to be controlled for a well-defined time. This is essential in controlling the quantity of amino acid deposited on the surface.

The in-vacuum length of the K-cell and the linear motion feedthrough allow source-sample distance L to be varied over $15 - 115\,\mathrm{mm}$. This allows L to be optimized for deposition rate and even sample coverage, and the K-cell to be retracted when not in use. The aperture can be changed easily and aperture disks have been machined with 1, 2, and 3 mm diameter apertures.

When loading the K-cell with another amino acid, assembly/disassembly, cleaning and loading can be done relatively quickly and easily, as required. The K-cell also underwent a bakeout at 383 K for 24 hours with the rest of the UHV chamber.

Although the K-cell meets its design requirements, there are several modifications and additions that could improve its performance. These are described in section 5.1 and will be summarized here. Improvements are the addition of a PID controller, tantalum heat shield, and fiberglass sleeving on the power lines and BeCu barrel connectors.

7.4 Mass Spectrometry

Mass spectrometry studies were performed in order to characterize the K-cell effusion products at a temperature of 403 K. For both L-cysteine and L-methionine, background gases such as H_2, H_2O, CO, and CO_2 dominated the spectra. This was due to lack of bakeout, unfavourable geometry, and low deposition rates.

For L-cysteine, the fragmentation (peaks and intensities) compared to NIST were in fairly good agreement (see Figure 6.4) [89]. Peaks were identified by comparison with EI, CI and SIMS (see Table 6.5) [89] [92] [93] [94]. A very large H_2S peak is an indication of L-cysteine decomposition, consistent with previous reports (see section 6.4). This emphasizes the need for care in interpreting STM and other studies of L-cysteine overlayers deposited in vacuum. A future experiment that would be interesting would be to attempt sublimation at a lower temperature or to use a less reactive oven material (glass).

The fragmentation pattern of L-methionine compared to NIST is in fairly good agreement (see Figure 6.6) [89]. The intensities are not all in agreement with NIST. This is likely due to different experimental conditions (low deposition rate, unfavourable geometry). The peaks were identified by comparison to EI and CI (see Table 6.6) [89] [90] [92] [93]. There was no evidence of decomposition of L-methionine, also consistent with other reports (see section 6.4).

In the future performing the same experiment in a baked UHV chamber would be useful in order to reduce the intensity of background gases in the spectra. Although it is not feasible in this thesis, performing the experiment with the K-cell in a direct line of site of the mass spectrometer would also be advantageous. This would mean

a greater quantity of the amino acid would enter the mass spectrometer and increase the intensity of peaks that are a direct result of K-cell effusion ($m/z > 50$).

7.5 Heat of Sublimation

The heats of sublimation for L-cysteine and L-methionine were measured using the K-cell and QCM, as described in section 6.5. For both L-cysteine and L-methionine, plots of $\ln p$ vs. $\frac{1}{T}$ were linear, as expected from the Clausius-Clapeyron equation. The heat of sublimation results for L-cysteine (see Figure 6.8) were scattered in the range $130.7 - 197.0\,\mathrm{kJ/\,mol}$ with an average of $168.3 \pm 33.2\,\mathrm{kJ/\,mol}$. Our results are all higher than the value of $96.2 \pm 4.2\,\mathrm{kJ/\,mol}$ reported by Gaffney *et al.*[97]. Given that our mass spectrometry results for L-cysteine suggest thermal decomposition, we would not expect to measure an accurate heat of sublimation, since heat of sublimation is sensitive to sample environment and purity [97] [83].

Results for the heat of sublimation for L-methionine are scattered in the range $147.3 - 167.5\,\mathrm{kJ/\,mol}$ with an average of $156.5 \pm 10.1\,\mathrm{kJ/\,mol}$. The scattering of results is lower than for L-cysteine. Our results are in best agreement with those of Sabbah *et al.* who reported a heat of sublimation of $164 \pm 4\,\mathrm{kJ/\,mol}$ [83].

Bibliography

[1] B. Kasemo. Biological surface science. *Surface Science*, 500:656–677, 2002.

[2] R.S. Phadke. Immobilization of enzymes/coenzymes for molecular electronics applications. *Biosystems*, 35(2-3):179–182, 1995.

[3] H.S. Mansur, R.L. Orefice, W.L. Vasconcelos, Z.P. Lobato, and L.J.C. Machado. Biomaterial with chemically engineered surface for protein immobilization. *J. Mater. Sci., Mater. Med. (USA)*, 16(4):333 – 40, 2005.

[4] D. Losic, K. Short, J.J. Gooding, and J.G. Shapter. Scanning probe microscopy characterization of immobilized enzyme molecules on a biosensor surface: Visualization of individual molecules. *J. Serb. Chem. Soc.*, 69(2):93–106, 2004.

[5] L.J. Blum and P.R. Coulet. *Biosensor Principles and Applications*, volume 15. Marcel Dekker Inc, 1991.

[6] L. Stryer. *Biochemistry*. W.H. Freeman & Company, fourth edition, 1999.

[7] A.P.F. Turner, I. Karube, and G.S. Wilson. *Biosensors: Fundamentals and Applications*. Oxford University Press, 1987.

[8] G.P. Bates. One misfolded protein allows others to sneak by. *Science*, 311(5766):1385 – 1386, 2006.

[9] M.C. Roco and W.S. Bainbridge. *Converging Technologies for Improving Human Performance: Nanotechnology, Biotechnology, Information Technology and Cognitive Science*. Kluwer Academic Publishers, 2003.

[10] D.S. Goodsell. *Bionanotechnology: Lessons From Nature*. John Wiley & Sons, 2004.

[11] J.A. Venables. *Introduction to Surface and Thin Film Processes*. Cambridge University Press, 2000.

[12] S.H. Gyepi-Garbrah and R. Silerova. Probing temperature-dependent behavior in self-assembled monolayers by ac-impedance spectroscopy. *Phys. Chem. Chem. Phys.*, 3:2117–2123, 2001.

[13] R. Di Felice, A. Selloni, and E. Molinari. Dft study of cysteine adsorption on au(111). *J. Phys. Chem. B (USA)*, 107(5):1151 – 6, 2003/02/06.

[14] M. Mascini, M. Del Carlo, D. Compagnone, I. Cozzani, P. G. Tiscar, C. P. Mpamhanga, and B. Chen. Piezoelectric sensors based on biomimetic peptides for the detection of heat shock proteins (hsps) in mussels. *Analytical Letters*, 39(8):1627 – 1642, 2006.

[15] O. Cavalleri, G. Gonella, S. Terreni, M. Vignolo, L. Floreano, A. Morgante, M. Canepa, and R. Rolanid. High resolution x-ray photoelectron spectroscopy of l-cysteine self-assembled films. *Phys. Chem. Chem. Phys.*, 6:4042–4046, 2004.

[16] K. Uvdal, J. Ekeroth, P. Konradsson, and B. Liedberg. Tyrosine derivatives assembled on gold. *Journal of Colloid and Interface Science*, 260:361–366, 2003.

[17] S.M. Barlow and R. Raval. Complex organic molecules at metal surfaces: bonding, organisation and chirality. *Surf. Sci. Rep. (Netherlands)*, 50(6-8):201 – 341, 2003.

[18] D. Losic, J.G. Shapter, and J.J. Gooding. Atomically flat gold for biomolecule immobilization and imaging. *Aust. J. Chem.*, 54:643–648, 2001.

[19] O. Cavalleri, L. Oliveri, A. Dacca, R. Parodi, and R. Rolandi. Xps measurements on l-cysteine and 1-octadecanethiol self-assembled films: A comparative study. *Applied Surface Science*, 175-176:357 – 362, 2001.

[20] G. Dodero, L. De Michieli, O. Cavalleri, R. Rolandi, L. Oliveri, A. Dacca, and R. Parodi. L-cysteine chemisorption on gold: An xps and stm study. *Colloids and Surfaces A: Physicochemical and Engineering Aspects*, 175(1):121 – 128, 2000.

[21] T. Shin, K. Kim, C. Lee, S. Shin, and H. Kang. Self-assembled monolayer of l-cysteine on au(111): Hydrogen exchange between zwitterionic l-cysteine and physisorbed water. *J. Phys. Chem. B.*, 107:11674–11681, 2003.

[22] A. Kuhnle, T.R. Linderoth, B. Hammer, and F. Besenbacher. Chiral recognition in dimerization of adsorbed cysteine observed by scanning tunneling microscopy. *Nature*, 415(6874):891 – 893, 2002.

[23] Q.M Xu, L.J. Wan, C. Wang, C.L. Bai, Z.Y. Wang, and T. Nozawa. New structure of l-cysteine self-assembled monolayer on au(111): Studies by in situ scanning tunneling microscopy. *Langmuir*, 17(20):6203 – 6206, 2001.

[24] J.A. Rodriguez, J. Dvorak, T. Jirsak, G. Liu, J. Hrbek, Y. Aray, and C. Gonzalez. Coverage effects and the nature of the metal-sulfur bond in s/au(111): High-resolution photoemission and density-functional studies. *Journal of the American Chemical Society*, 125(1):276 – 285, 2003.

[25] A.S. Dakkouri, D.M. Kolb, R. Edelstein-Shima, and D. Mandler. Scanning tunneling microscopy study of l-cysteine on au(111). *Langmuir*, 12:2849–2852, 1996.

[26] M. M. Harding and H. A. Long. The crystal and molecular structure of l-cysteine. *Acta. Cryst.*, B24:1096–1102, 1968.

[27] W.H. Brown. *Introduction to Organic Chemistry*. Saunders College Pub., second edition, 2000.

[28] J. Sarfati. Origin of life: The chirality problem. *Creation Ex Nihilo Technical Journal*, 12(3):263–266, 1998.

[29] R. Di Felice and A. Selloni. Adsorption modes of cysteine on au(111): thiolate, amino-thiolate, disulfide. *J. Chem. Phys. (USA)*, 120(10):4906 – 14, 2004.

[30] C. Kittel. *Introduction to Solid State Physics*. John Wiley & Sons, seventh edition, 1996.

[31] G. Attard and C. Barnes. *Surfaces*. Oxford Science Publications, 1998.

[32] N. Takeuchi, C.T. Chan, and K.M. Ho. Au(111): A theoretical study of the surface reconstruction and the surface electronic structure. *Physical Review B*, 43:13899–13906, 1991.

[33] J.V. Barth, H. Brune, and G. Ertl. Scanning tunneling microscopy observations on the reconstructed au(111) surface: Atomic structure, long-range superstructure, rotational domains, and surface defects. *Physical Review B*, 42(15):9307–9318, 1990.

[34] M.P. Marder. *Condensed Matter Physics*. John Wiley & Sons, corrected printing edition, 2000.

[35] H. Bulou and C. Goyhenex. Local strain analysis of the herringbone reconstruction of au(111) through atomistic simulations. *Physical Review B*, 65:045407–1 – 045407–10, 2002.

[36] M. Prutton. *Introduction to Surface Physics*. Oxford Science Publications, 1994.

[37] J. Tersoff and D.R. Hamann. Theory of the scanning tunneling microscope. *Physical Review B*, 31(2):805–813, 1985.

[38] D.R. Lide. *CRC Handbook of Chemistry and Physics*. CRC Press, eighty sixth edition, 2005.

[39] G. Binning, H. Rohrer, Ch. Gerber, and E. Weibel. Surface studies by scanning tunneling microscopy. *Physical Review Letters*, 49(1):57–61, 1982.

[40] R.M. Tromp, E.J. van Loenen, J.E. Demuth, and N.D. Lang. Tip electronic structure in scanning tunneling microscopy. *Physical Review B*, 37(15):9042–9045, 1988.

[41] J. Bardeen. Tunneling from a many-particle point of view. *Physical Review Letters*, 6(2):57–59, 1961.

[42] J.J. Sakurai. *Modern Quantum Mechanics*. Addison Wesley, revised edition, 1994.

[43] F. Schwabl. *Quantum Mechanics*. Springer-Verlag, second revised edition, 2001.

[44] R. Weisendanger. *Scanning Probe Microscopy and Spectroscopy*. Cambridge University Press, 1994.

[45] C.J. Chen. *Introduction to Scanning Tunneling Microscopy*. Oxford University Press, 1993.

[46] R. Wiesendanger and H.J. Guntherodt. *Scanning Tunneling Microscopy III*. Springer, second edition, 1996.

[47] J. Tersoff and D.R. Hamann. Theory and application for the scanning tunneling mircoscope. *Physical Review Letters*, 50(25):1998–2001, 1983.

[48] A. Baratoff. Theory of scanning tunneling microscopy - methods and approximations. *Physica*, 127B:143–150, 1984.

[49] L.W. Swanson and L.C. Crouser. Anomalous total energy distribution for a tungsten field emitter. *Physical Review Letters*, 16:389–392, 1966.

[50] L.W. Swanson and L.C. Crouser. Total-energy distribution of field-emitted electrons and single-plane work functions for tungsten. *Physical Review*, 163:622–641, 1967.

[51] S. Ohnishi and M. Tsukada. Molecular orbital theory for scanning tunneling microscopy. *Solid State Comm.*, 71:391–394, 1989.

[52] G. Binnig and H. Rohrer. Scanning tunneling microscopy. *IBM J. Res. Develop.*, 44(1/2):279–293, 2000.

[53] M.D. Rempel. Commissioning of an ultra-high vacuum scanning tunneling microscope. Master's thesis, University of Saskatchewan, 2003.

[54] W. Steckelmacher. Knudsen flow 75 years on: the current state of the art for flow of rarefied gases in tubes and systems. *Rep. Prog. Phys. (UK)*, 49(10):1083 – 107, 1986.

[55] M. Knudsen. *The Kinetic Theory of Gases*. John Wiley & Sons, second edition, 1934.

[56] C. Kittel and H. Kromer. *Thermal Physics*. W. H. Freedman & Company, second edition, 1980.

[57] P.W. Atkins. *Physical Chemistry*. Oxford University Press, second edition, 1978.

[58] M. Knudsen. Cosine law in kinetic theory of gases. *Annalen der Physik*, 48:1113–1121, 1916.

[59] B.S. Halliday A. Chambers, R.K. Fitch. *Basic Vacuum Technology*. Taylor and Francis, second edition, 1998.

[60] H. Luth. *Surface and Interfaces of Solids*. Springer, second edition, 1993.

[61] G. Sauerbrey. The use of quartz oscillators for weighing thin layers and for microweighing. *Z. Phys.*, 155:206–222, 1959.

[62] B.D. Vogt, E.K. Lin, W. Wu, and C.C. White. Effect of film thickness on the validity of the sauerbrey equation for hydrated polyelectrolyte films. *J. Phys. Chem. B*, 108:12685–12690, 2004.

[63] C. Lu and A.W Czanderna. *Applications of Piezoelectric Quartz Crystal Microbalances*. Elsevier, 1984.

[64] A. Hirose. *Introduction to Wave Phenomena*. Krieger Publishing Company, reprinted edition, 1990.

[65] C.W. Hutchings and Michael Grunze. Apparatus for chemical vapour deposition of polyimide films. *Review of Scientific Instruments*, 66(7):3943 –, 1995.

[66] E.H. Copland and N.S. Jacobson. Thermodynamic activity measurements with knudsen cell mass spectrometry. *The Electrochemical Society Interface*, pages 28–31, 2001.

[67] L.A. Torres, I. Hernandez-Contreras, J.A. Guardado, and M.G. Gonzalez. Quartz crystal microbalance to determine enthalpies of sublimation at intermediate temperatures by the knudsen effusion method. *Measurement Science and Technology*, 5(1):51 – 53, 1994.

[68] J. R. Taylor. *An Introduction to Error Analysis: The Study of Uncertainties in Physical Measurements*. University Science Books, second edition, 1997.

[69] RHK Technology. *Variable Temperature Ultra-High Vacuum Scanning Tunneling Microscope User's Guide*. RHK Technology Inc, 1.2 edition, 2001.

[70] RHK Technology. *SPM 32 User's Guide*. RHK Technology Inc., 1.6 edition, 2002.

[71] RHK Technology. *PPC100, Pre-Amps and SPM 1000 User's Guides*. RHK Technology Inc, 1999.

[72] C.E.J. Mitchell, G. Florizone, L. Hinther, D. Muir, and B. Wilson. A sample manipulator head for an ultra-high vacuum preparation and analysis chamber. Fourth-Year Engineering Design Report at the University of Saskatchewan, March 2004.

[73] A.W. Robinson, M.P. Bradley, M. Barnett, K. Krochak, and J. Robb. Low energy ion source for ion implantation. Fourth-Year Engineering Design Report at the University of Saskatchewan, April 2005.

[74] Sigma Instruments Inc. *SQM-160 Rate/Thickness Monitor*. Sigma Instruments Inc., 2003.

[75] R. March and R. Hughes. *Quadrupole Storage Mass Spectrometry*. John Wiley & Sons, 1989.

[76] Hiden Analytical. *RC Systems Manual*. Hiden Analytical Ltd., issue: b rev.: 1 edition, October 2003.

[77] Hiden Analytical. *MASoft Version 4 User's Manual*. Hiden Analytical Ltd., issue b edition, December 2002.

[78] N.G. Semaltianos and E.G. Wilson. Investigation of the surface morphology of thermally evaporated thin gold films on mica, glass, silicon and calcium fluoride substrates by scanning tunneling microscopy. *Thin Solid Films*, 366(1-2):111 – 116, 2000.

[79] C. Li, 2003. Personal communication with Dr. Chenzhong Li (Dept. of Biochemistry) at University of Saskatchewan.

[80] N. Olfert. Tip etching. Nanoscale & Surface Physics Laboratory Procedure Booklet, August 2003.

[81] V.M. Hallmark, S. Chiang, J.F. Rabolt, J.D. Swalen, and R.J. Wilson. Observation of atomic corrugation on au(111) by scanning tunneling microscopy. *Phys. Rev. Lett. (USA)*, 59(25):2879 – 82, 1987/12/21.

[82] R.L. McCarley and J.A. Bard. Surface reactions of au(111) with aqueous cyanide studied by scanning tunneling microscopy. *Journal of Physical Chemistry*, 96(18):7410 –, 1992.

[83] R. Sabbah and C.C Minadakis. Thermodynamics of sulfur compounds ii. thermochemical study of. *Thermochimica Acta*, 43(3), 1981.

[84] Origin. *Origin Pro Manual*. Origin Scientific Graphing and Data Analysis Software, 7 edition, 2002.

[85] Origin. *Getting Started Manual*. Origin Scientific Graphing and Analysis Software, 7 edition, 2002.

[86] Origin. *Peak Fitting Module Manual*. Origin Scientific Graphing and Analysis Software, 7 edition, 2002.

[87] Origin. *Programming Guide*. Origin Scientific Graphing and Analysis Software, 7 edition, 2002.

[88] K. Biemann and James A. McCloskey. Mass spectra of organic molecules. ii amino acids. *J. Am. Chem. Soc.*, 84(16):3192–3193, 1962.

[89] S.E. Stein. *NIST Standard Reference Database*, chapter 69. National Institute of Standards and Technology, http://webbook.nist.gov, June 2005.

[90] G. Junk and H. Svec. The mass spectra of alpha-amino acids. *J. Am. Chem. Soc.*, 85(7):839–845, 1963.

[91] K. Prince, 2006. Personal communication of Dr. Katie Mitchell with Dr. Kevin Prince (Sincrotrone Trieste).

[92] K. Biemann, J. Siebl, and F. Gapp. Mass spectra of organic molecules. i ethyl esters of amino acids. *J. Am. Chem. Soc.*, 83:3795–3804, 1961.

[93] G. W. A. Milne, T. Axenrod, and H. M. Fales. Chemical ionization mass spectrometry of complex molecules. iv. amino acids. *J. Am. Chem. Soc.*, 92(17):5170–5175, 1970.

[94] G.J. Leggett, M.C. Davies, D.E. Jackson, and S.J.B. Tendler. Surface studies by static secondary ion mass spectrometry: adsorption of 3-mercaptopropionic acid and cysteine onto gold surfaces. *J. Phys. Chem. (USA)*, 97(20):5348 – 55, 1993/05/20.

[95] B. Khawas. X-ray study of l-arginine hci, l-cysteine, dl-lysine and dl-phenylalanine. *Acta. Cryst.*, B(27):1517–1520, 1971.

[96] B. Khawas. Unit cells and space groups of l-methionine, l-beta-phenylalanine, and dl-tyrosine. *Acta. Cryst.*, B(26):1919–1924, 1970.

[97] J.S. Gaffney, R.C. Pierce, and L. Friedman. Mass spectrometer study of evaporation of alpha-amino acids. *J. Am. Chem. Soc.*, 99(13):4293–4298, June 1977.

[98] H.J. Svec and D.D. Clyde. Vapour pressures of some alpha-amino acids. *Journal of Chemical Engineering Data*, 10(2):151–152, April 1965.

[99] W.F. Riley, L.D. Sturges, and D.H. Morris. *Mechanics of Materials*. John Wiley & Sons, fifth edition, 1999.

Appendix A
Blueprints of Knudsen Cell Components

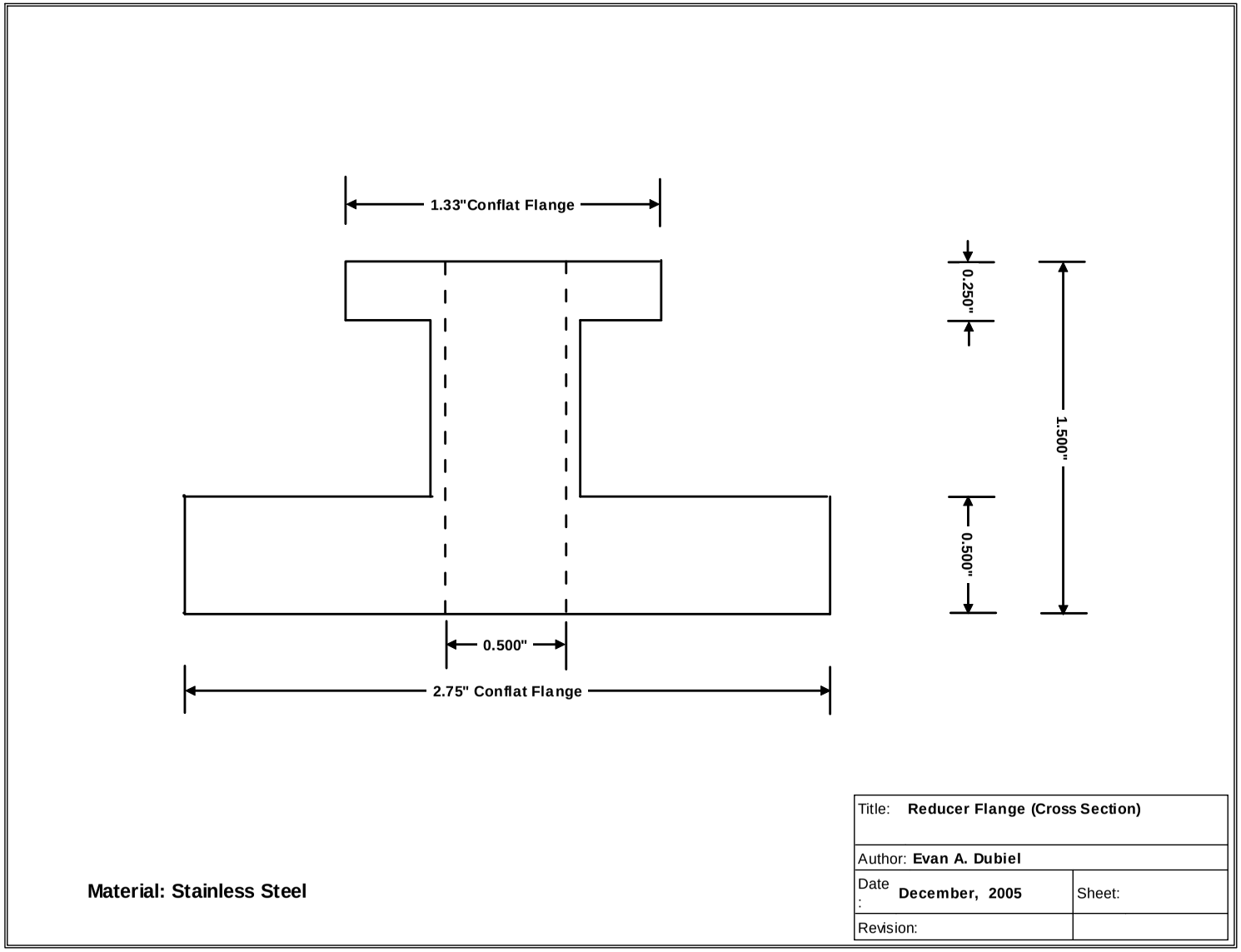

Figure A.1: Custom designed reducer flange schematic

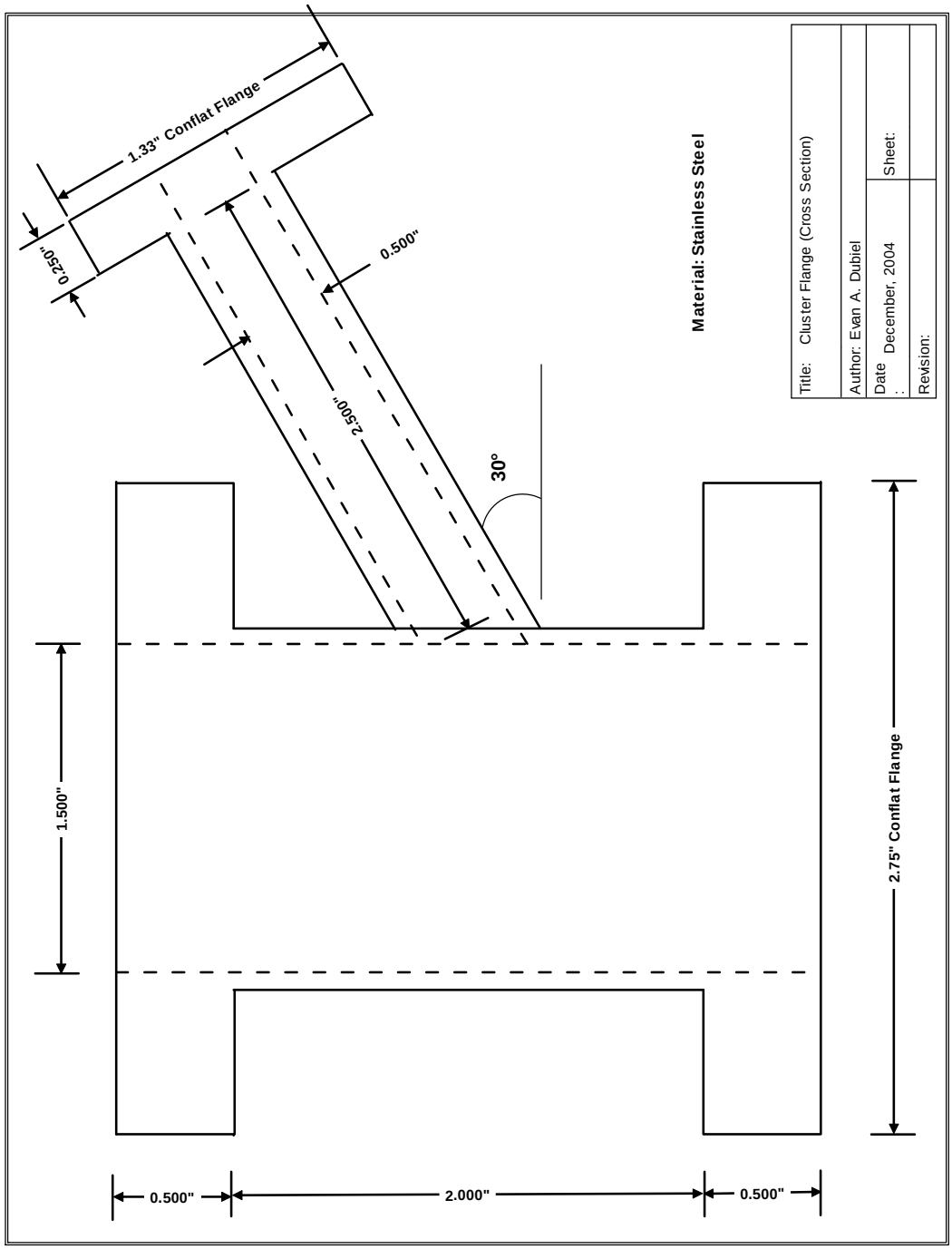

Figure A.2: Custom designed cluster flange schematic

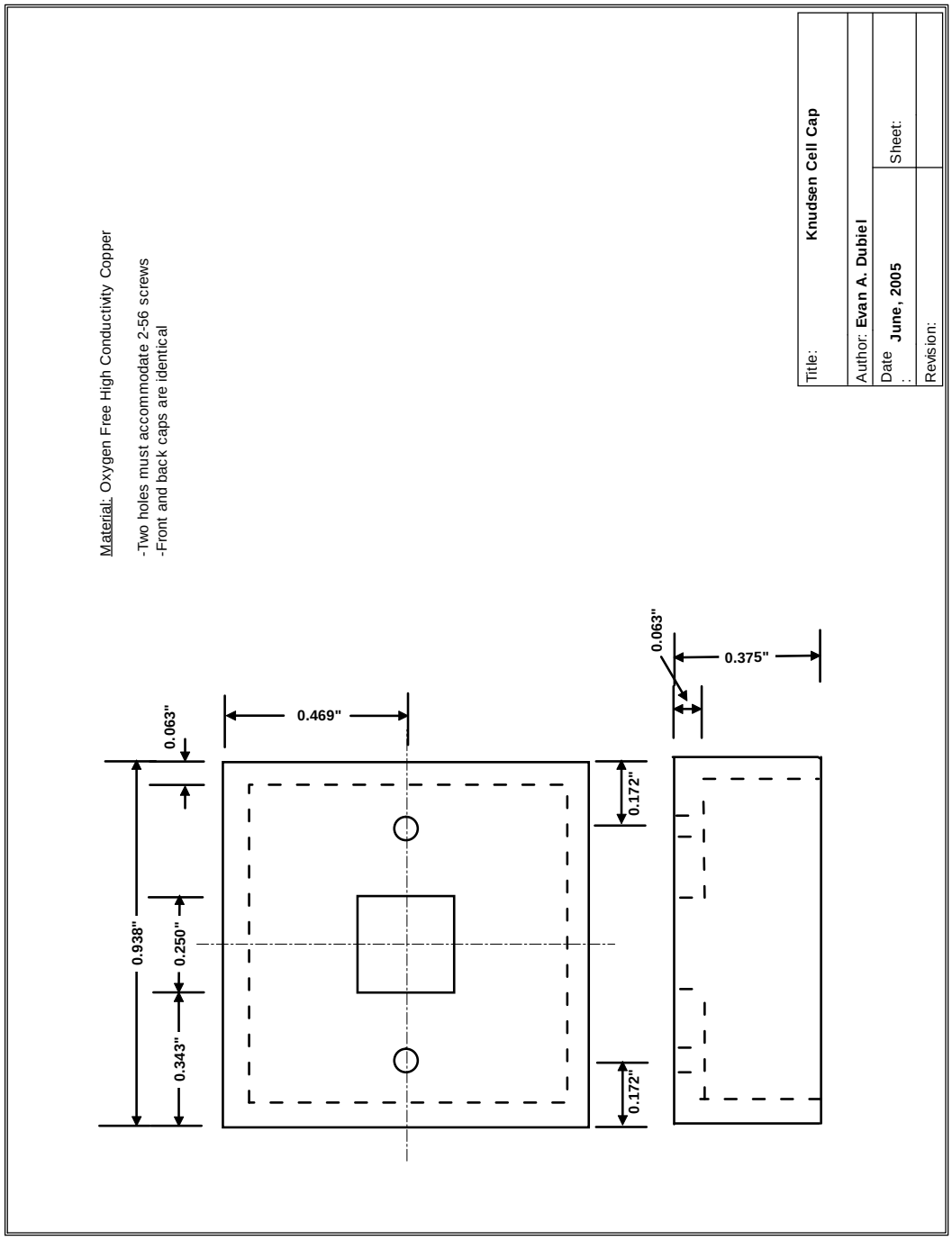

Figure A.3: Knudsen oven cap schematic

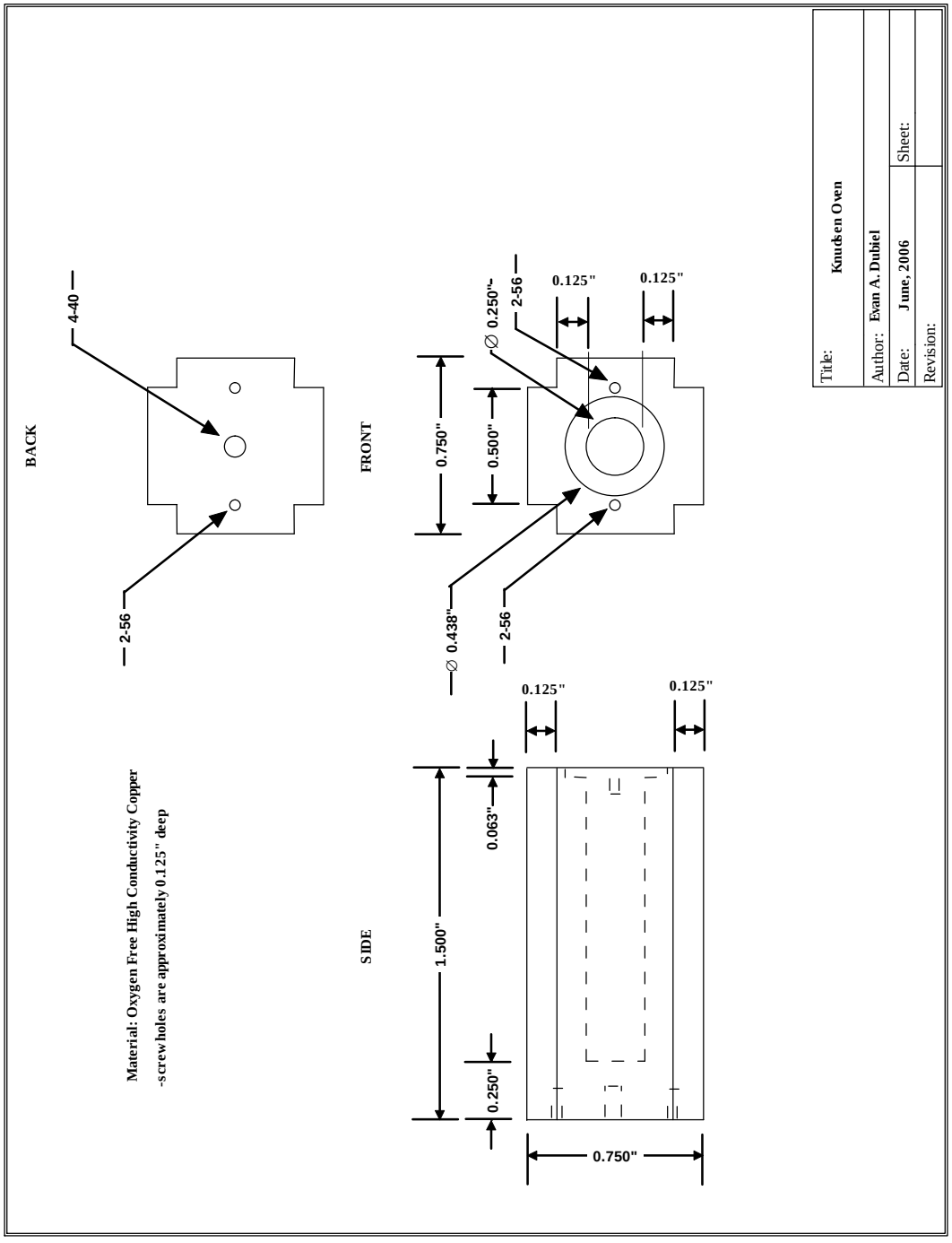

Figure A.4: Knudsen oven body schematic

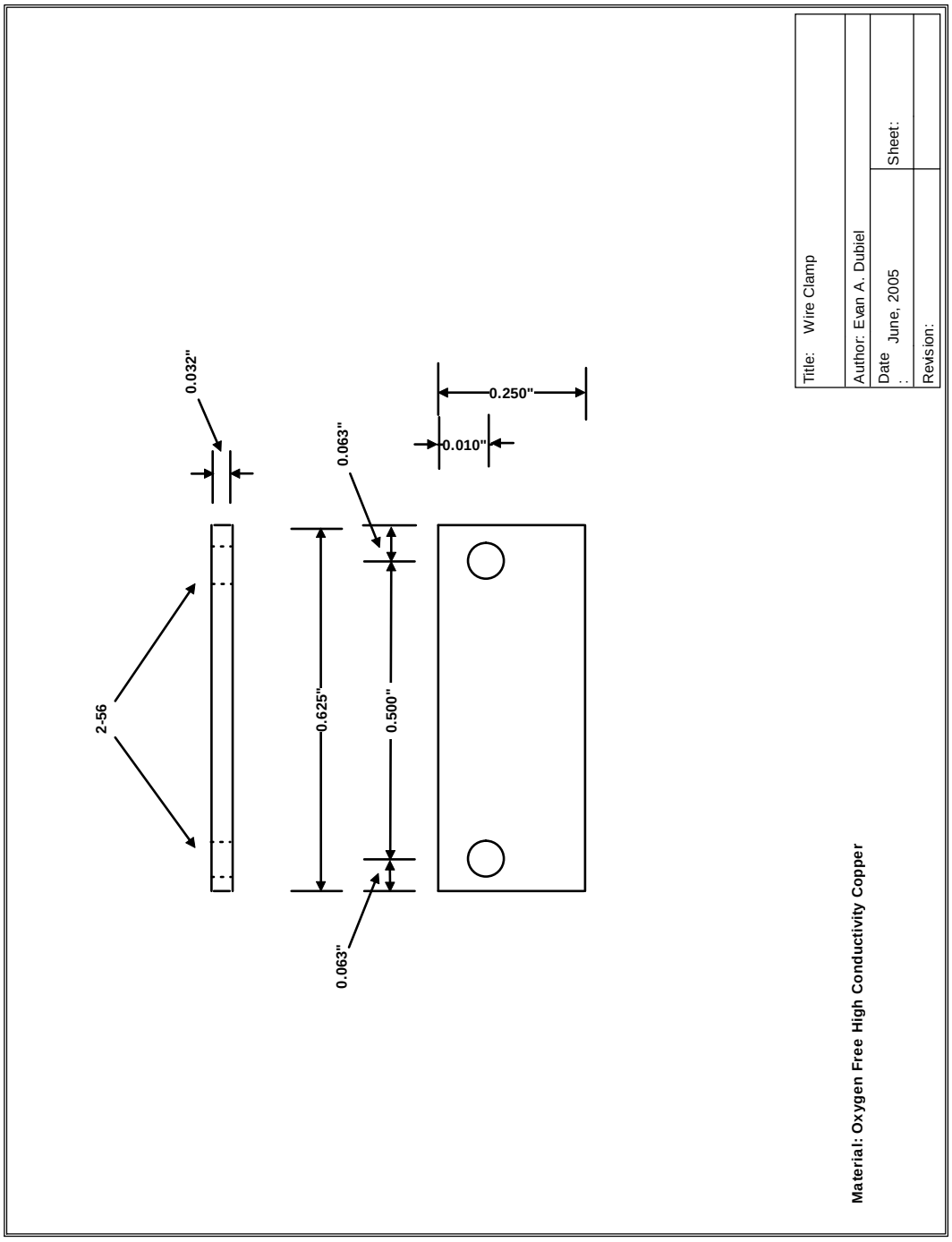

Figure A.5: Schematic for wire guide plate on Knudsen cell

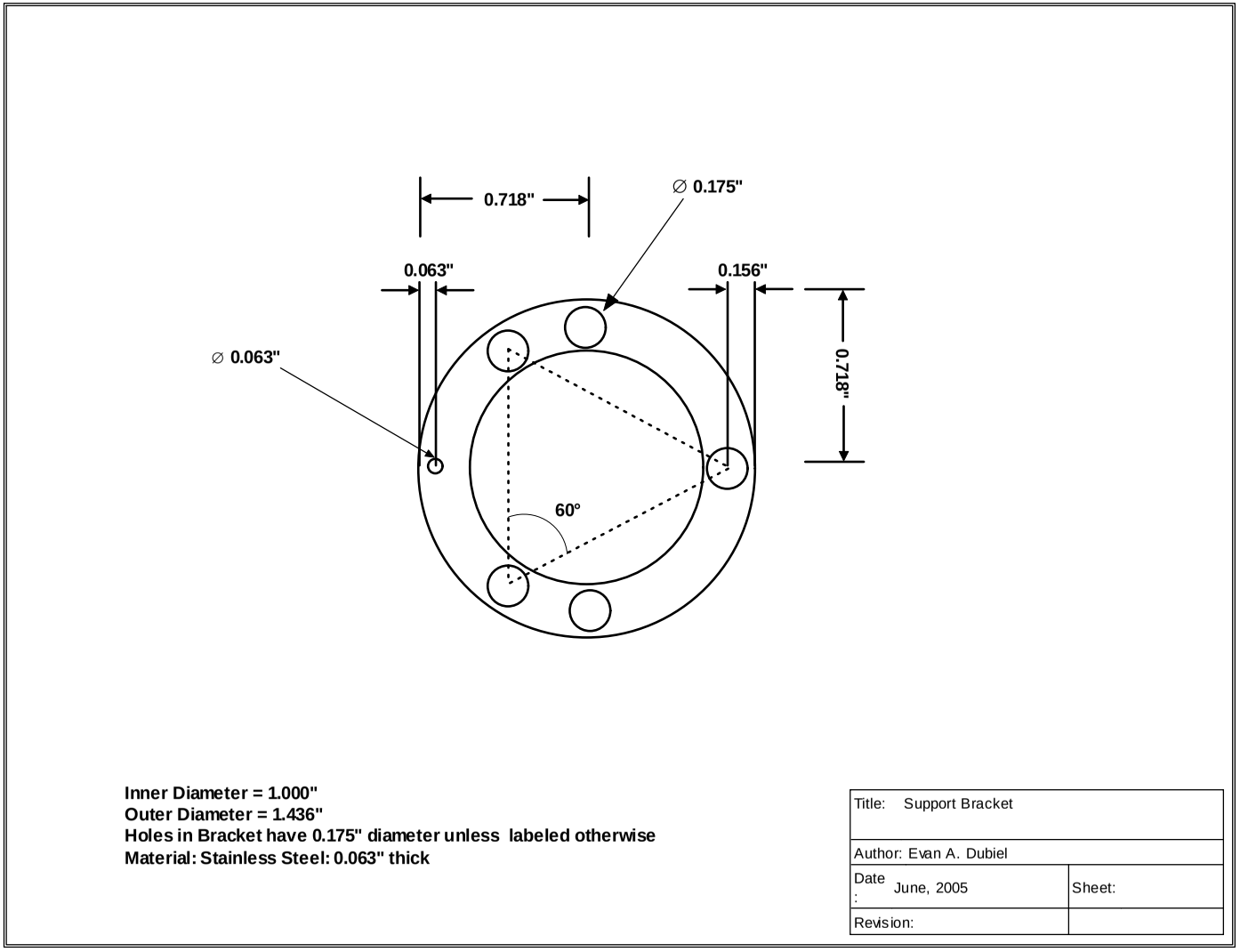

Figure A.6: Schematic for support collar on Knudsen cell

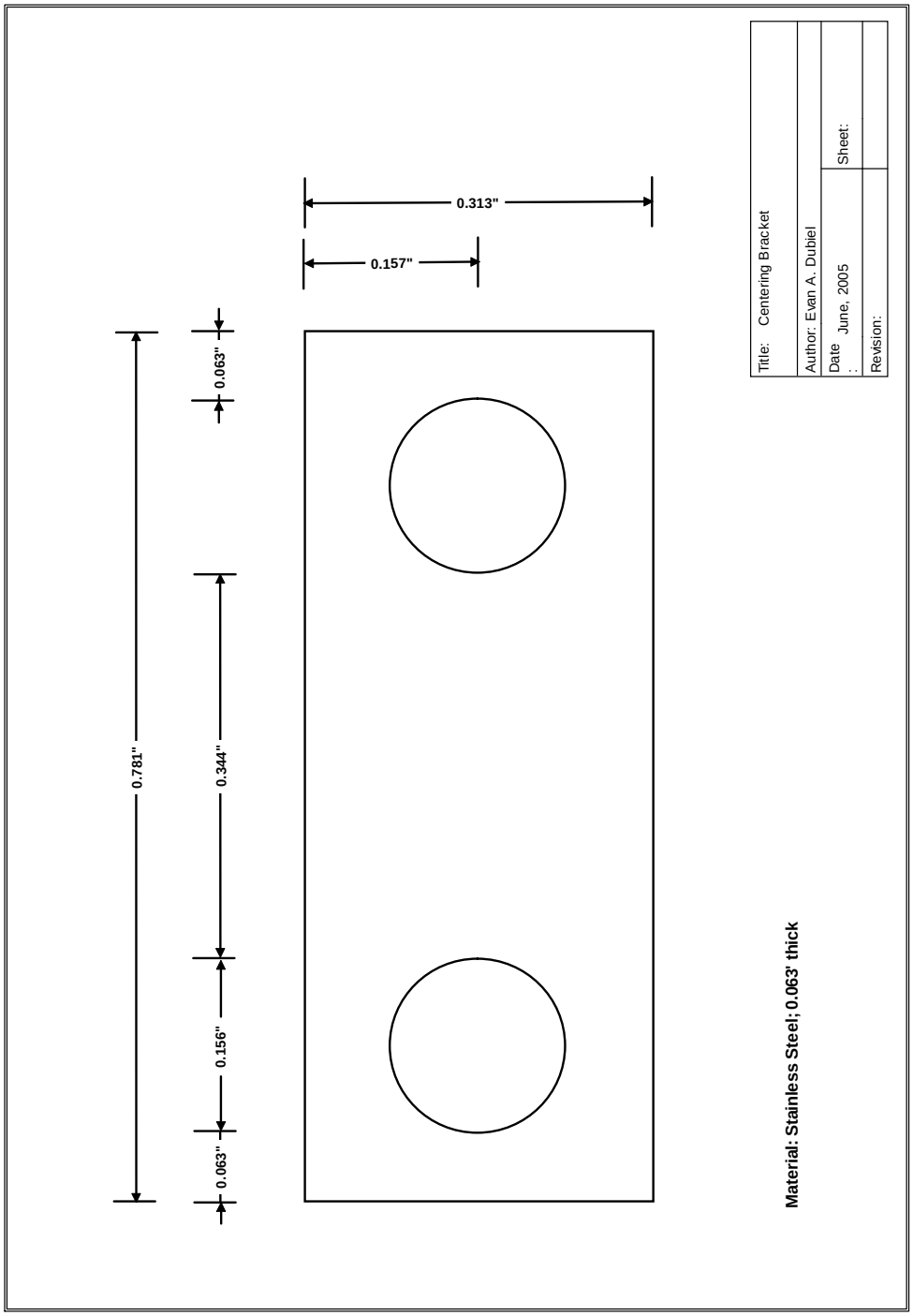

Figure A.7: Schematic for centering bracket on Knudsen cell

Appendix B
Commercial Parts for Knudsen Cell

Table B.1: Commercial parts for Knudsen cell

Component	**Manufacturer**	**Reference**
Linear Feedthrough	MDC Vacuum Products	LTM-154
Rotary Feedthrough	MDC Vacuum Products	HTBRM-133
Electrical Feedthrough	Datacomp Electronics	T31K1231502
Ceramics	Datacomp Electronics	EFS110-20-1000
BeCu Barrel Connectors	Kurt J. Lesker	FTAIBC058
Thermocouple Wire	Kurt J. Lesker	FTAWKU32
Power Line Wire	Kurt J. Lesker	FTAWCU32
Heater Wire	Mor Electric Heating Assoc., Inc	19GA-NI60

Appendix C
Support Rod Deflection of Knudsen Cell

The Knudsen cell (K-cell) should be aligned with its centerline in the horizontal plane. A small deviation (on the order of 1 mm or less) is acceptable. The maximum deviation of the K-cell aperture from the horizontal center line was estimated by assuming the weight of the K-cell was divided evenly between the three support rods. The equation (see Figure C.1) for the deflection of a support rod is

$$y_{\max} = \frac{FL^3}{3EI} \tag{C.1}$$

where F is the force on the beam, L is the length of the beam, E is the elastic modulus of the material the support rod is made of (in this case stainless steel), and I is the moment of inertia of the beam [99]. The moment of inertia of a cylindrical support rod is

$$I = \pi \frac{r^4}{4} \tag{C.2}$$

where r is the radius of the cylindrical support rod [99].

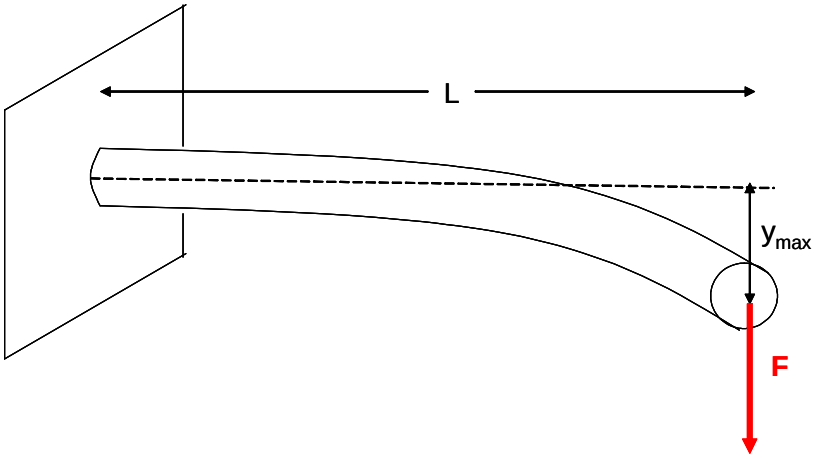

Figure C.1: Deflection of cylindrical support rod

The mass of the Knudsen oven is 200 g. The support rod has a length $L = 0.293\,\mathrm{m}$ and a radius $r = 0.00238\,\mathrm{m}$. Using equation C.1 and

$$\begin{aligned} F &= mg \\ &= \left(\frac{0.200\,\mathrm{kg}}{3}\right)(9.81\,\mathrm{m/\,s^2}) \\ &= 0.65\,\mathrm{N} \end{aligned} \tag{C.3}$$

with equation C.2

$$\begin{aligned} I &= \frac{\pi(0.00238\,\mathrm{m})^4}{4} \\ &= 2.52\ \mathrm{x}\ 10^{-11}\,\mathrm{m}^4 \end{aligned} \tag{C.4}$$

the deflection of the support rod is

$$\begin{aligned} y_{\max} &= \frac{(0.65\,\mathrm{N})(0.293\,\mathrm{m})^3}{3(190G\,\mathrm{Pa})(2.52\ \mathrm{x}\ 10^{-11}\,\mathrm{m}^4)} \\ &= 1.1\,\mathrm{mm} \end{aligned} \tag{C.5}$$

The value of the elastic modulus E for stainless steel was taken from Riley *et. al.*[99]. The alignment was also checked by eye and the deflection was not noticeable.

Appendix D
Amino Acid Decomposition Temperatures

All decomposition temperatures are taken from the CRC Handbook of Chemistry and Physics [38] unless referenced otherwise.

Table D.1: Decomposition temperatures of amino acids.

Name	**Chemical Formula**	**Decomp. Temp. (K)**
Alanine	CH_3-CH(NH_2)-COOH	587
Arginine	HN=C(NH_2)-NH-(CH_2)$_3$-CH(NH_2)-COOH	517
Asparagine	H_2N-CO-CH_2-CH(NH_2)-COOH	509
Cysteine	HS-CH_2-CH(NH_2)-COOH	513,[38] 448 [83]
Glutamine	H_2N-CO-(CH_2)$_2$-CH(NH_2)-COOH	458
Glycine	NH_2-CH_2-COOH	535
Histidine	NH-CH=N-CH=C-CH_2-CH(NH_2)-COOH	557
Isoleucine	CH_3-CH_2-CH(CH_3)-CH(NH_2)-COOH	558
Leucine	(CH_3)$_2$-CH-CH_2-CH(NH_2)-COOH	568
Lysine	H_2N-(CH_2)$_4$-CH(NH_2)-COOH	498
Methionine	CH_3-S-(CH_2)$_2$-CH(NH_2)-COOH	556
Phenylalanine	Ph-CH_2-CH(NH_2)-COOH	556
Proline	NH-(CH_2)$_3$-CH-COOH	493
Serine	HO-CH_2-CH(NH_2)-COOH	501
Threonine	CH_3-CH(OH)-CH(NH_2)-COOH	508
Tryptophan	Ph-NH-CH=C-CH_2-CH(NH_2)-COOH	563
Tyrosine	HO-Ph-CH_2-CH(NH_2)-COOH	615
Valine	(CH_3)$_2$-CH-CH(NH_2)-COOH	588